HYBRID EXCITED SYNCHRONOUS GENERATOR DESIGN AND COMPARISON OF DIRECT DRIVE WIND TURBINES

A THESIS SUBMITTED TO
THE GRADUATE SCHOOL OF NATURAL AND APPLIED SCIENCES
OF
MIDDLE EAST TECHNICAL UNIVERSITY

BY

AYSEL AKGEMCİ

IN PARTIAL FULFILLMENT OF THE REQUIREMENTS
FOR
THE DEGREE OF MASTER OF SCIENCE
IN
ELECTRICAL AND ELECTRONICS ENGINEERING

JANUARY 2019

Approval of the thesis:

HYBRID EXCITED SYNCHRONOUS GENERATOR DESIGN AND COMPARISON OF DIRECT DRIVE WIND TURBINES

submitted by **AYSEL AKGEMCİ** in partial fulfillment of the requirements for the degree of **Master of Science in Electrical and Electronics Engineering Department, Middle East Technical University** by,

Prof. Dr. Halil Kalıpçılar
Dean, Graduate School of **Natural and Applied Sciences**

Prof. Dr. Tolga Çiloğlu
Head of Department, **Electrical and Electronics Engineering**

Assist. Prof. Dr. Ozan Keysan
Supervisor, **Electrical and Electronics Engineering, METU**

Examining Committee Members:

Assoc. Prof. Dr. Murat Göl
Electrical and Electronics Engineering, METU

Assist. Prof. Dr. Ozan Keysan
Electrical and Electronics Engineering, METU

Assist. Prof. Dr. Emine Bostancı
Electrical and Electronics Engineering, METU

Prof. Dr. Oğuz Uzol
Aerospace Engineering, METU

Assist. Prof. Dr. Tolga İnan
Electrical and Electronics Engineering, Çankaya University

Date: 18.01.2019

I hereby declare that all information in this document has been obtained and presented in accordance with academic rules and ethical conduct. I also declare that, as required by these rules and conduct, I have fully cited and referenced all material and results that are not original to this work.

Name, Last Name: Aysel Akgemci

Signature :

ABSTRACT

HYBRID EXCITED SYNCHRONOUS GENERATOR DESIGN AND COMPARISON OF DIRECT DRIVE WIND TURBINES

Akgemci, Aysel
M.S., Department of Electrical and Electronics Engineering
Supervisor : Assist. Prof. Dr. Ozan Keysan

January 2019, 108 pages

Various types of electrical generators are used in wind turbines and there is not an agreement on the best generator type. Although, high speed Doubly Fed Induction Generators (DFIGs) are still the most common generator topology utilized in wind turbine systems, there is a trends toward direct-drive Permanent Magnet Synchronous Generators (PMSGs), as they are more efficient and reliable. However, permanent magnets (PMs) induce uncontrollable voltage due to the fixed flux resulting from PM excitation. Conventional synchronous direct-drive generators are controllable, but they usually have a higher mass.

In the last decade, the idea of using hybrid excitation to effectively control the output voltage emerged. The hybrid term come from the employment of both PM and DC-excited field winding excitations. By this way, it would be possible to control the load angle and power factor, and an uncontrolled diode rectifier can be used. Furthermore, the amount of required magnet reduces, which helps to reduce overall cost.

In this thesis, several topologies of the hybrid excited generators in the literature will be introduced and a 2.5 MW two rotor hybrid excited generator is designed for direct drive wind turbine application. The design is evaluated using finite element method (FEM) simulations. At the same ratings, the generator topology is compared with the PMSG and Electrically Excited Synchronous Generator (EESG) in terms of short circuit characteristics, torque ripple and induced voltage harmonics.

Keywords: Hybrid Excited Synchronous Generator, wind turbine generator design, FEA of electrical machines

ÖZ

HİBRİT UYARTIMLI SENKRON GENERATÖR TASARIMI VE DOĞRUDAN SÜRÜŞLÜ RÜZGÂR TÜRBİNLERİNİN KARŞILAŞTIRILMASI

Akgemci, Aysel
Yüksek Lisans, Elektrik ve Elektronik Mühendisliği Bölümü
Tez Yöneticisi : Dr. Öğr. Üyesi Ozan Keysan

Ocak 2019 , 108 sayfa

Rüzgâr türbini sistemlerinde çeşitli generatörler kullanılmaktadır ve halen en iyi generatör tipinin hangisi olduğuna dair bir uzlaşıya varılmamıştır. Rüzgâr türbinlerinde en sık rastlanan generatör topolojisi yüksek hızlı Çift Beslemeli İndüksiyon Generatörleri olsa da, daha verimli ve güvenilir olan doğrudan sürüşlü Sabit Mıknatıslı Senkron Generatörler yükselişe geçmiştir. Fakat Sabit Mıknatıslar oluşturdukları sabit akı sebebiyle kontrol edilemeyen bir gerilim indüklerler. Ayrıca alışılagelmiş doğrudan sürüşlü senkron generatörler kontrol edilebilirdirler ama genellikle daha ağırdırlar.

Son yıllarda çıkış gerilimini etkili bir biçimde kontrol etmek için hibrit uyartım kullanma fikri öne sürülmüştür. Hibrit terimi generatör uyartımında sabit mıknatıslarla beraber DC uyartımlı alan sargılarının kullanılmasından gelmektedir. Bu sayede yük açısını ve güç faktörünü kontrol etmek mümkün olabilecektir ve bu durumda güç dönüştürücüde diyot doğrultucu kullanılabilecektir. Ayrıca aynı güçte gereken mıknatıs mıktarı azalacağı için generatör maliyeti de düşecektir.

Sunulan tezde hibrit uyartımlı generatörlerin literatürde bahsi geçen çeşitleri ve 2,5 MW gücünde iki rotorlu bir hibrit generatör topolojisinin doğrudan sürüşlü rüzgâr türbinleri uygulamaları için tasarımı aktarılmıştır. Tasarım sonlu eleman analizleri kullanılarak değerlendirilmiştir. Tasarlanan generatör aynı güç değerlerindeki Sabit Mıknatıslı ve Elektrikle Uyarılmış Senkron Generatörlerle kısa devre karakteristikleri, tork dalgalanmaları ve indüklenen gerilimdeki harmonikler açısından karşılaştırılmıştır.

Anahtar Kelimeler: Hibrit Uyartımlı Senkron Generatör, Rüzgâr türbini generatörü tasarımı, elektrik makinelerinin sonlu elemanlar analizi

To Esra and Mahmut

ACKNOWLEDGMENTS

Firstly, I would like to express my deep gratitude to Assist. Prof. Dr. Ozan Keysan, not only for his encouragement and guidance throughout his supervision but also for being an unprejudiced, kind and thoughtful human being.

I also would like to thank Reza Zeinali for teaching me all about the machine design and simulation. I am lucky to have studied with such a hardworking, polite and helpful person. I also want to thank Assist. Prof. Dr. Emine Bostancı for sharing her knowledge and spending time on me always with a smiling face.

I am grateful to Erencan Duymaz and Doğa Ceylan for their valuable support and for making the working environment so enjoyable. I also thank Siamak Pourkeivannour, İlker Şahin, Salar Koushan and the rest of the Powerlab members as I am proud of being in a research group with them. I also thank Özgür Yazıcı for his great support during my simulation and analysis process. I am sure that he will be one of the best electrical machine designer in Turkey.

I feel unspeakably grateful to have surrounded by friends who made such a stressful term of my life bearable: Ece Büber, Negin Razizadeh, Sevil Çalışkan, Çağan Yüksel, Furkan Doğramacı, Erdem Canbalaban, Berkay Baykara, Baybora Matur, Doğancan Eser and the rest of the "Yemekhane Team". I also would like to mention my oldest friends Fethiye Mermer, Zehra Koştu and Melek Demiröz who were and always will be there for me. I also should thank Caner Sağlam for his valuable support.

I must also express my gratitude to my parents, Emine Güler and Tahir for their endless support. I am thankful to have parents who believe in me and cherish me.

Lastly, I want to thank my dearest siblings Esra and Mahmut for showing me that the endless struggle of life is worth fighting on, knowing that it is meaningless yet beautiful. Without them, I would never have grasped that there is honor in being yourself.

TABLE OF CONTENTS

CHAPTERS

LIST OF TABLES

TABLES

LIST OF FIGURES

FIGURES

LIST OF ABBREVIATIONS

EESG	Electrically Excited Synchronous Generator
DFIG	Doubly Fed Induction Generator
DSPM	Doubly Salient Permanent Magnet
FEA	Finite Element Analysis
FEM	Finite Element Method
GA	Genetic Algorithm
HESG	Hybrid Excited Synchronous Generator
HVDC	High Voltage Direct Current
LCOE	Levelized Cost of Energy
PM	Permanent Magnet
PMSG	Permanent Magnet Synchronous Generator
RFPM	Radial Flux Permanent Magnet
SCIG	Squirrel Cage Induction Generator
THD	Total Harmonic Distortion
VCS	Voltage Source Converter
WF	Wound Field

LIST OF SYMBOLS

D	Stator Bore Diameter
D_i	Inner Diameter
D_o	Outer Diameter
g	Air-gap Length
h_t	Stator Tooth Height
h_{tr}	Rotor Tooth Height
I_f	Field Current
J	Current Density of the Armature Windings
J_r	Current Density of the Field Windings
l_m	Magnet Thickness
L_{stk}	Stacking Length
P	Number of Poles
R_{ph}	Phase Resistance of Armature Windings
R_f	Resistance of the Field Windings
s_o	Stator Tooth Tip Ratio
s_{or}	Rotor Tooth Tip Ratio
t_w	Tooth Width
X_{sd}	d-axis Component of the Phase Reactance
X_{sq}	q-axis Component of the Phase Reactance
q	Electrical Loading

CHAPTER 1

INTRODUCTION

Wind energy has a long history from windmills to today's modern wind turbines although it had not been given much importance until 1970s. Thanks to the technological developments and increasing investments in 80s, wind energy has become a competitive energy source in the 21st century. It is recorded that the weighted average investment cost for onshore wind fell by slightly more than two-thirds between 1983 and 2015 where the Levelized Cost of Energy (LCOE) fell from USD 0.38/kWh to USD 0.06/kWh over the same period [1].

Wind energy market has continuously being shaped by technological developments and economical feasibility of these technologies. Although a typical wind turbine contains up to 8000 different components and the most expensive parts are the ones that are not directly involved in electricity generation, technology level of a wind turbine concept is mostly related to components in the drive train, namely the generator, the gearbox and the power converter.

In Figure 1.1, the percentage costs of the main components of a 2 MW REpower MM92 model wind turbine utilizing 3 staged gearbox and Doubly Fed Induction Generator (DFIG) are given. As seen from the chart, the gearbox covers 13% of the overall cost whereas the generator covers only 3% [2]. However, for the direct drive wind turbines in which the gearbox is eliminated and the generator mass is increased dramatically, the generator cost also covers that 13% and reaches up to 16% share. Therefore, it can be concluded that from economical and technological point of view, drive train technologies play crucial role in the wind turbine industry.

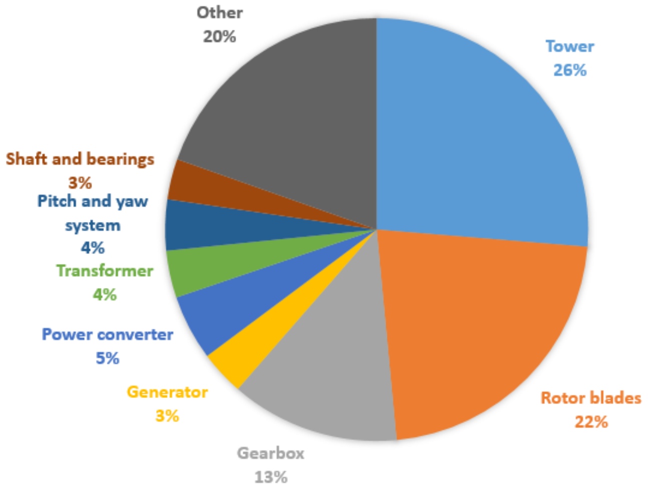

Figure 1.1: The contribution of the turbine components to the overall cost [2].

1.1 Wind Turbine Generator Topologies Used in Industry

The drive train configurations used in industry are shaped according to the features and the capabilities of the utilized generator. For instance, the generator types operating at constant speed and the corresponding turbine topologies diminish as the generators operating at variable speed yield more durable drive train and higher aerodynamic efficiency.

Two main types of wind turbine generator and their basic variations can be listed as follows:

- AC Asynchronous (Induction) Generators
  - Squirrel Cage Induction Generator (SCIG)
  - Wound Rotor Induction Generator (WRIG)
  - Doubly-Fed Induction Generator (DFIG)
- AC Synchronous Generators
  - Electrically Excited Synchronous Generator (EESG)
  - Permanent Magnet Synchronous Generator (PMSG)

The general properties of these generators and the drive train configurations associated with them are investigated in the following parts of this section.

1.1.1 Induction Generators

Induction generators are cheap, simple and well-developed as they are based on a mature technology. There are various applications of induction generators in wind turbines; however, the need for reactive power compensation is a common drawback of the topologies utilizing induction generators. In addition, they are generally used with three staged gearboxes because low rotational speeds in direct drive concept would require larger dimensions, hence larger air gap lengths. The magnetizing currents goes up and losses increase dramatically as air gap gets larger [3]. Therefore, having a speed around 1000-2000 rpm, induction generators used in wind energy are relatively small but the associated topologies are gearbox dependent.

Constant speed wind turbines utilize SCIGs as seen in Figure 1.2. In this topology, power factor compensation is provided by the capacitor bank and the soft starter enables smoother grid connection. This primitive topology with no speed control and poor transient behavior gradually disappears from the market. Nonetheless, SCIGs can be used in variable speed concept with full power converter as seen in Figure 1.3. This topology, mostly adopted by SIEMENS brand wind turbines, brings the advantages of SCIGs and variable speed concept together.

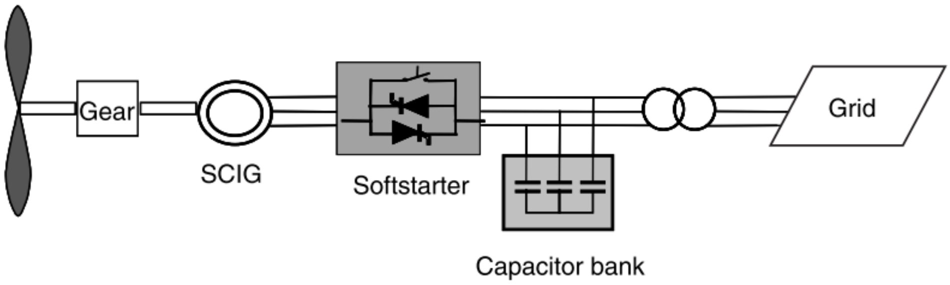

Figure 1.2: SCIG in constant speed wind turbines [4].

The same drive train configuration in constant speed concept allows variable speed in a limited range when WRIG is used instead of SCIG. The speed control is realized through a variable resistance connected series with rotor windings (Figure 1.4). The

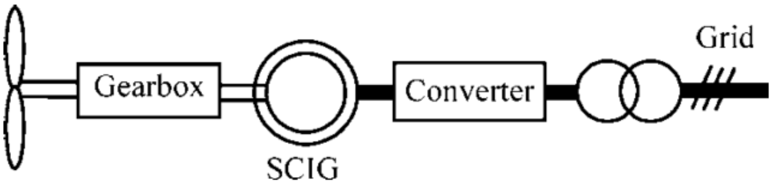

Figure 1.3: SCIG in full power converter speed controlled wind turbines [5].

speed range determined by the ratings of the variable resistance is typically 10% of the synchronous speed. A wider control range would increase the slip and hence decrease the efficiency. This topology is also no longer preferred as DFIGs dominate the market thanks to low price of the utilized topology and wider speed control range.

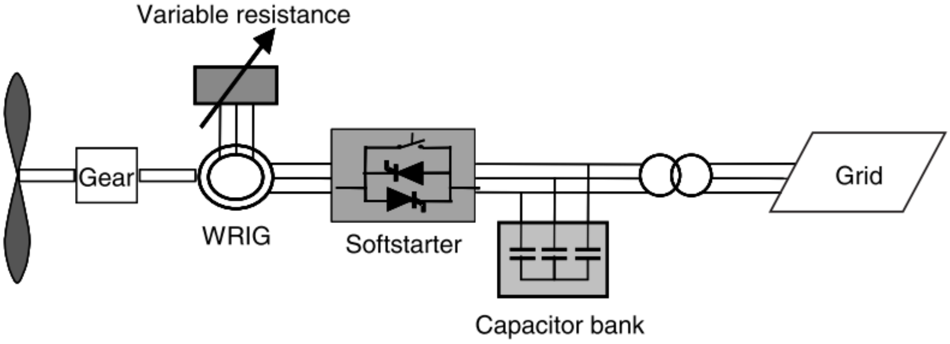

Figure 1.4: WRIG in variable speed concept with limited range [4].

In DFIG topology, as seen in Figure 1.5, the wound rotor is connected to the grid via a partial scale power converter rated around 30% of the total power. The scale of the converter determines the speed control range and the cost of the power converter. Adopting partial scale converter instead of full scale ones lowers the size and hence the cost of power electronic components but limits the power and speed control capabilities. DFIGs are still the most common generator topology in wind turbines due to the know-how level and mature production capabilities of the leading companies in the sector. Moreover, utilization of partial scale converter results in decreased drive train cost which makes DFIG topology attractive.

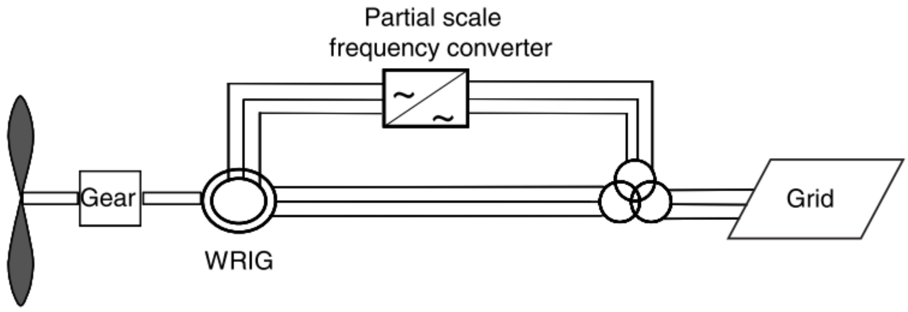

Figure 1.5: Utilization of DFIG in wind turbines [4].

1.1.2 Synchronous Generators

Synchronous generators, contrary to induction generators, are suitable for the direct drive applications where rotational speed is low and torque rating is high. Although full scale power converter requirement can be accepted as a downside of the topologies utilizing synchronous generators, energy yield and efficiency are expected to be higher in these topologies. The utilization of synchronous generators in wind turbines may generally be associated with the idea of discarding the gearboxes and their drawbacks in terms of efficiency and maintenance. However, synchronous generators connected to single or two staged gearboxes and operating at medium speed are not common yet.

1.1.2.1 Electrically Excited Synchronous Generators

The rotor of the typical synchronous generators carries field windings excited with DC and has either cylindrical or salient poles. Since salient pole machines are more advantageous in low speed applications, they are preferred in wind turbines utilizing EESG. The general configuration of direct drive EESG concept is given in Figure 1.6.

The excitation current can be controlled by the converter on the rotor side and it is possible to control the amplitude and frequency of generator output voltage and active/reactive power generation. Flux control capability and permanent magnet free structure are among the advantages of EESG; however, DC excitation on the rotor

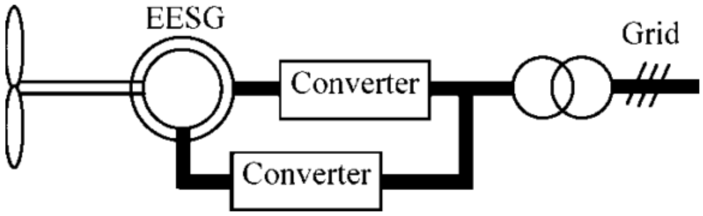

Figure 1.6: Direct drive EESG topology [5].

requires brushes or rotating rectifier where field losses are inevitable in both cases.

Direct drive EESG concept maintains market position thanks to ENERCON [6], the biggest representative of the topology in wind industry. However, EESGs are not common in Asia and North America where PMSG utilization seems to be the first choice in direct drive applications [7].

1.1.2.2 Permanent Magnet Synchronous Generators

Field excitation in PMSGs is created by permanent Magnets (PMs) and they are more efficient than EESGs as field windings and their associated losses are eliminated. In addition to having high efficiency, energy yield and torque density; PMSGs do not require slip rings, brushes and additional power supply for the field excitation. As a result, direct drive PMSGs topology given in Figure 1.7 became more popular in the last decade. The major disadvantage of PMSGs is high and unstable cost of PMs. Moreover, the topologies including PMs suffer from the risk of demagnetization due to high temperature or short circuit.

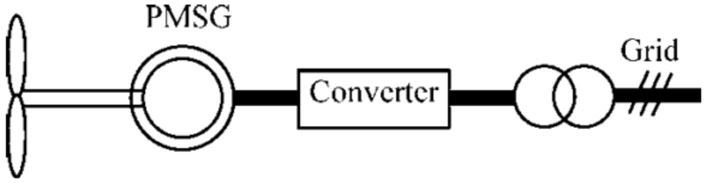

Figure 1.7: Direct drive PMSG topology [5].

Medium speed PMSGs coupled with single stage gearboxes given in Figure 1.8 also promise high efficiency and required PM and the total generator mass is much lower than those of direct drive PMSGs. Although the gearboxes and hence their disadvantages reappear in medium speed concept, the gearboxes utilized with medium speed generators are single and double stage gearboxes that are said to be more reliable than common three stage gearboxes [8]. There are few commercial examples of the medium speed PMSG concept but these products have not been much sought after in the market. Nonetheless, the academic research and comparative studies about medium speed concept continue.

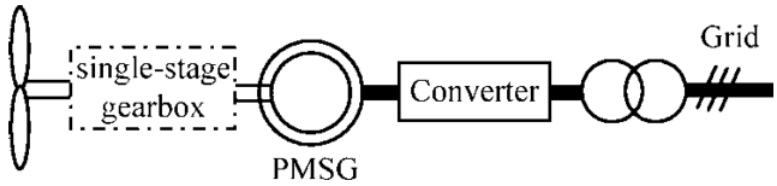

Figure 1.8: Medium speed PMSGs with single stage gearbox [5].

PMSGs can be classified according to flux path as radial, axial or transverse flux PM generators. Radial Flux Permanent Magnet (RFPM) machines are the most common PM generator topology in the wind industry since they have simpler and more stable structure.

All of the presented generator topologies have their own advantages and disadvantages considering the performance and cost trade-off. PMSGs are favorable in terms of performance but the investment cost is significant especially in case of direct drive utilizations. In addition, the maintenance cot is low in PM machines due to the absence of brushes and slip rings. The general properties mentioned under this section are summarized in Table 1.1.

Table 1.1: Comparison of generator topologies (+:Low, ++:Medium, +++:High, -:N/A).

Generator		**Efficiency**	**Reliability**	**Cost**		
				Investment	Maintenance	Power Converter
SCIG Geared		+	+++	+	+	-/+++
WRIG Geared		+	+	+	+++	-
DFIG Geared		+	+	+	+++	++
EESG	Direct Drive	++	+	+++	+++	+++
	Geared	++	+	++	+++	+++
PMSG	Direct Drive	+++	+++	+++	+	+++
	Geared	+++	+++	++	+	+++

1.2 Hybrid Excited Generators

Although high speed DFIGs still dominate the market, direct drive PMSG systems became attractive due to high power density and efficiency where these features became more important as the power ratings of wind turbines progressively increase. In addition, getting rid of reliability issue of gearboxes makes direct drive PMSG systems preferable for offshore wind turbines in which the maintenance cost and downtime are crucial. However, direct drive PMSGs contain hundreds of kilogram PM that is expensive and difficult to handle in the manufacturing process. Furthermore, PMs induce uncontrollable voltage in contrast to generators with DC excited field windings. Therefore, these drawbacks of the most attractive topology among the commercially available options motivated researchers to come up with a new topology. Although hybrid excited machines, making use of both PMs and DC excited field windings, had not been specifically proposed for wind turbine generators; they offer cheap and flexible systems for wind energy.

The main idea behind the hybrid excited machines is to provide the MMF by using both PM and the field winding excitation. The benefits of the concept include reduction in the amount of PM and field strengthening/weakening possibility. Moreover, hybrid excited generators can produce power in case of a loss of field winding or open circuit, thanks to PM excitation [9].

Hybrid term in this sense appeared for the first time in a patent published back in 1987 [10] where field coils included in between the two PM machine stators function as a control coil to vary the output voltage. Later on, hybrid excitation phenomenon became a topic of interest among researchers. A machine with PMs and field windings on the same rotor creating parallel flux paths is suggested in [11]. The six pole machine is proposed to combine the power density of the PM machines and the field regulation capability of conventional synchronous machines. PM poles as seen in Figure 1.9 are supposed to provide a major part of air gap flux whereas field weakening/strengthening is achieved by changing the flux density under the excitation poles. Another property of the given topology is that the armature reaction inductance is said to be lower than conventional synchronous machines and higher than PM machines. However, it is pointed out that weakening the field at high speeds may promote stator core loss as there exist a high flux density region in the stator between two adjacent PM poles.

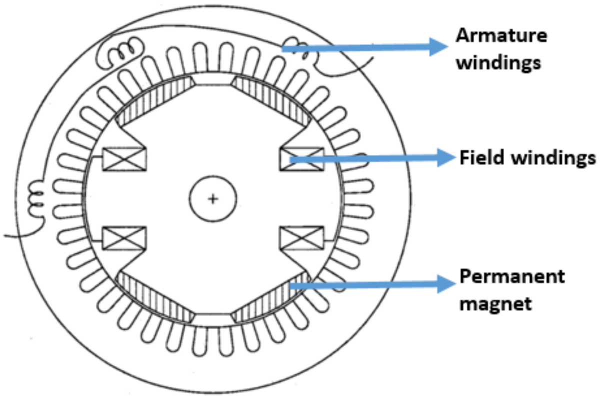

Figure 1.9: Structure of hybrid machine proposed in [11] .

Variations of Doubly Salient Permanent Magnet (DSPM) machine topology proposed in [12], constructed the basis of several studies about hybrid excitation machines especially for electric car applications [13–17]. In [13], Chau suggested that flux weakening/strengthening is enabled by adding an extra flux path in parallel with each PM pole while the stator carries both of the polyphase armature and DC field windings as seen in Figure 1.10. In a subsequent study [18], the doubly salient structure is modified by adding an extra air bridge in shunt with PMs so that the effect of flux weakening/strengthening is amplified and a small DC field excitation yields wider flux regulating range. It is claimed that although the generator is proposed for a standalone low-voltage battery-based power systems, it is applicable to the large scale wind systems. Figure 1.11 illustrates the generator structure and the equivalent magnetic circuit of the suggested topology.

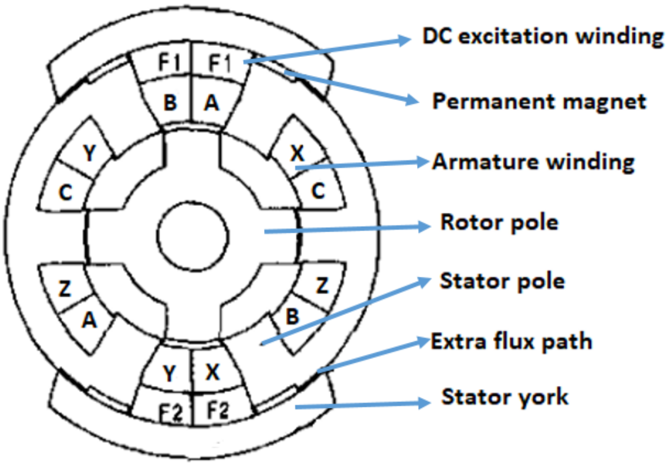

Figure 1.10: Stator Doubly Fed Doubly Salient PM (SDFDS-PM) machine topology [13].

A more common structure of DSPM based hybrid machines is given in Figure 1.12. Stator core encloses the PMs beside containing both armature and field windings. Rotor structure is very simple as there is no PMs, windings or brushes. Saturated magnetic bridges are usually included in this configuration as they enable the stator laminations to be sticked together and amplifies the effect of DC field flux due to their low reluctance [14].

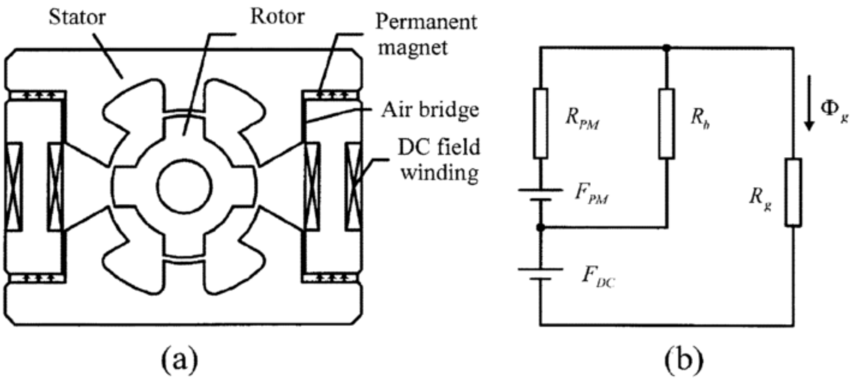

Figure 1.11: PM brushless hybrid generator with air bridge [18]. (a)structure. (b)magnetic circuit.

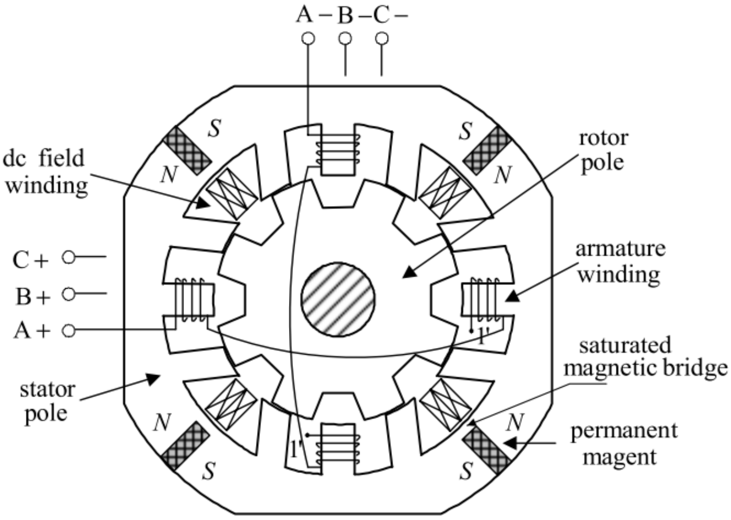

Figure 1.12: Hybrid excited doubly salient machine propesed in [14].

A similar principle is applicable to the flux switching PM machines since the excitation sources are located in the stator just as DSPM machines. It is possible to contain the field windings external or wrapped around the PMs embedded in the stator [19].

Doubly salient stators may also be used as an outer layer of dual-stator structures where both PM and field winding excitations are integrated in the inner stator to reduce the overall size and mass. Moreover, by using outer rotor, direct coupling with wind blades is enabled and constant output voltage range is widened [20]. Double layer stator may be utilized also with inner rotor [21]. Structural model of inner rotor dual-stator hybrid excited generator is given in Figure 1.13. The PMs in this structure are included in the rotor and the field winding is fixed on the shell with the inner stator. It is claimed that the topology is beneficial for wind energy utilizations since both power density and output voltage are increased.

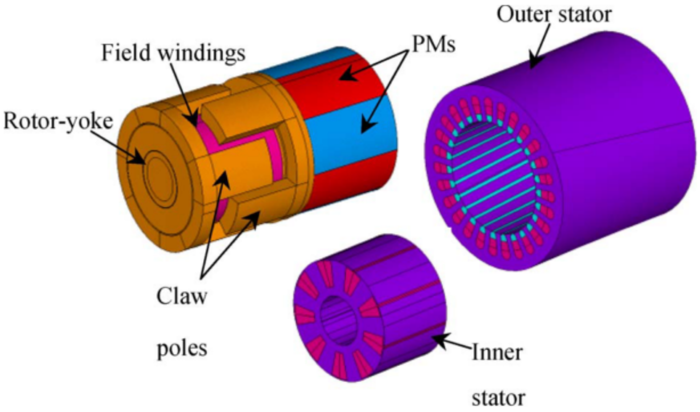

Figure 1.13: Structural model of dual stator hybrid excited wind generator [21].

A variation of dual-stator structure is given in [22] where concentrated armature windings lay in the outer stator whereas inner stator houses surface mounted PMs and field windings as seen in Figure 1.14. The topology is claimed to have attractive flux regulation capability since PM or Wound Field (WF) flux can loop through the adjacent pole individually unlike the series hybrid machines where both flux components have the same flux path. This configuration also requires no slip rings and the torque density is high thanks to the double stator structure. However, the fact that excitation poles are not completely balanced may result in deterioration of the back-EMF.

In [23], a consequent-pole PM whose structure is given in Figure 1.15 is proposed to have a wide range of control on air-gap flux with minimum field excitation. The rotor is divided into two sections consisting of surface mounted PMs and laminated iron poles. Conventional stator structure with armature winding is altered by adding a circumferential field winding in the middle of the stator so that externally controllable DC excitation is achieved without brushes or slip rings. However, this magnetically complex structure reduces power density while increasing material requirement and core losses in addition to causing manufacturing difficulties.

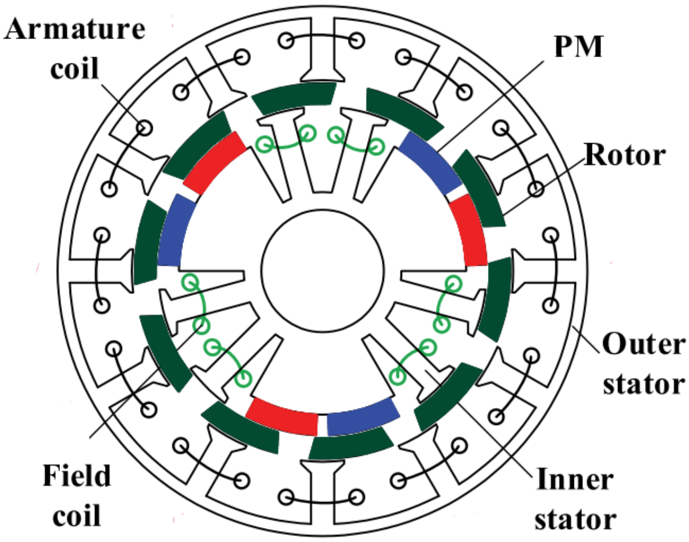

Figure 1.14: Schematic of partitioned stator hybrid excited machine [22].

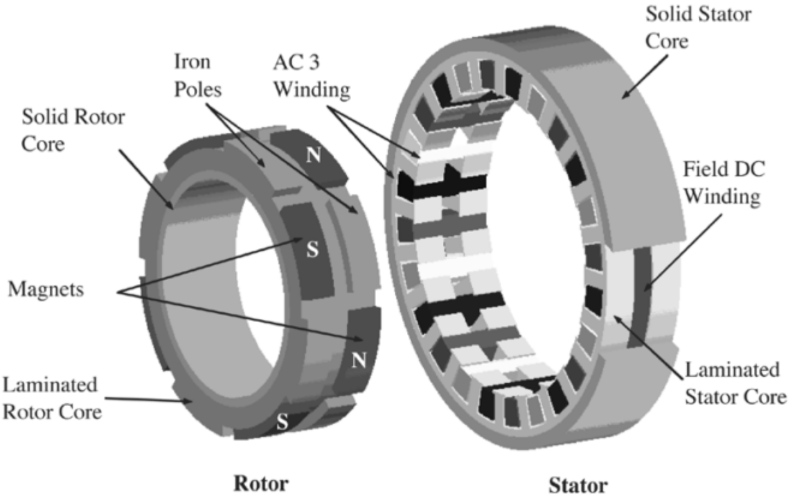

Figure 1.15: Structure of consequent pole PM machine [23].

So far, the discussed studies are focused on low power/high speed applications. A different approach is presented by Beik and Schofied in [24] with the introduction of high voltage hybrid generator containing two separate rotors. The main focus was the elimination of controlled rectifier in power converter stage. Later on, the authors explained the design procedure of a 5 MW 600 rpm hybrid wind turbine generator [25]. Figure 1.16 illustrates the proposed topology where PM and WF rotors share the same stator while a brushless exciter with a separate stator is used to have no brush or slip rings. Both of the WF and surface mounted PM rotors are coupled on the same shaft. Output voltage is resulted from the combination of the fixed field from the PM rotor and a variable filed from WF rotor. Therefore, the output voltage is controllable over a range that design of the WF rotor allows. Nine phase armature winding is also preferred to increase power density and decrease DC-link voltage ripple.

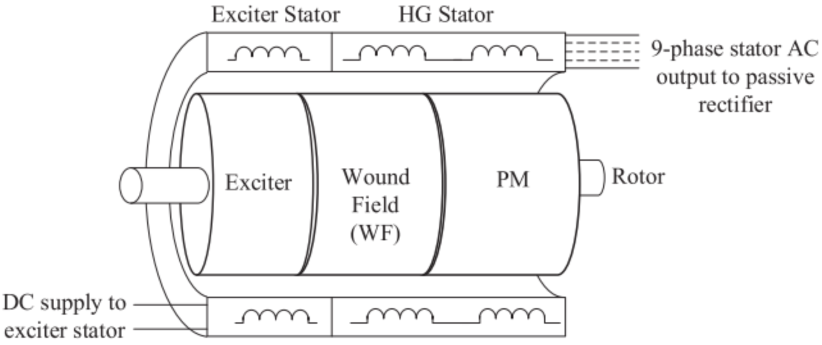

Figure 1.16: Schematic of hybrid generator proposed in [25].

Although topology given in Figure 1.16 is proposed for high power wind turbine applications, the predicted speed in [25] is in the medium speed range which still necessitates a gearbox. A scale-down direct drive application of a hybrid excited machine is proposed in [26] where dual stator structure is preferred. Both rotor and outer stator include PM-iron pole sequences to provide PM excitation and flux modulation at the same time whereas armature windings are wound in inner stator and field windings lay in the outer stator. The design is suggested for direct-drive utilization, since the major harmonics are synchronous and they contribute the electromagnetic torque generation to achieve high torque density. Regulation of the back EMF by changing the field current is again possible for this hybrid excited machine. However, this topology may not be economically feasible for a full scale direct drive application due to excessive PM requirement.

To sum up, doubly salient hybrid excited machines are generally preferred in high speed applications. There are various dual stator topologies suitable for wind turbines promising high power and/or torque density. However, these electromagnetically complex structures may be commercially infeasible due to high material and manufacturing costs. Among the hybrid excited synchronous machines discussed under this section, structure combining WF and PM rotors suggested in [25] is used as a base in the following parts of the thesis to design a direct drive hybrid excited synchronous generator and make comparison among conventional direct drive topologies. Although, this hybrid configuration is no different from the other topologies considering the level of completeness as they are all only tested on prototypes in low power scale, the concept is easier to apply since two separate rotors are conventional PM and WF rotors. There are no limitations on power or torque level since the direct drive applications of surface mounted PM and WF synchronous generators are well-known.

1.3 Scope of the Thesis

This thesis focuses on electromagnetic design and analysis of direct drive synchronous generators having different excitation sources; namely PM, WF and hybrid excitation which is basically the combination of former two excitation types. The main approach is based on cost optimization using analytical model of WF and PM synchronous machines and the FEM simulations of the resulting designs. The study aims to discuss the feasibility of hybrid excitation concept for direct drive wind turbine applications by comparing a sample hybrid excited synchronous generator (HESG) design with a PMSG and a EESG at the same ratings. As a new concept, hybrid excitation promises controllability and flexibility but the performance and capabilities of such generators need to be investigated. Although, it is expected to have performance ratings in between those of EESG and PMSG, the characteristics of HESGs remain unknown due to lack of studies in the literature.

The outline of the rest of the thesis is as follows:

In Chapter 2, how the 2.5 MW 16 rpm direct drive EESG and PMSG are designed to construct a reference point to discuss the hybrid excitation is explained. To mathematical models of the generators are summarized and sample designs for each topology are obtained using Genetic Algorithm optimization. Afterwards, these designs are simulated and verified by FEM simulations in ANSYS Maxwell environment.

In Chapter 3, the principle applied in Chapter 2 is adapted to design the selected hybrid excited synchronous generator topology which is a machine with two separate rotors for two different excitations coupled on the same shaft and sharing the same stator. The dominance of WF and PM excitation sections and the effects of it on the performance are investigated. According to the results of multi-objective optimization, the excitation percentages are determined and the resulting design is given.

In Chapter 4, 2D and 3D FEA results of the hybrid excited synchronous generator designed in Chapter 3 are given. The feasibility of the design approach given in Chapter 3 is discussed and the simulation results are evaluated.

In Chapter 5, given 2.5 MW 16 rpm direct drive EESG, PMSG and Hybrid Excited Synchronous Generator designs are compared in terms of cost, mass and performance. The discussion on performance includes THD of induced voltage, short circuit characteristics, efficiency and power factor. The dimensions and parameters of the designs are presented and compared.

CHAPTER 2

DESIGN OF 2.5 MW DIRECT DRIVE WIND TURBINE GENERATOR

2.1 Introduction

In the previous chapter, common generator topologies in the wind industry are discussed and the main attributes and variations of hybrid excited synchronous generators are analyzed. The discussion is concluded by choosing the two rotor hybrid generator topology to be investigated further. In order to evaluate the performance of the direct drive hybrid generator to be designed, desired reference points are constructed in terms of mass, cost and performance of conventional direct drive wind turbine generators used in the industry. In this chapter, the design and analysis procedure of 2.5 MW direct drive PMSG and EESG is conveyed.

According to the statistics recorded in 2017 in Turkey, 92% of the wind energy was generated by the wind turbines rated 2 MW and above [27]. Although dominated by high speed DFIGs, the conjuncture of onshore wind industry promotes the selection of 2.5 MW scale as the base power rating of the designs. In 2-3 MW range, a rotational speed of 15-18 rpm is common among commercial direct drive PMSG and EESG based wind turbines. The rotor speed drops 10-12 rpm as the rated output power gets higher. In Table 2.1, several direct drive wind turbine models are presented. In compliance with the commercial products, the nominal rotor speed is selected to be 16 rpm for the 2.5 MW generators to be designed.

Terminal voltages of available wind turbine generators vary between 690-3300 V. Although higher terminal voltages reduces the required current at the same power and results in higher efficiency, the generators with terminal voltages of kV level require different safety measures in manufacturing and maintenance processes than the ones with low terminal voltages. In this study, the rated voltage of the designs is selected as 690 V.

Table 2.1: Examples of commercial direct drive wind turbines around 2 MW scale.

Model	Generator Type	Power	Speed	Diameter	Weight
Enercon-E92 [28]	EESG	2.35 MW	5-16 rpm	-	-
Enercon-E82 [28]	EESG	2.3 MW	6-18 rpm	-	62 t
Enercon-E115 [28]	EESG	3 MW	4-12.8 rpm	-	-
Zephyros [29]	PMSG	1.5 MW	18 rpm	4 m	40 t
NewGen [30]	PMSG	4 MW	19 rpm	9 m	37 t
Switch 1650-17 [31]	PMSG	1.65 MW	17 rpm	-	50 t
Switch 3200-12 [31]	PMSG	3.2 MW	12 rpm	$\sim$6 m	80 t

Under this chapter, the design process of 2.5 MW 16 rpm direct drive PMSG and EESG is conveyed. Each generator is designed based on the analytical model constructed on MATLAB. The material cost of the generator is selected as the objective function of the optimization problem.

The analytic models, optimization process and finite element analysis (FEA) results are shared in the following sections.

2.2 Design of 2.5 MW Electrically Excited Synchronous Generator

2.2.1 Optimization Process Based on Analytical Model

The aim is to obtain the optimum EESG design by constructing an objective function on MATLAB which calculates the material cost using independent variables and dimensions. In this sense, firstly, the performance requirements and criteria are determined. The independent variables are selected and afterwards, the mathematical model is created step by step. The obtained objective function is used in optimization process in which Genetic Algorithm (GA) available in Optimization toolbox of MATLAB is preferred.

2.2.1.1 Constraints and Constant Values

Based on literature survey and the some industrial products, some of the dependent variables are restrained to keep the dimensions and flux densities in a reasonable range. In addition to constraints, some values are pre-defined and kept constant. These restrictions can be summarized as follows;

- The outer diameter is limited to 5.5 meters for manufacturing and transportation limitations.
- The tooth width must be thicker than 15 millimeters so that the teeth can endure the mechanical stress.
- The maximum flux density in the back cores and teeth are set to 1.6 and 2 T, respectively.
- The number of slots per pole per phase is decided to be equal to 2 since increasing it further causes manufacturing process to be harder considering tooth thickness, although greater number of slots would result in more sinusoidal flux density in the air-gap [32], [33].
- The fill factors for armature and field windings are selected considering the required space for insulating materials around the conductors.
- Tooth tips of the stator core are assigned independent from the varying dimensions. As illustrated in Figure 2.1, the total tooth lip height, h_{tl} is accepted as 6 millimeters.
- Pole embrace ratio, i.e. the ratio of pole shoe over pole pitch, is taken to be equal to 0.72 to arrange the angle of the magnet arc such that 11^{th} harmonic of the air-gap flux density is minimized [34].

The performance criteria regarding efficiency and power factor are enforced by means of penalty functions as a very large coefficient is multiplied by the difference between calculated and allowed top values and added up to the objective function. The other constrained variables having penalty coefficient are outer diameter, D_o, tooth width,

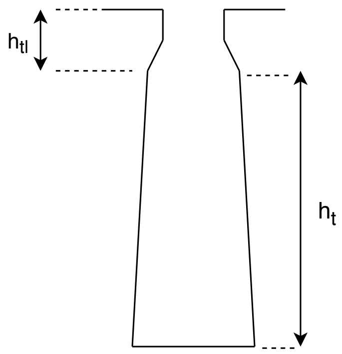

Figure 2.1: Stator slot and tooth lip heights.

t_w and the tooth flux density, B_t. The constrained variables and their limits are summarized in Table 2.2.

Table 2.2: Performance criteria and the limited variables.

Variable/Parameter	**Criteria**
Outer diameter, D_o	<5.5 m
Tooth width, t_w	>15 mm
Efficiency, η	>93%
Power factor, pf	>0.9
Tooth flux density, B_t	<2 T

2.2.1.2 Construction of the Objective Function

After setting the constants and determining the constraints, dimensions and dependent parameters are formulated in terms of independent variables of the optimization. The formulation process can be divided into for main steps as illustrated in Figure 2.2.

The input of the block I is the design vector containing the independent parameters. These parameters are subjected to upper and lower bounds specified before the execution of Genetic Algorithm (GA).

The first block calculates maximum flux density values, main dimensions and number of turns using the design vector and given constant values. The flat top and average

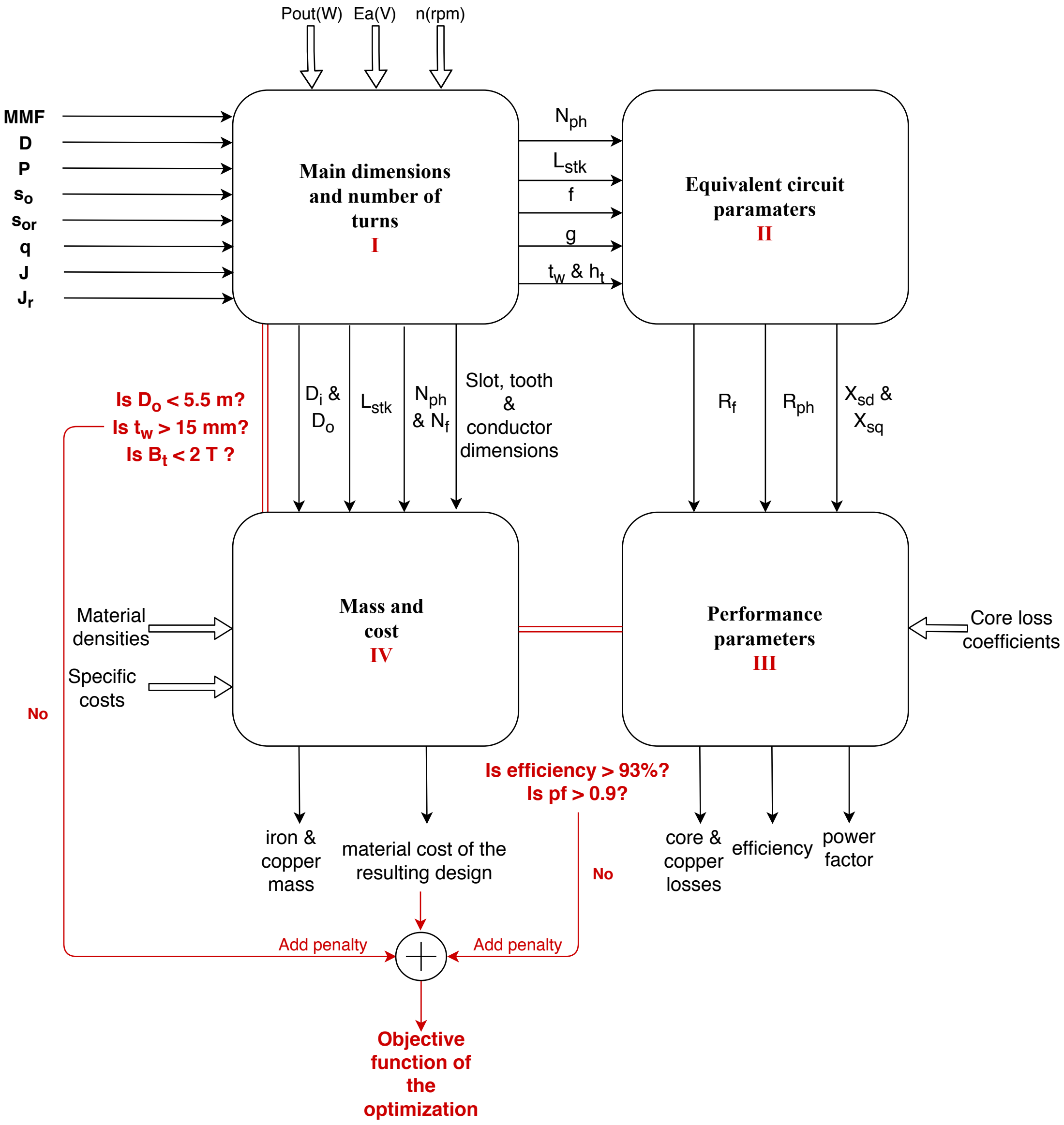

Figure 2.2: Construction of the objective function based on analytical calculations for EESG.

values of the air gap flux density, B_g and B_{avg} respectively, are calculated as given in Eq. (2.1) and (2.2) where g_{eff} is the effective air gap length calculated using the Carter's coefficient and τ_p is the pole embrace ratio. It is important to point out that the air gap length is empirically chosen to be equal to the 0.1% of the selected outer diameter limit.

$$B_g = \frac{\mu_0}{g_{eff}} MMF \tag{2.1}$$

$$B_{avg} = \frac{8}{\pi^2} B_g sin(\tau_p \frac{\pi}{2}) \tag{2.2}$$

The rated electromechanical torque, T_{em} is obtained by using constant power and speed ratings decided earlier. The stacking length of the generator, L_{stk}, is calculated using the main torque relation given in Eq. (2.3). The number of turns per phase, N_{ph}, is derived from the induced voltage equation as seen in Eq. (2.4) where k_w is the winding factor, D is the bore diameter, f is the frequency, q is the electrical loading and A_p is the area per pole.

$$L_{stk} = \frac{4\sqrt{2}T_{em}}{\pi^2 B_{avg} q k_w D^2} \tag{2.3}$$

$$N_{ph} = \frac{E_a}{4.44 k_w f B_{avg} A_p} \tag{2.4}$$

The backcore heights of stator, h_{sbc} and rotor, h_{rbc} is determined according to the allowed flux density in the cores. The tooth height, h_t is calculated considering the electric loading, armature current density, the fill factor and total height of the tooth lips, h_{tl}. Eq. (2.5) shows the calculation of the outer diameter, D_o.

$$D_o = D + 2(h_{sbc} + h_t + h_{tl}) \tag{2.5}$$

The number of turns of the field windings is calculated by simply dividing the MMF value provided in the design vector to the field excitation current, I_f which is accepted as 55 A in the design process as seen in Eq. (2.6). The value of the excitation current can be altered later to observe its effects on induced voltage.

$$N_f = \frac{MMF}{I_f} \tag{2.6}$$

After obtaining the main dimensions, the equivalent circuit parameters can be calculated. The calculation of armature and field winding resistances, R_{ph} and R_f, is given in Eq. (2.7) and (2.8) respectively using the mean length of winding turn in a coil,

LMC and conductor area, A_{co} for the armature and their rotor equivalents with subscript r for the field where a is the number of parallel paths which is set to be equal to the number of poles, p, in this study.

$$R_{ph} = \frac{\rho_{cu} LMC N_{ph}}{A_{co} a^2} \tag{2.7}$$

$$R_f = \frac{\rho_{cu} LMC_r N_f}{A_{cor}} \tag{2.8}$$

From Eq. (2.9) to (2.12), the calculation procedure of D and Q axis equivalent reactances is summarized. Firstly, equivalent self inductances are obtained using D and Q equivalent reluctances. The mutual inductances which are equal to the one third of the self inductances and the leakage inductance which is taken to be 15% of the D axis component of self inductance, L_d are added up the self inductance values. Lastly, the D and Q equivalent reactances are obtained using the angular frequency.

$$L_d = \frac{\frac{8}{\pi} \mu_0 D L_{stk} (k_w N_{ph})^2}{p^2 g_d} \tag{2.9}$$

$$L_q = \frac{\frac{8}{\pi} \mu_0 D L_{stk} (k_w N_{ph})^2}{p^2 g_q} \tag{2.10}$$

$$L_{sd} = L_d + L_{leakage} + \frac{L_d}{3} \quad \& \quad L_{sq} = L_q + L_{leakage} + \frac{L_q}{3} \tag{2.11}$$

$$X_{sd} = 2\pi f L_{sd} \quad \& \quad X_{sq} = 2\pi f L_{sq} \tag{2.12}$$

The equivalent circuit parameters are used to calculate the losses, efficiency, terminal voltage and power factor in the third block of the design chart. The main sources of losses are copper and core losses which are obtained as given in Eq. (2.13) to (2.16). While the armature and field copper losses are calculated easily by using resistances, the core loss calculation requires hysteresis and eddy loss coefficients, k_h and k_e in addition to the tooth and backcore masses, M_t and M_{bc}. The efficiency is calculated as given in Eq. (2.17) neglecting the windage and friction losses.

$$Pcu_a = 3R_{ph}I_a^2 \quad \& \quad Pcu_f = pR_fI_f^2 \tag{2.13}$$

$$M_t = \rho_{iron}L_{stk}N_{slot}t_w(h_t + h_{tl}) \tag{2.14}$$

$$M_{bc} = \rho_{iron}L_{stk}(0.25\pi D_o^2 - (D + 2h_t + 2h_{tl})^2) \tag{2.15}$$

$$P_{core} = M_t(k_hfB_t^{nn} + k_ef^2B_t^2) + M_{bc}(k_hfB_{bc}^{nn}k_ef^2B_{bc}^2) \tag{2.16}$$

$$\eta = \frac{P_{out}}{P_{out} + P_{core} + Pcu_a + Pcu_f} \tag{2.17}$$

The terminal voltage of the generator is calculated as given in Eq. (2.18). It is important to note that to achieve vector control conditions, I_d is set to zero and $X_{sd}I_d$ term vanishes. Both E_a and I_q lay on the Q axis. Therefore, the angle between V_t and Q axis is the power angle and the power factor is the cosine of this angle.

$$V_t = E_a - R_{ph}x(I_q + jI_d) + X_{sd}I_d - jX_{sq}I_q \tag{2.18}$$

The last block of the design works as a mass and cost calculator using the results of Block I. The calculation of copper mass, M_{cu} containing the armature, Mcu_a and field windings Mcu_f and iron mass, M_{iron} containing the stator, M_{stator} and rotor masses M_{rotor} are given in Eq. (2.19) to (2.21) where N_{slot} is the number of slots, W_p is the width of the rotor poles, D_r is the rotor diameter excluding the pole shoes and D_i is the inner diameter of the rotor.

$$Mcu_a = 3\rho_{cu}N_{ph}A_{co}LMC \quad \& \quad Mcu_f = P\rho_{cu}N_fA_{cor}LMC_r \tag{2.19}$$

$$M_{stator} = \rho_{iron} L_{stk} [0.25\pi (D_o^2 - (D + 2h_t + 2h_{tl})^2 + N_{slot} t_w (h_t + h_{tl}))] \quad (2.20)$$

$$M_{rotor} = \rho_{iron} L_{stk} [\tau_p 0.25\pi ((D - 2g)^2 - D_r^2) + pW_p h_{tr} + 0.25\pi ((D_r - 2h_{tr})^2 - D_i^2)] \quad (2.21)$$

Calculated masses are multiplied with the specific cost values to obtain the main material expenditures of the design. The objective function C is achieved after the penalty function is added to the total material cost as Eq. (2.22) reveals. Penalty function includes penalty coefficients multiplied with penalty values for each constraints defined in Table 2.2.The specific costs of the material used are given in Table 2.3.

Table 2.3: The costs per kg of the main materials used in the generators [35].

Material	**Specific Cost**
Iron	3 \$/kg
Copper	10 \$/kg
Permanent Magnet	80 \$/kg

$$C = 10 \frac{\$}{kg} M_{cu} + 3 \frac{\$}{kg} M_{iron} + penalty \quad function \quad (2.22)$$

2.2.2 Optimization Results

The constructed objective function is aimed to be minimized where Genetic Algorithm (GA) is chosen as solver in MATLAB optimization toolbox. The convergence of the algorithm to the optimum cost is given in Figure 2.3. The active mass of the resulting design is calculated to be 33 tonnes corresponding to a material cost of approximately 140 k\$. The design vector yielding the optimum design are given in Table 2.4. It is important to note that the number of pole pairs is enforced to be an integer.

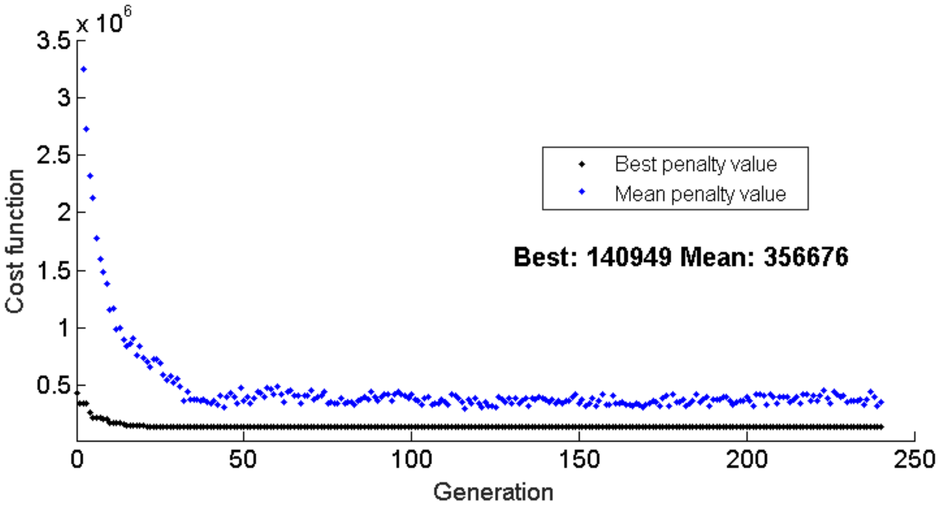

Figure 2.3: Convergence of the GA.

Table 2.4: The resulting design vector.

The Design Variable	Optimization Result
MMF	5766 A
Stator bore diameter, D	5222 mm
Number of poles, P	100
Stator slot opening ratio, s_o	0.3
Rotor slot opening ratio, s	0.43
Electrical loading, q	$40,470$ A/m
Armature current density, J	$4.2x10^6$ A/mm^2
Field current density, J_r	$3.2x10^6$ A/mm^2

The main dimensions of the resulting design are given in Table 2.5 whereas the important parameters and mass values are summarized in Table 2.6 and 2.7. 3D and 2D model of the optimum design are given in Figure 2.4 and 2.5, respectively. The unit of the dimensions is millimeters.

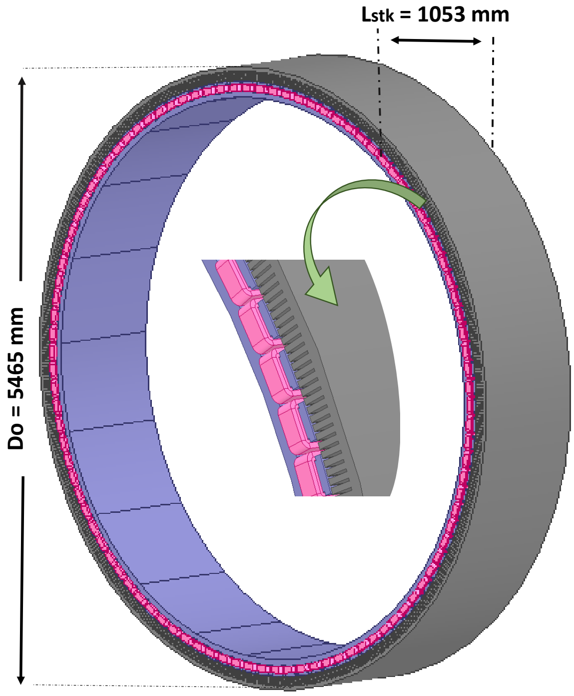

Figure 2.4: 3D view of the optimum EESG.

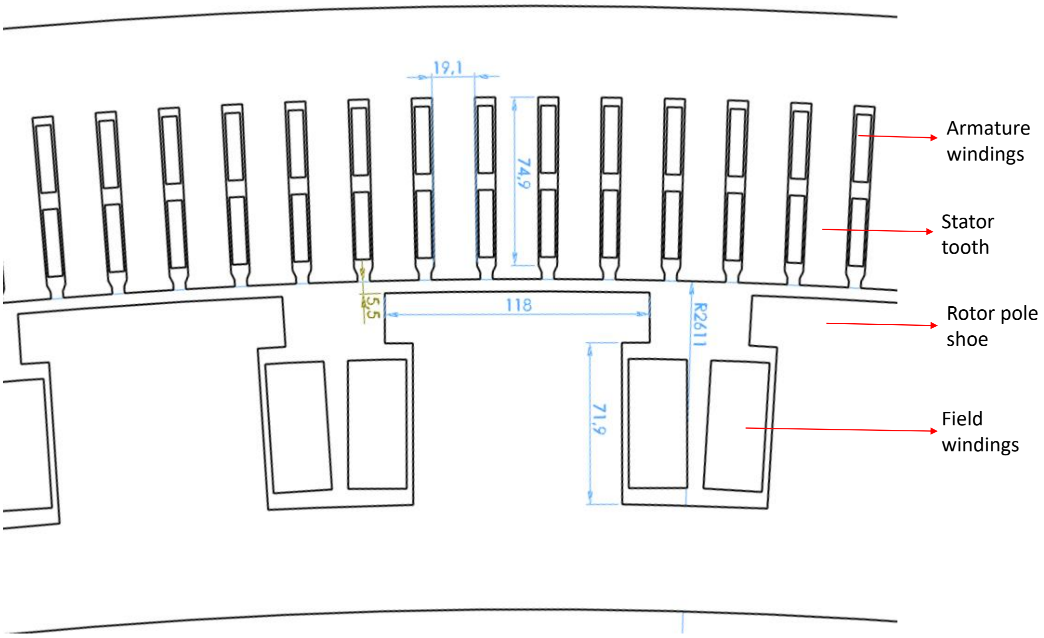

Figure 2.5: 2D model of the optimum EESG.

Table 2.5: The main dimensions of the resulting design.

Dimension	Value
Outer Diameter, D_o	5465 mm
Stacking length, L_{stk}	1053 mm
Air gap length, g	5.5 mm
Tooth width, t_w	19.1 mm
Stator tooth height, h_t	74.9 mm
Rotor tooth height, h_{tr}	71.9 mm
Width of pole shoe, W_{ps}	118 mm
Inner diameter, D_i	4928 mm

Table 2.6: The main parameters of the resulting design.

Parameter	Value
Number of conductors per slot, N_a	52
Number of slots, s	600
Number of turns in field windings, N_f	105
Phase resistance of armature windings, R_{ph}	5.1 mΩ
Q axis equivalent inductance, L_q	0.66 mH
D axis equivalent inductance, L_d	0.73 mH

Since in the analytical model, the rated values are defined first and the parameters are calculated each time the design vector input is changed; the power and voltage ratings of the resulting design may slightly differ from the selected values. This is mainly because the flux density in the air-gap is modulated each time according to the calculated dimensions for a given design vector so that stator teeth does not saturate. As a result, the induced line voltage of the optimum design is calculated to be 667 V where the resulting EESG can be still classified as a 690 V machine.

Table 2.7: The performance parameters of the resulting design.

Parameter	Value
Induced line voltage (rms), E_a	$667.2V$
Power factor, pf	0.9
Core loss, P_{core}	20.1 kW
Armature copper loss, Pcu_a	77.1 kW
Efficiency, η	93%
Iron mass, M_{iron}	27.2 t
Copper mass, M_{cu}	5.9 t
Material mass, M	33.1 t
Material cost, C	140.9 k$

2.2.3 Electromagnetic Finite Element Analysis

The optimum design is simulated on ANSYS Maxwell to verify the calculated parameters and discuss the feasibility of the designed generator. The design vector and calculated parameters are used to construct the parametric model on RMxprt module. Afterwards, the model is exported as Maxwell 2D design. The line to line induced voltage at no load can be seen from Figure 2.6. The rms value of the fundamental component is measured to be 672 V. The 5 V difference between the analytical calculations and simulation is due to the approximating of the leakage flux and neglecting the harmonic components in the analytical model.

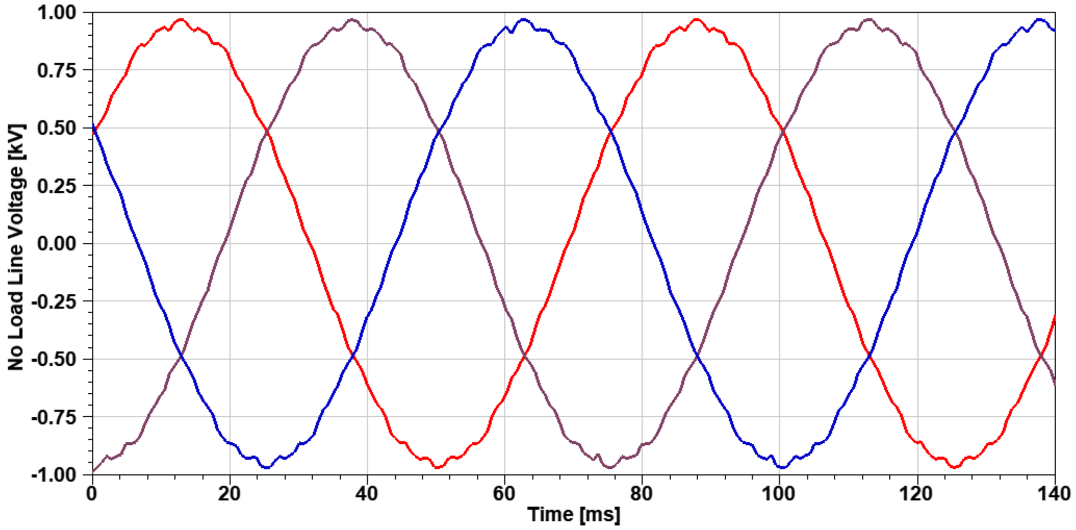

Figure 2.6: No load line to line induced voltage at 16 rpm.

According to 2D simulation, no load torque ripple, i.e., the cogging torque has a peak to peak value over 100 kNm (Figure 2.8) whereas full load torque oscillating over the rated value is given in Figure 2.7. The cut-in speed of wind turbines depends on the cogging torque, as the starting performance is highly effected by no load torque ripples. Hence, the cogging torque is expected to be lower than 1.5-2.5% of the rated torque [36].

The cogging torque is estimated to be nearly 8% percent of the rated torque for this design. It is known that modifying slot opening width, pole embrace ratio, pole shoe shape or skewing rotor/stator can significantly reduce cogging torque [37–42]. Nevertheless, it is decided to not to make any further modifications onto the optimization results in this level of the design.

After analyzing the behavior of the generator at no load condition, current excitation is applied to the armature windings to simulate the full load condition. The flux density distribution under full load is given in Figure 2.9. The flux density in the rotor backcore is recorded to be in the 1.6-1.7 T band, whereas it can reach up to 1.8 T in the region of pole shoe which faces the excited armature phase at that moment.

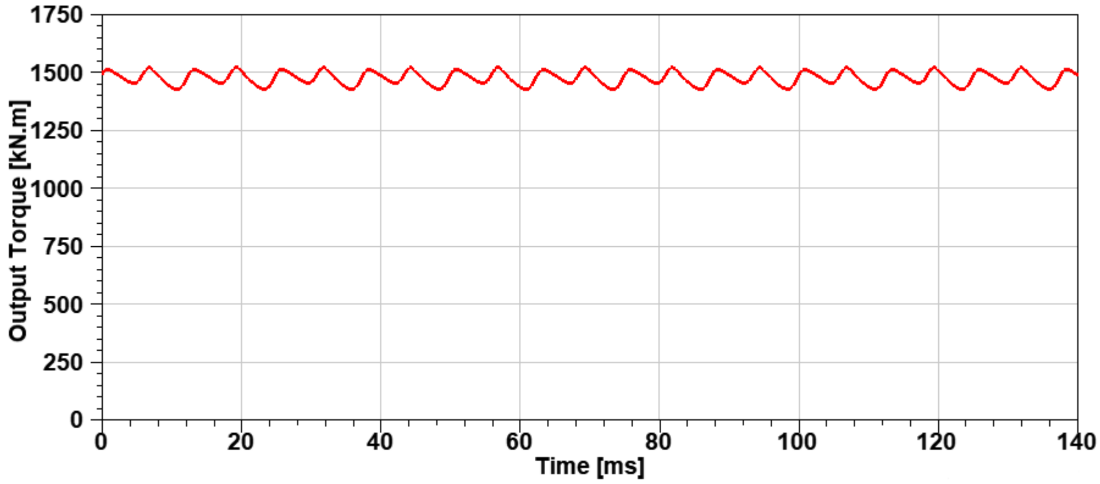

Figure 2.7: Output torque of EESG under full load.

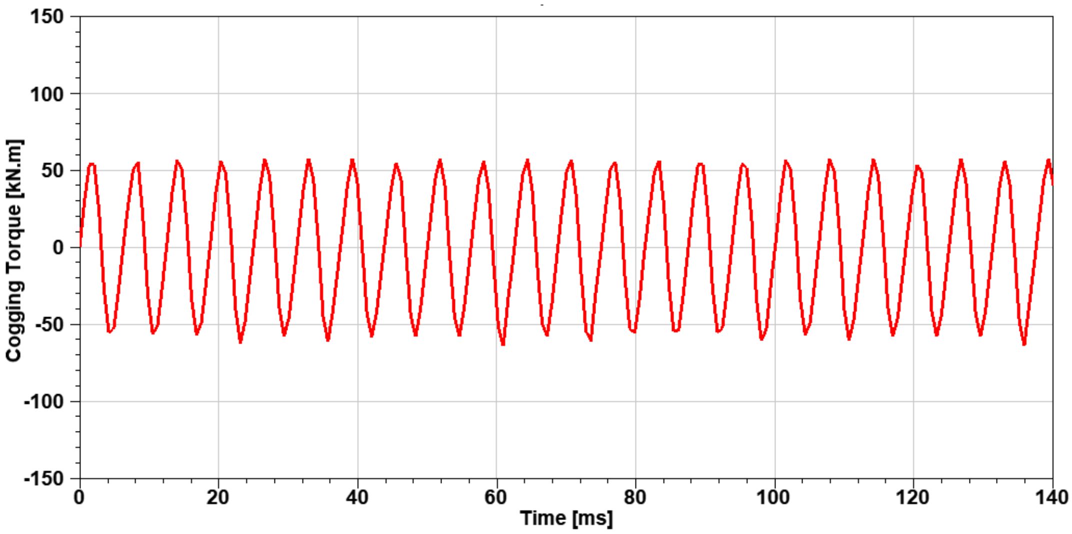

Figure 2.8: Cogging torque versus time at 16 rpm.

The output power at the rated full load can be seen from Figure 2.10 where the average value is recorded as 2.45 MW. The ripples over the average value are due to the torque ripples as they have the same frequency.

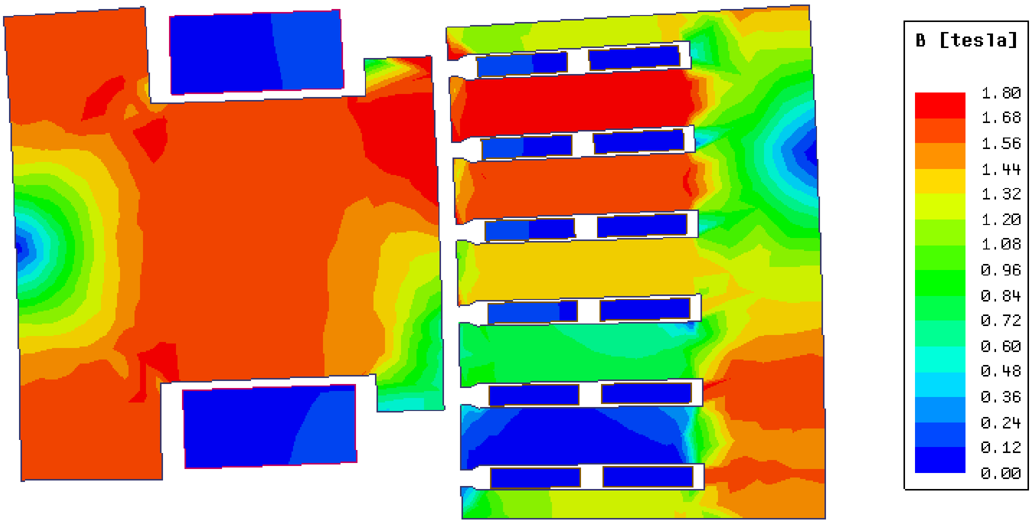

Figure 2.9: Flux density distribution under a pole at full load.

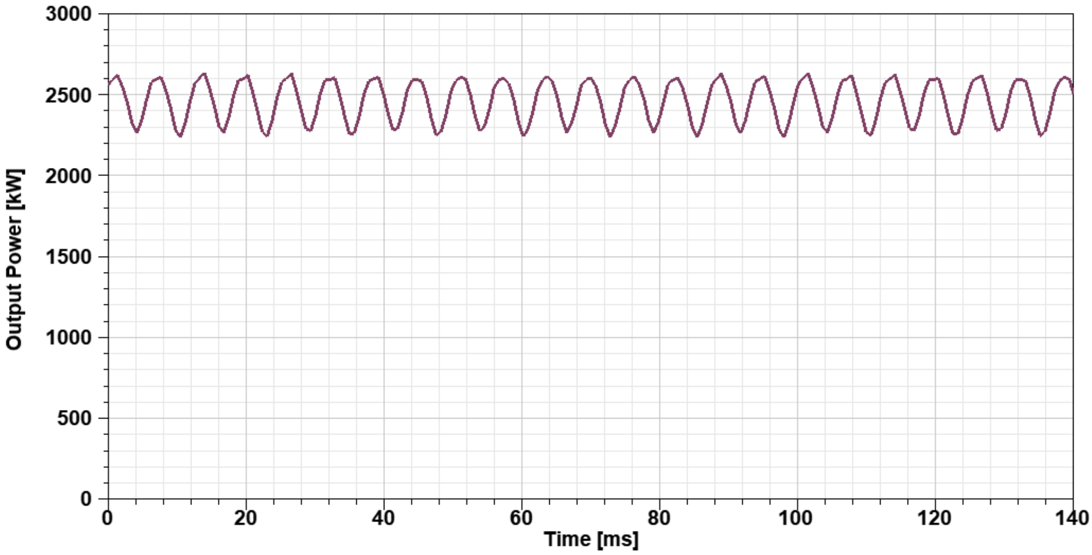

Figure 2.10: Output power versus time under full load.

2.3 The Design of Permanent Magnet Synchronous Generator

2.3.1 Optimization Process Based on Analytical Model

The process of PMSG design is very similar to the EESG design explained in the previous section. After determining the requirements and criteria, the mathematical model is used to construct the objective function to be minimized by GA.

The restrictions applied on the dimensions and parameters are nearly same for the PMSG design. Bore diameter is selected to be equal to that of the EESG designed in the previous section. The parameters accepted to be constant or limited can be summarized as listed under section 2.2.1.1. The parameters which have penalty coefficients are as listed in Table 2.2 whereas the only difference is the efficiency criteria set to 95$\%$ since the efficiency is expected to be larger due to elimination of the losses on the field windings.

2.3.1.1 Construction of the Objective Function

The construction of the objective function is illustrated in Figure 2.11. Again the process is similar to that of ESSG where properties of PM are added to the predefined constants. The design vector contains magnet thickness L_m, pole number P, slot opening ratio s_o, electric loading q and armature current density J since the bore diameter is decided to be equal to that of designed EESG in the previous section.

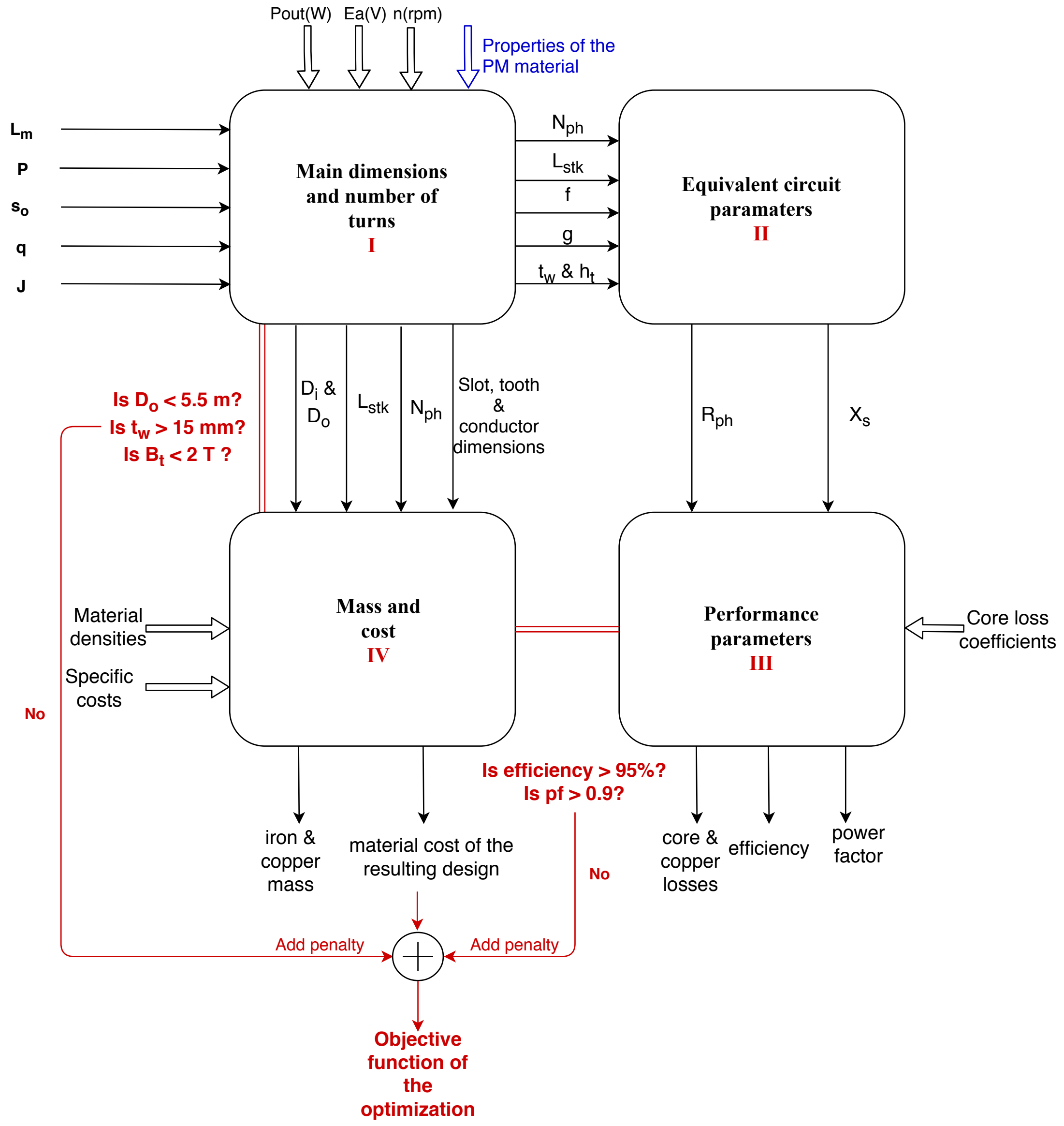

Figure 2.11: Construction of the objective function based on analytical calculations for PMSG.

The main properties of the chosen NdFeB permanent magnet for the study is given in Table 2.8.

The flux path in a PM machine and the equivalent circuit corresponding that flux are given in Figure 2.12, where P_{rl} represents the rotor leakage flux. As seen calculate the the average flux density in the air-gap, air-gap reluctance and magnet permeance are needed. Therefore, magnet area per unit axial length, A_{ml} is calculated first as given in Eq. (2.23). The calculation of magnet total permeance per unit axial length, P_{ml}

Table 2.8: Main properties of chosen NdFeB magnet.

Property	**Value**
Grade	30N
Remanence	1.2 T
Relative permeability	1.044

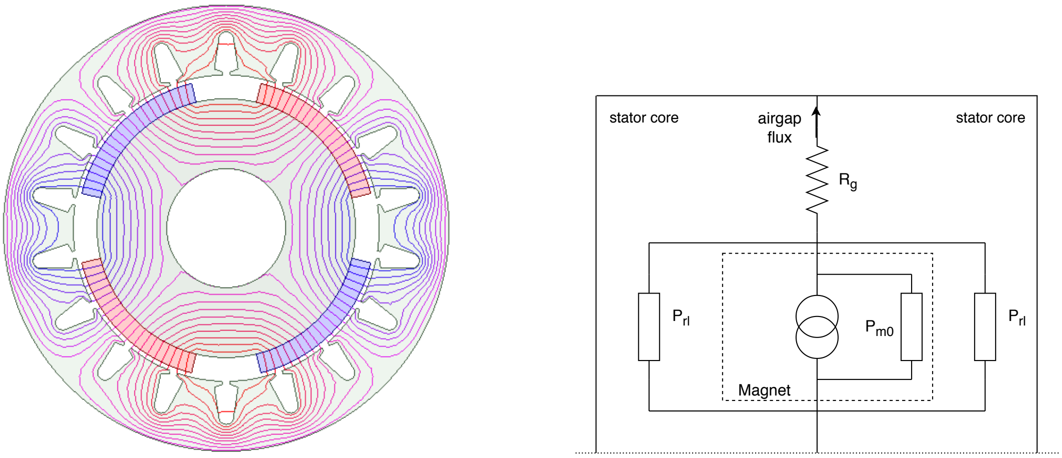

(a) Flux path in a 4 pole PM machines.

(b) Magnetic circuit of a pole.

Figure 2.12: Flux path and equivalent circuit of a pole for PM machines.

and air-gap reluctance per unit axial length R_{gl} are given in Eqs. (2.24) and (2.35), respectively where k_m is the magnet leakage flux coefficient and summation of P_{rl} and P_{mo} divided by length corresponds to P_{ml}.

$$A_{ml} = \frac{\tau_m \pi (D - 2g - L_m)}{P} \tag{2.23}$$

$$P_{ml} = \frac{k_m \mu_0 \mu_{rec} A_{ml}}{L_m} \quad \& \quad R_{ml} = \frac{1}{P_{ml}} \tag{2.24}$$

$$R_{gl} = \frac{g_{eff}}{\mu_0 [\frac{\tau_m \pi (D - g)}{P} + 2g]} \tag{2.25}$$

Flat top value of air gap flux density is obtained by using Eq. (2.26) where B_r is the magnet remanent flux density. Average value of the air-gap flux density is calculated using Eq. (2.27).

$$B_g = \frac{A_m}{\dfrac{\tau_m \pi (D-g)}{P} + 2g} \frac{B_r}{1 + P_{ml} R_{gl}} \tag{2.26}$$

$$B_{avg} = \frac{8}{\pi^2} B_g sin(\tau_m \frac{\pi}{2}) \tag{2.27}$$

The stacking length of the generator, L_{stk}, is calculated using the main torque relation given in Eq. (2.3) and the number of turns per phase, N_{ph}, is derived from the induced voltage equation as seen in Eq. (2.4) given under section 2.2.1.2. Moreover calculation of slot dimensions, outer diameter and phase resistance is also as given in EESG design process.

The phase inductance is calculated using magnet and air-gap reluctances, R_m and R_g, respectively as ginen in Eq. (2.28). The synchronous reactance, X_s is obtained by multiplying angular frequency with the synchronous inductance which contains self, mutual and leakage inductances per phase.

$$L_{ph} = \frac{N_{ph}^2}{4(R_g R_m)} \tag{2.28}$$

The relations governing the terminal voltage and the power factor are given in Eq. (2.29).

$$V_t = E_a - R_{ph} I_a - X_s I_a \quad \& \quad pf = \frac{|E_a| + |R_{ph} I_a|}{V_t} \tag{2.29}$$

The mass calculation is straightforward as given in Eqs. (2.19), (2.20) (2.30) and (2.31). Finally, the objective function is obtained as given in Eq. (2.32) by multiplying mass values with corresponding specific costs and adding the penalty function.

$$M_{rotor} = \rho_{iron} L_{stk} [0.25\pi (D - 2g - 2L_m)^2 - D_i^2] \tag{2.30}$$

$$M_{magnet} = \rho_{magnet} L_{stk} \tau_m 0.25[(D-2g)^2 - (D - 2g - 2L_m)^2] \tag{2.31}$$

$$C = 80\frac{\$}{kg}M_{magnet} + 10\frac{\$}{kg}M_{cu} + 3\frac{\$}{kg}M_{iron} + penalty \quad function \tag{2.32}$$

2.3.2 Optimization Results

Genetic Algorithm provided in MATLAB Optimization Toolbox is again applied to the constructed cost function. The convergence of the algorithm to the minimum cost is given in Figure 2.13. The variables in design vector yielding the minimum cost are listed in Table 2.9. Magnet length is forced to be an integer due to concerns regarding manufacturability.

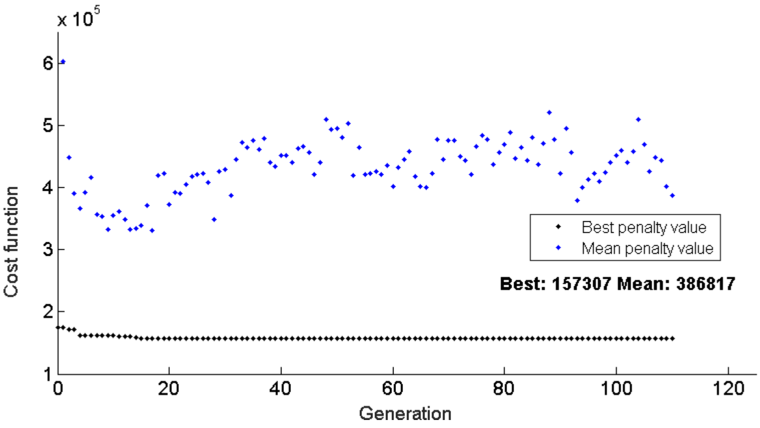

Figure 2.13: Convergence of GA for PMSG design.

Table 2.9: The resulting design vector.

The Design Variable	Optimization Result
Magnet thickness, L_m	13 mm
Number of poles, P	100
Stator slot opening ratio, s_o	0.42
Electrical loading, q	$60,000$ A/mm^2
Armature current density, J	$4.6x10^6$ A/mm^2

3D view and 2D model of the optimum design are given in Figure 2.14 and 2.15, respectively. The unit of the dimensions is millimeters. The main dimensions are listed in Table 2.10 while the design and performance parameters are summarized in Tables 2.11 and 2.12, respectively. Total active material mass is calculated to be nearly 17 tonnes whereas the corresponding cost turns out to be 157 k\$. The magnet cost covers 60% of the total material cost.

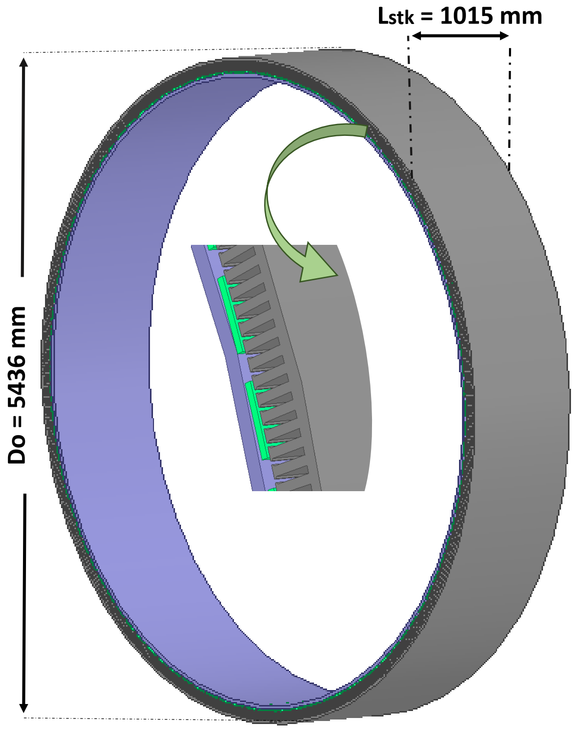

Figure 2.14: 3D view of the optimum PMSG.

Table 2.10: The main dimensions of the resulting design.

Dimension	**Value**
Outer Diameter, D_o	5436 mm
Stacking length, L_{stk}	1015 mm
Air gap length, g	5.5 mm
Tooth width, t_w	15.6 mm
Stator tooth height, h_t	72.8 mm
Inner diameter, D_i	5128 mm

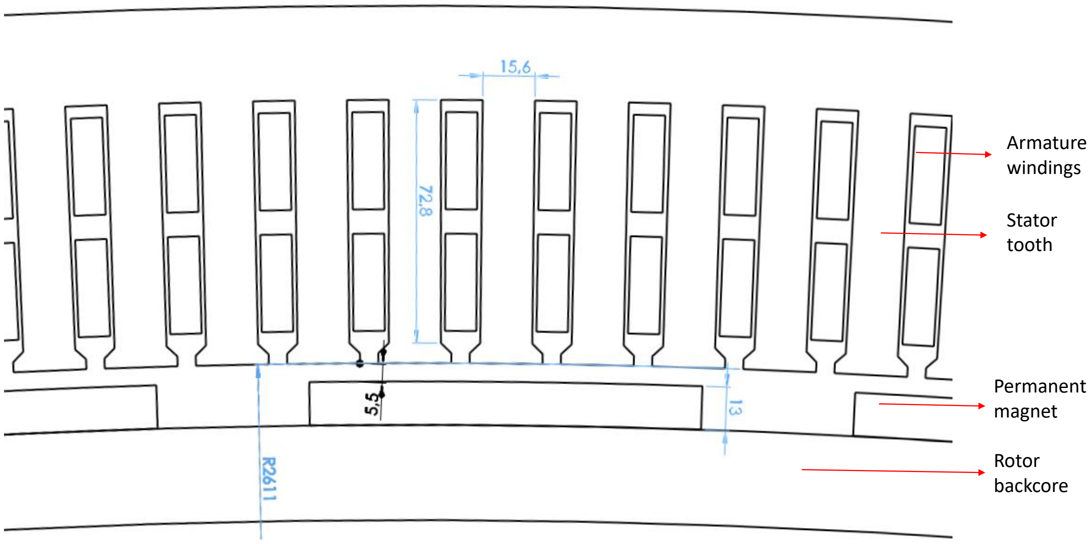

Figure 2.15: 2D model of the optimum PMSG.

Table 2.11: The main parameters of the resulting design.

Parameter	**Value**
Number of conductors per slot, N_a	76
Number of slots, s	600
Phase resistance of armature windings, R_{ph}	8.2 mΩ
Phase inductance, L_{ph}	0.7 mH

The rms of the induced line voltage is calculated to be 658 V which is 4.6% lower than the chosen rated value due to modulation of air-gap flux density in the optimization process.

Table 2.12: The performance parameters of the resulting design.

Parameter	Value
Induced line voltage (rms), E_a	658 V
Power factor, pf	0.9
Core loss, P_{core}	12.3 kW
Armature copper loss, Pcu_a	119.3 kW
Efficiency, η	95%
Magnet mass, M_{magnet}	1.2 t
Iron mass, M_{iron}	13.4 t
Copper mass, M_{cu}	2.3 t
Material mass, M	16.9 t
Material cost, C	157.3 k$

2.3.3 Electromagnetic Finite Element Analysis

The same procedure explained in section 2.2.3 is applied to simulate the findings in ANSYS Maxwell. According to 2D simulation results, the fundamental component of the line to line induced voltage at no load (see Figure 2.16) is 663 Vrms.

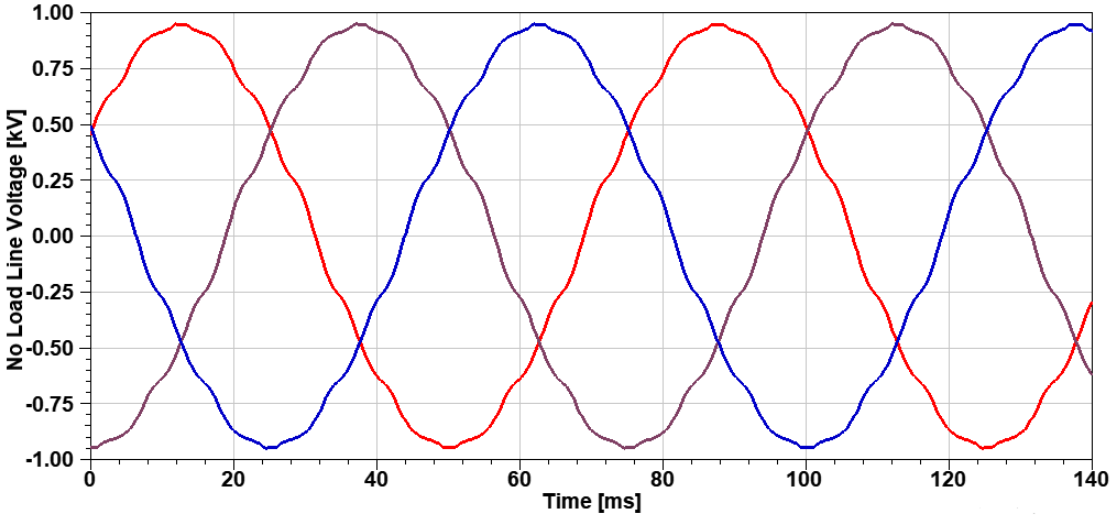

Figure 2.16: No load line to line induced voltage at 16 rpm.

The cogging torque waveforms is given in Figure 2.18. The peak to peak value of the torque ripple is estimated to be 25kN.m which is lower than % 2 of the rated torque. It is important to note that this value is highly dependent on slot opening width, magnet shape and magnet embrace.

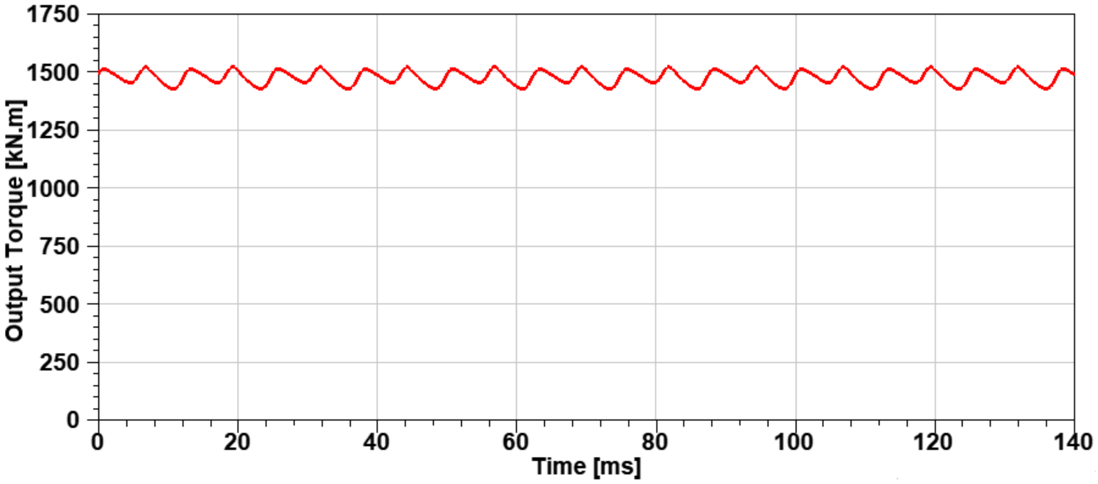

Figure 2.17: Output torque of PMSG under full load.

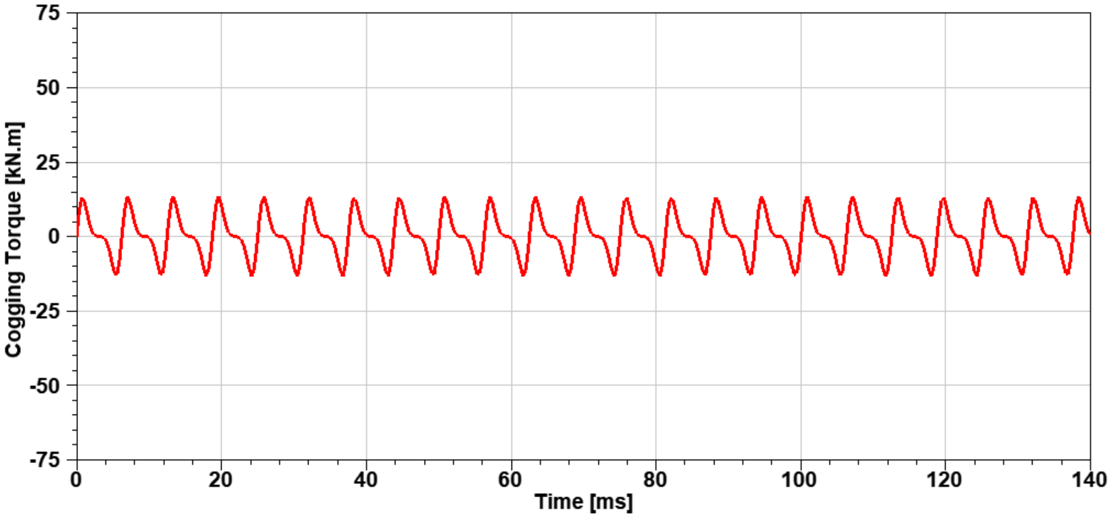

Figure 2.18: Cogging torque at 16 rpm.

Full load condition is analyzed while armature windings are loaded with the rated current. Flux density distribution on a pole under this condition is given in Figure 2.19.

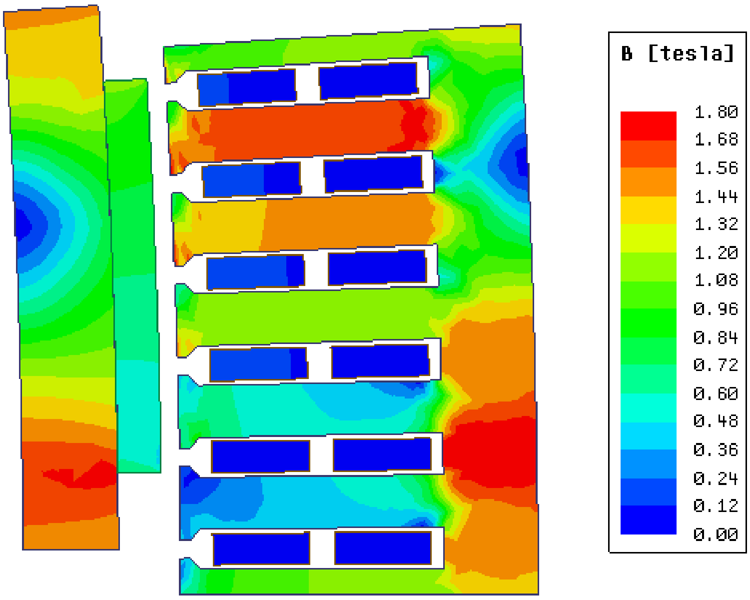

Figure 2.19: Flux density distribution under a pole at full load.

The output power at rated load current can be seen in Figure 2.20. The power oscillates around 2.47 MW with the same frequency as the no load torque ripples.

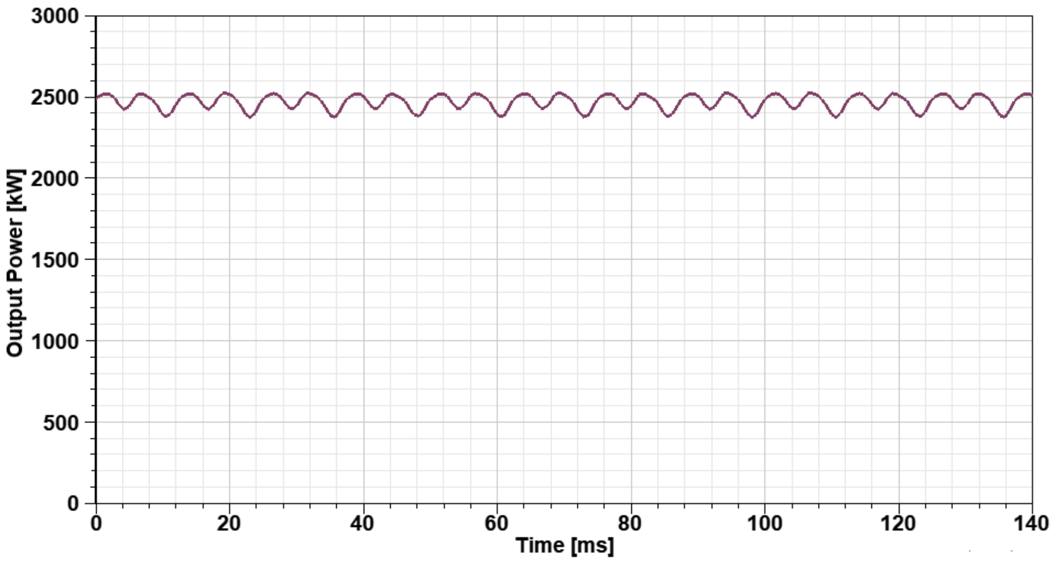

Figure 2.20: Output power under full load.

2.4 Discussion and Comments

Under this chapter, the design procedure of conventional synchronous generators used in wind turbines, namely PMSG and EESG, are reported. The designs are based on material cost optimization and the findings are simulated and verified in ANSYS Maxwell environment.

The designs' purpose is to have reference points for hybrid excited synchronous generators concerning mass, cost and efficiency. The findings are compatible with general expectations since the active mass of PMSG is nearly as much as the half of the EESG mass and the magnet cost dominates the active mass cost of PMSG. However, the structural mass is excluded at this stage of the design and it will be heavier and more expensive for the EESG topology. In this case, total material cost of EESG may turn out to be greater than that of PMSG. The discussion on structural mass will be provided in Chapter 5.

In [32], 3 MW 15 rpm direct drive PMSG with 5 meters of outer diameter is also designed and active material mass is estimated to be 24 tonnes whereas air-gap length and magnet thickness are 5 and 15 millimeters, respectively. In the same study, 3 MW 15 rpm direct drive EESG with 5 meters of outer diameter designed for comparison of wind turbine generators, has an active material mass of 45 tonnes whereas 2.3 MW Enercon-E(82) weights 62 tonnes including structural mass which is generally greater than active mass in direct drive generators.

In a study where direct drive and geared PMSGs are compared, the total weight of 3 MW 16 rpm generator with 5 meters of outer diameter is calculated as 65 tonnes including structural mass [43]. Excluding structural mass and scaling power rating would result in a similar value that is estimated in this thesis. It can be concluded that compared to commercial products and examples in the literature, the parameters of the designs given under this chapter seem realistic. The comparison is summarized in Table 2.13

According to the presented data, the dimension, efficiency and mass values are similar but for PMSGs, the corresponding costs differ as the total cost is highly dependent on the PM cost per kg. The fact that each study assumes a very different specific cost is

Table 2.13: Comparison of designed PMSG, EESG and examples from literature.

Parameter	PMSG	EESG	PMSG and EESG in [32]	PMSG in [43]
Rated power	2.5 MW	2.5 MW	3 MW	3 MW
Rated speed	16 rpm	16 rpm	15 rpm	16 rpm
Outer diameter	5.44 m	5.47 m	5 m	5 m
Axial length	1.01 m	1.05 m	1.2 m	1.4 m
Air gap length	5.5 mm	5.5 mm	5 mm	5 mm
Poles	100	100	160 - 80	-
PM thickness	13 mm	-	15 mm - N/A	12 mm
Efficiency	95%	93%	-	approx. 95%
Active mass	16.9 t	33.1 t	24 t - 45 t	approx. 25 t
Cost	\$ 157.3k	\$ 140.9k	€287k - €162k	approx. €150k

a proof of estimating PM cost not being easy. Therefore, improvement of efficiency, reliability and power density comes with the price of unstable and high costs of PMs.

EESGs are easier to manufacture and active mass material is cheaper; however, the efficiency is inevitably lower due to loss in the field windings. Moreover, the excitation of the field requires additional power supply and control circuit. In spite of these disadvantages of WF excitation, field windings enable flux weakening/strengthening and hence control over induced voltage.

Comparing cogging torque and harmonic contents of induced EMF waveforms will be more complicated since the cost optimization does not prioritize them and resulting optimum design would have dimensions that yield a poor performance regarding torque ripple and harmonic content of EMF. Therefore, as far as the draft designs presented here are concerned, it would be wrong to jump to a conclusion such as cogging torque for PMSG topology is much lower than that of EESG.

In the following chapter, similar design approach will be applied upon hybrid excited topology.

CHAPTER 3

DESIGN OF A HYBRID EXCITED SYNCHRONOUS GENERATOR

3.1 Introduction

In this chapter, the design procedure of a 2.5 MW 16 rpm direct drive hybrid excited synchronous generator is reported by using a similar approach constructed for the design of conventional synchronous generators in the previous chapter. As stated in the section 1.2, the topology proposed in [24] and [25] is selected for design and further discussion. After introducing the topology, the applied design method is given and a discussion about the variation of the dominance of each excitation type for the given topology is carried. Finally, the comments on the topology and the resulting design are shared.

In [24], the authors propose a high voltage hybrid generator connected to a passive rectifier for off-shore wind generation systems with HVDC interconnection and transmission. It is claimed that the system is more efficient, simpler, lighter and cheaper than the existing commercial systems. In [25], the authors have particularly explained the design of a 5 MW 600 rpm two rotor hybrid generator. Moreover, 3 phase and 9 phase stator winding designs are compared and a 3 kW 3000 rpm prototype is constructed for 9 phase system.

Conventional wind turbine generators are connected to the grid via two back to back VSCs which decouple the generator from the grid. The generator side VSC controls the machine speed via vector control whereas grid side VSC controls reactive power and keeps the DC link voltage constant. In the proposed system, two VSCs are replaced with a passive rectifier and the tower transformer is eliminated so that the DC output of the rectifier is sent to the offshore substation where it is converted to AC and sent to HVDC converter station as seen in Figure 3.1.

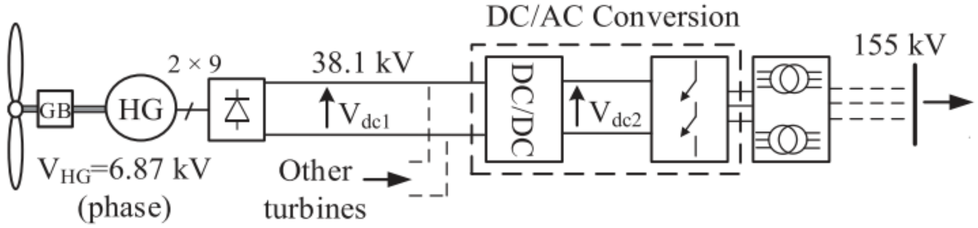

Figure 3.1: Connection of the proposed hybrid generator system to the converter station [25].

The hybrid generator (HG) proposed in [25] utilizing both PM and WF rotor sections has 9 phase stator windings with 6.87 kV rms phase voltage at 600 rpm. The HG combines the output voltage due to a fixed field from PM and a controlled variable voltage due to the variable field of DC windings. The range of the total voltage variation depends on the ratio of the WF excitation over PM field excitation. Therefore, the term split ratio is defined as the ratio of the field excitations and taken as 3:1 (0.75/0.25) to be able to cover for 25% terminal voltage variation between individual wind turbines whose outputs are to be connected in parallel.

DC current for the WF rotor excitation is provided by a brushless exciter with AC multiphase rotor winding. Output of the brushless excited rotor is connected to a rotating rectifier that supplies DC to the WF. The brushless exciter has a DC stator winding fed by the rectified output of the HG.

Considering the provided main information about the wound field and PM excited hybrid generator topology; in the following sections of this chapter, the design of such generator is reported.

3.2 Design Procedure

The mechanical power of the rotating electrical machines can be related to the air gap diameter, D and axial length, L of the generator using Eq. (3.1) given below;

$$P_{mech} = \frac{\pi^2}{4\sqrt{2}} \omega k_w B_{avg} D^2 L \tag{3.1}$$

Where, k_w is winding factor, ω is the rotational speed in rad/s, B_{avg} and q are average air gap flux density and electric loading, respectively. Therefore, it can be concluded that the torque and hence the mechanical power is directly proportional to the active axial length. In the previous chapter, the given main relation was used to determine the main dimensions of separate WF and PM based generators. For the hybrid generator topology under investigation, it is known that the total power of the generator is a result of both WF and PM excitations where related power and induced voltages are directly related to the axial length of corresponding rotor sections.

In order to make a fair comparison between full PMSG and EESG designs given in Chapter 2 and the hybrid excited generator, it is decided to scale the full PMSG dimensions whose parameters are reported in Table 2.10 according to the chosen excitation split ratio. Therefore, the axial length of the PM rotor section is calculated by multiplying the length of full PMSG with the chosen excitation ratio whereas the dimensions of the WF rotor is calculated by constructing a new objective function to be optimized by imposing the parameters of the stator of the full PMSG design. Since the stator is common for both rotor sections, the stator length corresponds the the summation of the lengths of each section and the required gap between the rotor sections. The resulting cross-sectional view of the explained approach is illustrated in Figure 3.2.

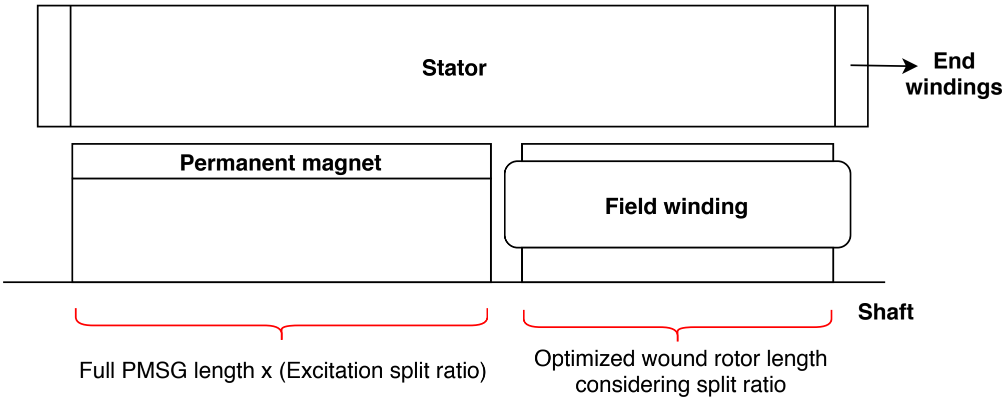

Figure 3.2: Cross-sectional view of the topology.

Construction of the objective function to optimize the dimensions of the WF rotor is given in Figure 3.3. The number of poles, stator dimensions and air gap length are fixed as the values of the full PMSG are imposed to the design. The excitation split ratio is chosen and fed to the analytical model. MMF, field winding current density, and the rotor slot opening ratio are chosen as design variables and hence the input of the objective function. The optimization is again based on minimizing the material cost and a penalty function is calculated according to the specified criteria and added up the cost value.

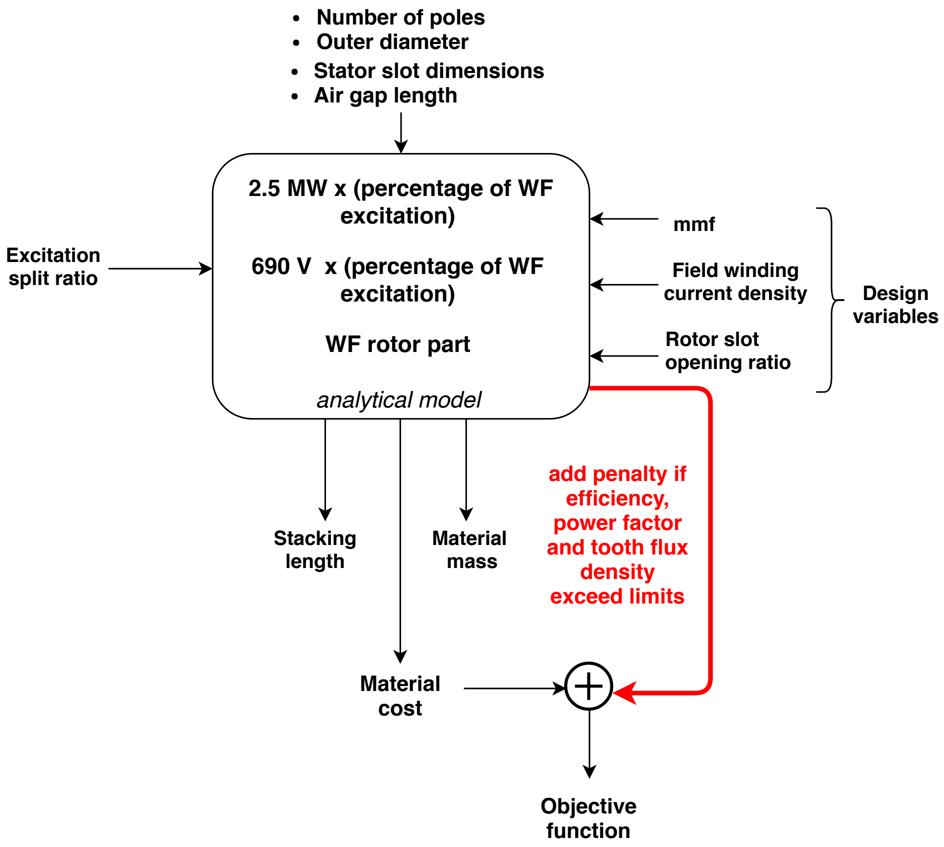

Figure 3.3: Construction of the objective function for the design WF rotor of the hybrid excited generator.

Therefore, once the excitation ratio is chosen, the main dimensions and parameters of the hybrid excited generator are obtained through explained procedure.

3.3 Variation of the Excitation Split Ratio

As defined earlier, the ratio of PM and WF excitations gives the split ratio of the hybrid generator. For instance, the ratio 4:1 corresponds to the case where 80% of the induced voltage is obtained from PM excitation while the remaining 20% is due to the WF excitation. In this case, that 80% resulting from PM excitation would be fixed and uncontrollable whereas changing the field excitation of the wound rotor part would change the resulting induced voltage at the armature windings. Therefore, the split ratio, determining the control range over induced voltage and hence the generated power, is a key parameter for the hybrid excited generator design.

The control range over the induced voltage depends on the requirements of the application. For wind turbine applications, these requirements may be determined by the variation of the wind speed for individual turbines whose terminals are to be connected in parallel. In that case, the control range needs to be wide enough to compensate for the induced voltage variation of each individual. It is said that wind velocity variation is recorded under 20% between individual wind turbines located in the same wind farm [44–46].

The variation of excitation ratio also effects the material mass, cost and performance parameters since it directly involves in the determination of the axial length of each section. Hence it is decided to investigate the effect of split ratio on the generator parameters before fixing it for the final design.

In this thesis, optimization technique applied so far was Genetic Algorithm aiming at minimizing the material cost. However, investigating the effect of split ratio through a single objective optimization would be pointless since the algorithm would converge to a design where the split ratio is adjusted to minimize just the chosen objective function provided that the limits specified for performance parameters are once reached. For example, if the active material cost is chosen to be the objective function, the algorithm tends to maximize the WF excitation whereas if the active material mass is chosen instead, the algorithm converges to maximize PM excitation to yield a power dense design. Therefore, the investigation is carried using multi-objective function where the generator losses, active material mass and cost are minimized all together.

Multi objective optimization problems have no unique solution; rather there exists a set of reasonable trade-off optimal solutions. This set is known as Pareto front [47]. In our case, generating the Pareto front allows us to discuss the trade-off among the chosen parameters of the design; namely the efficiency, active material mass and corresponding cost.

For this purpose, analytical model of the hybrid excited generator is constructed on MATLAB environment where the percentage of PM excitation, MMF due to field windings, field current density and rotor slot opening ratio are selected as the variables. Obtained Pareto front of the objective functions while the percentage of PM excitation is varied between 45% and 95% is given in Figure 3.4.

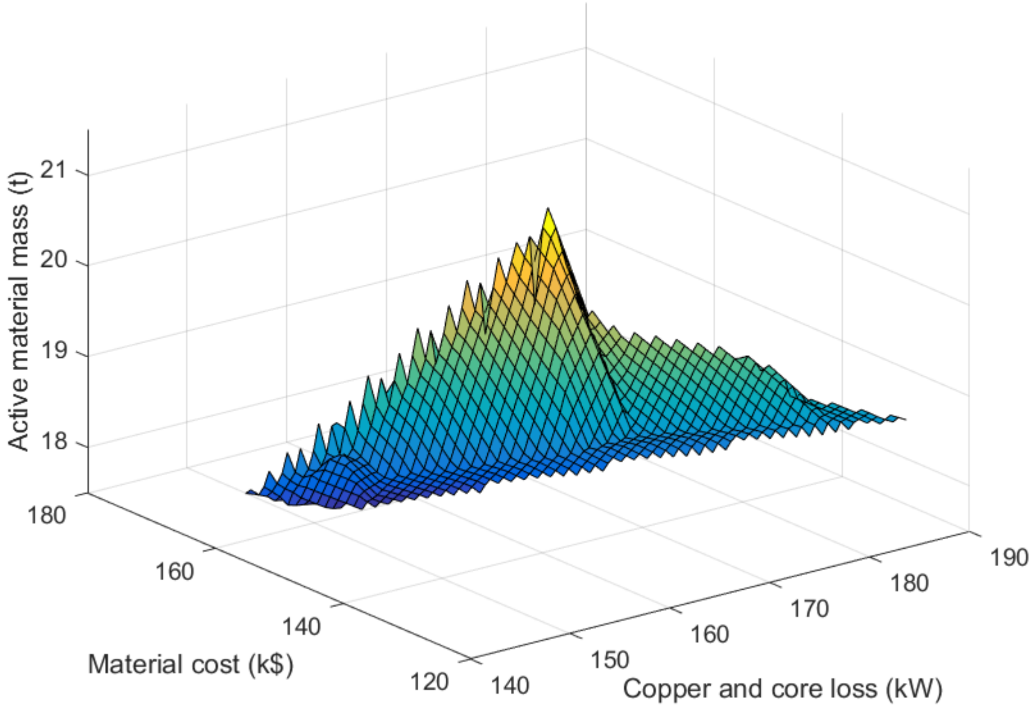

Figure 3.4: 3D Pareto front of the multi-objective optimization problem.

To compare the performance of the designs provided by the Pareto front, the acquired solution set is analyzed. Each design vector belonging to an element in the solution set is given as an input to the function where the parameters of hybrid excited generator are calculated. The resulting variations are plotted as given in Figure 3.5.

It can be concluded that efficiency is tend to increase as the percentage of PM excitation increase. Nonetheless, the active material mass decreases with increasing split ratio since the PM part is expected to have higher power density. However, due to increasing magnet requirement, increasing PM excitation percentage results in higher material cost. Power factor also increases in a small range while the split ratio gets higher. Since in PM machines, phase inductance is calculated by taking into account the reluctance of PM in addition to the air gap reluctance, the power factor increases as the PM part grows dominant.

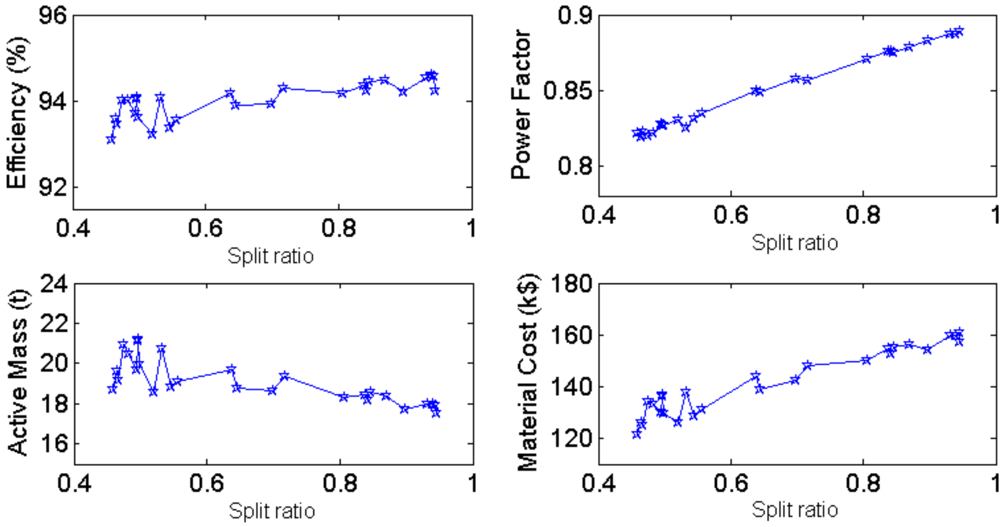

Figure 3.5: Variation of the generator parameters with respect to split ratio according to recorded Pareto set.

This discussion on analysis reveals that the choice of split ratio depends on performance requirements. By setting the design criteria, Genetic Algorithm based multi-objective optimization is carried to find out a single point that the algorithm converges. Minimum power factor is set to 0.85 while the minimum efficiency is selected as 94%. Power factor and efficiency requirements are imposed to the objective function by means of penalty whereas the loss, active material mass and cost values are normalized using the ranges calculated the score histogram while generating the Pareto front. The multi-objective function with the imposed criteria converged to a solution where the excitation split ratio is recorded as 0.65. The corresponding design vector and boundaries are given in Table 3.1.

Table 3.1: The resulting design vector of multi-objective optimization.

The Design Variable	**Optimization Result**
Split ratio	0.65
MMF	4772 A
Rotor slot opening ratio, s_{or}	0.50
Field current density, J_r	$3.557x10^6$ A/mm^2

It is important to note that the convergence depends on the selected efficiency and power factor criteria. The 0.65 split ratio corresponds to a design with 94% efficiency and a power factor 0.85. Moreover, it means that 65% of the induced voltage and generated power will be fixed due to PM excitation whereas remaining 35% will be controllable due to field winding excitation. However, 35% controllability range is beyond the estimated requirement. Therefore, in this study, the excitation split ratio is decided to be selected as 0.75 since 25% voltage variation is sufficient and efficiency would be slightly higher than the estimated value for a ratio of 0.65. Following part of the thesis focus on the design with 75% PM and 25% WF excitation.

3.4 Dimensions and Parameters of the Selected Design

After selecting the split ratio, the principle given in Figure 3.3 is applied to estimate the WF rotor parameters. The PM part is scaled down for the decided split ratio and the parameters are recalculated. The obtained results for separate excitation sections are given in Table 3.2 and 3.3.

As stated in Section 3.2, the stator of the 2.5 MW PMSG designed in Chapter 2 is imposed to the design. Therefore, only the length of the stator is modified such that it is equal to the summation of the length of WF rotor, PM rotor and the gap in between due to end windings of field. Moreover, there should be also a gap between the end windings and the PM rotor. The length of this gap is empirically chosen to be near 5 millimeters. The side view of the both rotor sections and the stator can be seen in Figure 3.6.

Table 3.2: The main parameters of the excitation sections and the whole machine.

Parameter	**PM section**	**WF section**	**Whole machine**
Rated power, P_{out}	1875 kW	625 kW	2500 kW
Rated terminal voltage, V_t	517.5 V	172.5 V	690 V
Induced line voltage, E_a	490 V	160 V	650 V
Outer diameter, D_o	5436 mm	5436 mm	5436 mm
Stacking length, L_{stk}	761 mm	220 mm	1020 mm
Air gap length, g	5.5 mm	5.5 mm	5.5 mm
Number of poles, p	100	100	100
Core loss, P_{core}	9.2 kW	3.1 kW	12.3 kW
Armature copper loss, Pcu_a	89.8 kW	41.2 kW	117.9 kW
Field copper loss, Pcu_f	-	25.1 kW	25.1 kW
Efficiency, η	94.9%	90%	94.1%
Iron mass, M_{iron}	10.1 t	4.2 t	14.7 t
Magnet mass, M_{magnet}	879 kg	-	879 kg
Copper mass, M_{cu}	1.8 t	2 t	3.5 t
Material mass, M	12.8 t	6.2 t	19.2 t
Material cost, C	\$118.9k	\$32.8k	\$150k

While designing each rotor section, the copper losses are calculated separately and hence the numbers indicated in Table 3.2 include losses due to end windings as if there are two separate stators. Therefore, armature copper loss for whole machine is slightly less than the summation of separately calculated losses.

Table 3.3: Some of the parameters of the resulting design.

Parameter	PM part	WF part	Whole machine
Number of turns per slot, N_a	76	76	76
Inner diameter, D_i	5128 mm	4995 mm	4995 mm
Rotor tooth height, h_{tr}	-	46.7 mm	46.7 mm
Width of pole shoe, W_{ps}	-	118 mm	118 mm
Number of turns in field, N_f	-	83	83
Magnet/pole shoe embrace	0.72	0.72	0.72
PM thickness, L_m	$13mm$	-	13 mm

The efficiency of WF part is lower than EESG designed in Chapter 2 since for such power rating, the ratio of bore diameter over length is far from the optimum point. Moreover, the rated current is 2250 A which apparently causes lower efficiency when the WF part is treated as a separate machine.

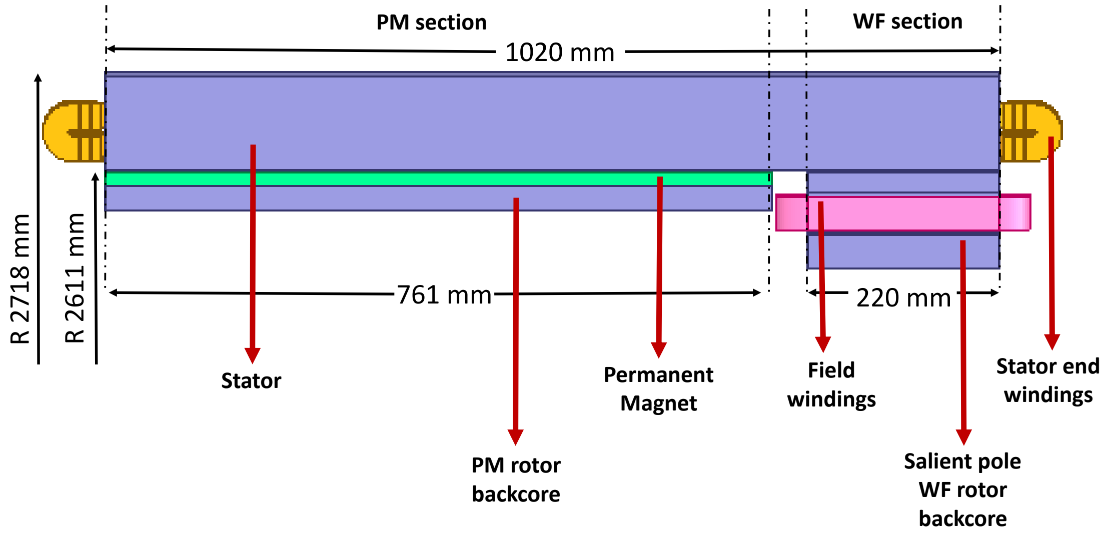

Figure 3.6: Axial view of the generator sections.

The active material mass of the whole machine is estimated to be 19.2 tonnes and the corresponding cost is 150 k$ whose 46.8% belongs to the permanent magnet cost.

3.5 Discussion and Comments

In this chapter, the main approach applied to permanent magnet and electrically excited synchronous machines is used to design a hybrid excited synchronous generator consisting of two separate rotor sections sharing a stator. Variance of the percentages of applied excitation is discussed and it is decided to fix the design with 75% PM excitation and 25% WF excitation. It means that 75% of the induced voltage and generated power will be fixed due to PM excitation. The remaining 25% will be added up when the rated field current is applied.

The discussed configuration can be treated like two separate generators connected in series as seen in Figure 3.7. The excitation sections share a common stator and therefore the armature current is also shared.

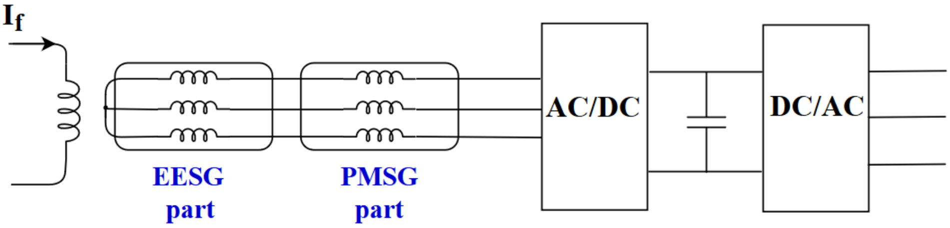

Figure 3.7: Grid connection scheme in case of series connection of the excitation sections.

Since the WF excitation enables control over terminal voltage in a certain range, there is an option to utilize passive converter in the rectification stage. Using diode instead of MOSFET/IGBT in the rectifier would significantly decrease the converter cost. However, the machine side converter is generally responsible from speed control and passive converter would not achieve this duty. In this case, the speed control would only rely on pitch control whose response time is restricted by mechanical time constants. Therefore, there is a trade-off between controllability and cost when the rectification stage is concerned.

The excitation sections may also be connected in parallel provided that their terminal voltages are equal as seen in Figure 3.8. Therefore, the stator and armature windings cannot be shared as in the series connection case. However, rectification stage can be decoupled and therefore generator side converter of the PMSG part can be an active rectifier whereas the one connected to the EESG part can be a passive rectifier.

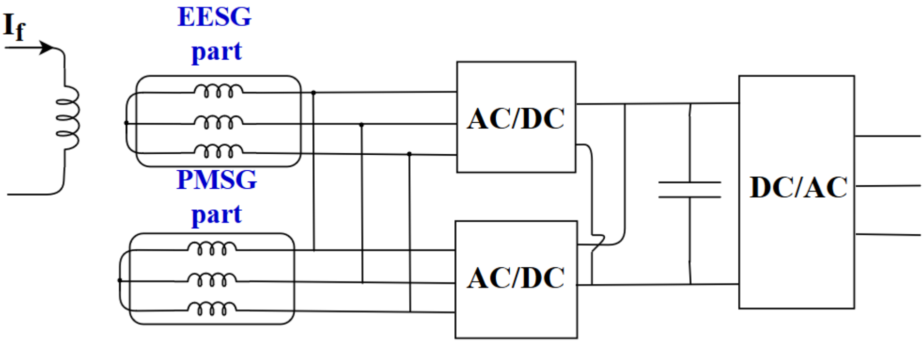

Figure 3.8: Grid connection scheme in case of parallel connection of the excitation sections.

Another option is to fully decouple the EESG and PMSG part by also utilizing separate inverters as seen in Figure 3.9. In this case, the DC link voltages may also be controlled independently and the excitation sections would be fully decoupled. Nonetheless, this configuration increases the converter cost.

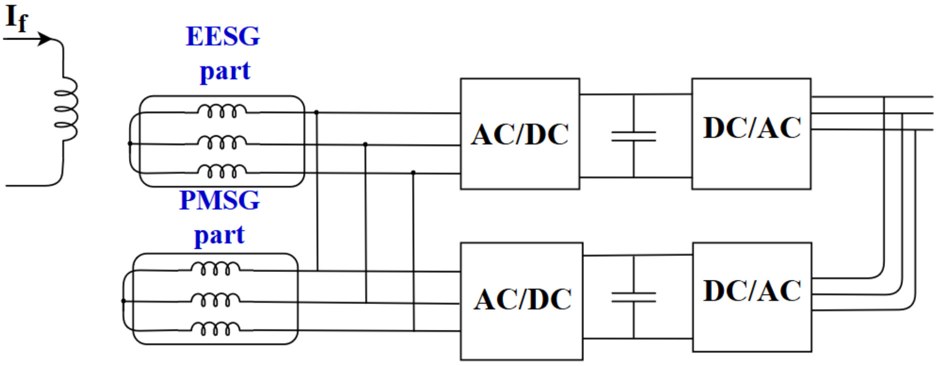

Figure 3.9: Grid connection scheme for fully decoupled case.

The discussion in this thesis is based on series connection of the excitation parts since a comparison between direct drive synchronous generator contained in a single body and similar main dimensions is concerned.

The results obtained under this chapter are as expected since the parameters lay in between those of fully EESG and fully PMSG designed in Chapter 2. There are certain trade-offs between cost, mass and efficiency; and the application requirements determines the priority of each. In the next chapter, the designed hybrid excited generator is verified and analyzed in ANSYS Maxwell environment.

CHAPTER 4

FINITE ELEMENT ANALYSIS OF THE DESIGNED HYBRID EXCITED SYNCHRONOUS GENERATOR

4.1 Introduction

In this chapter, the hybrid excited synchronous generator is modeled in ANSYS Maxwell FEA software. It is aimed to verify and analyze the design by using 2D and 3D FEM simulations.

In the analytical design process, two rotor sections, namely PM and WF rotors are treated as if they are part of two separate machines. Since the flux path is in radial direction for both sections, this approach is theoretically feasible. However, interaction of the end windings of the WF rotor and the PM is neglected in the design process. This assumption and its consequences are needed to be discussed by analyzing the whole machine. Therefore, the magnetic field in the interaction region is analyzed.

Firstly, 2D models of the rotor sections are simulated separately. Afterwards, the whole machine model is constructed in Maxwell 3D module. Figure 4.1 shows 5 poles of the HESG model to be simulated. The simulation and analysis results are shared in the following parts of this chapter.

4.2 2D Analysis

The hybrid excited machine sections whose dimensions are given in Table 3.2 are parametrically modeled in RMxprt module and imported as Maxwell 2D designs. The simulation results using 2D transient solution type are reported under this section.

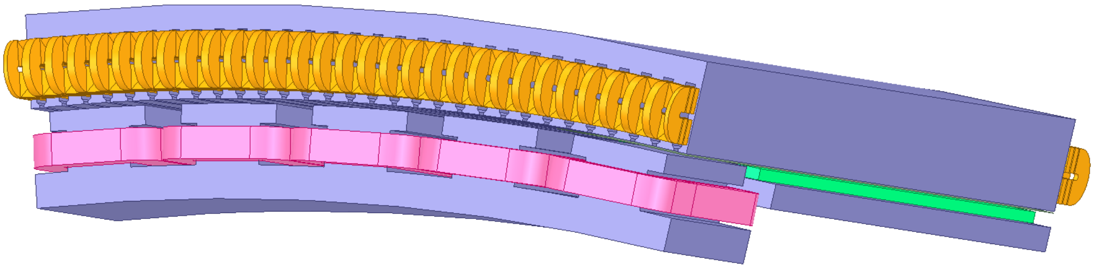

Figure 4.1: 3D view of 5 poles of the HESG.

4.2.1 Permanent Magnet Rotor Section

The PM rotor section is responsible from 75% of the induced voltage and output power. The induced voltage due to PM part under no load condition is given in Figure 4.2. The rms value of the fundamental component is measured as 496 V which is nearly 96% of the rated terminal voltage of the PM section.

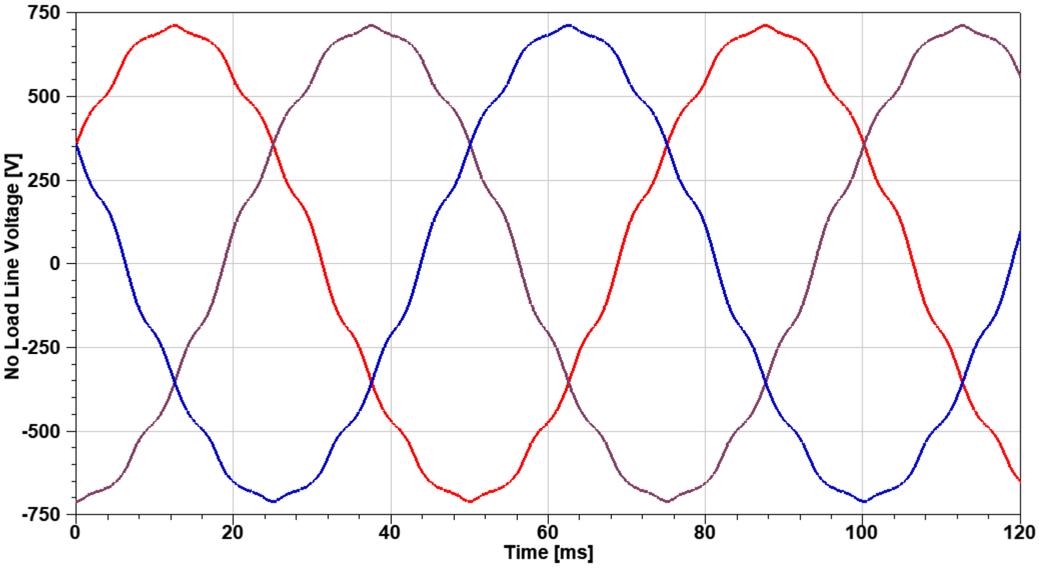

Figure 4.2: No load line to line voltage at 16 rpm of the PM section.

The output power under full load condition is given in Figure 4.3. The average of the given waveform is measured to be 1840 kW. The observed ripple in the power is due to the variation in the torque waveform whereas no load torque ripple, namely the cogging torque of PM section is given in Figure 4.4, peak to peak value of which is 18 kNm. This is below 2% of the rated torque of the PM rotor section.

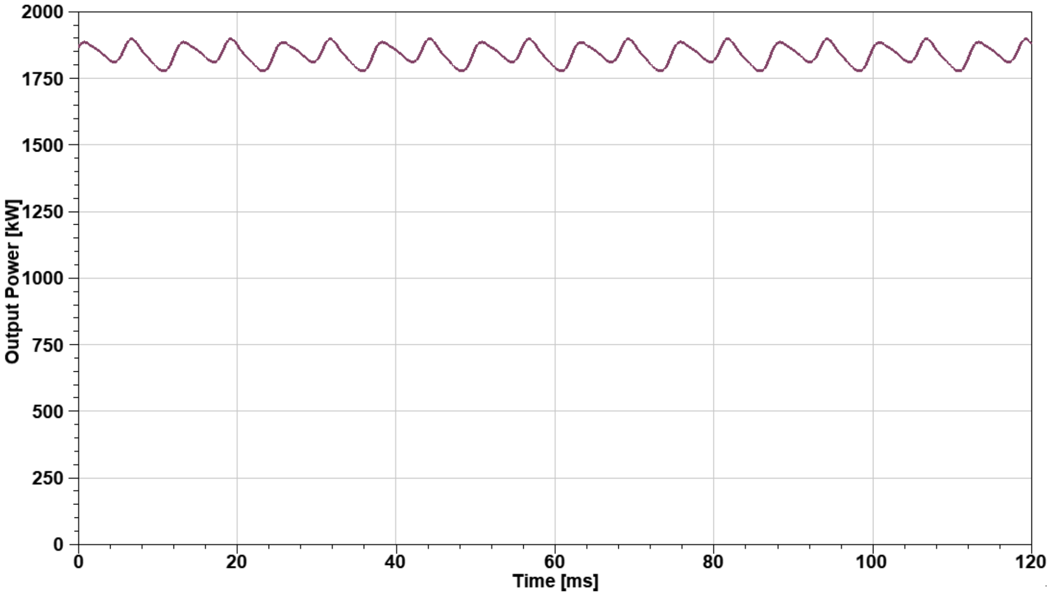

Figure 4.3: Output power of PM part under full load.

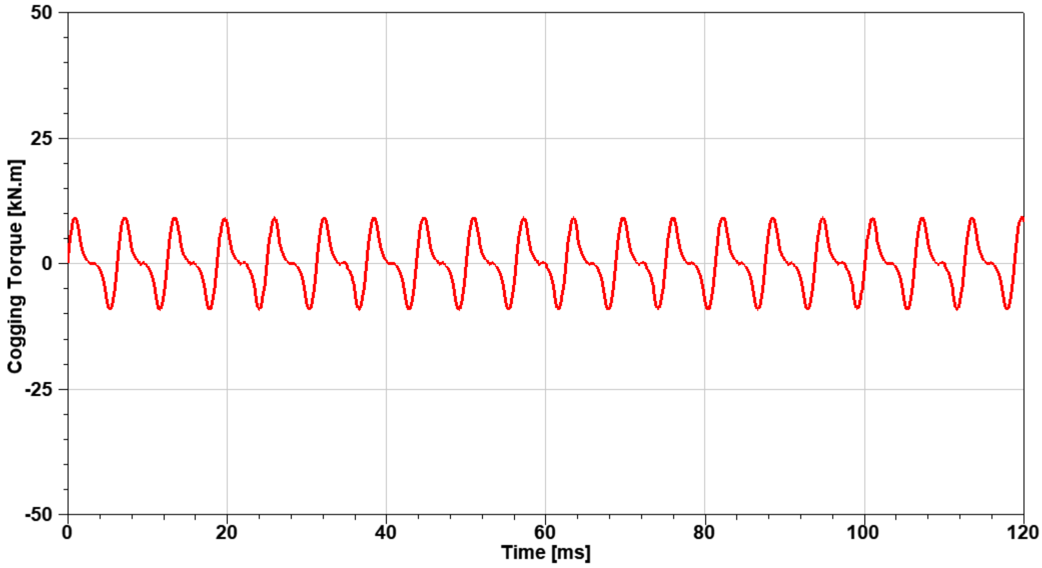

Figure 4.4: No load torque ripple of PM part.

The flux density distribution while the rated armature current is applied is given in Figure 4.5. The flux densities in the teeth and back core remain within the desired limits.

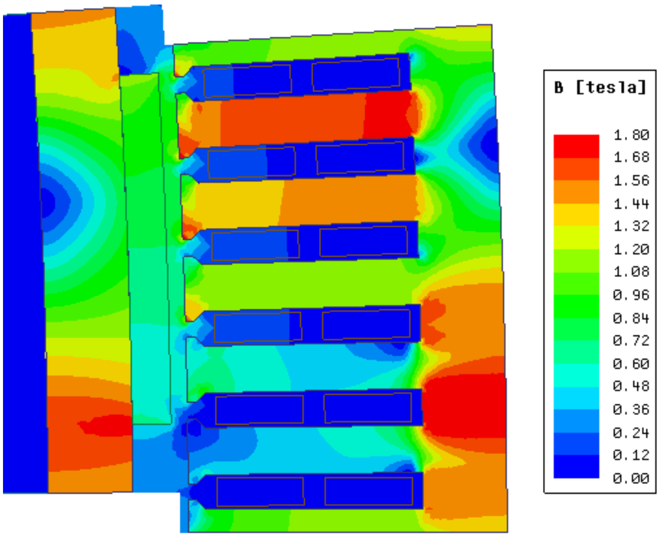

Figure 4.5: Flux density distribution of PM part at full load condition.

4.2.2 Wound Field Rotor Section

The WF rotor section is capable of generating 25% of the rated power of whole machine when the rated field current is applied. The no load induced voltage is given in Figure 4.6 whose fundamental component has an rms value of 162 V.

Output power under full load at rated field current is given in Figure 4.7 whose average value is 544 kW. This is the 87% of the rated power of this section. However, if the WF rotor section is treated like an individual EESG, it would have an efficiency of 89% which is lower than those of PM part itself and whole machine. Therefore, the output power being lower than the rated is acceptable.

No load torque ripple is given in Figure 4.8. The peak to peak value is measured to be 12.8 kNm where the rated torque of the WF section with given field current is nearly 375 kNm. Therefore, simulated no load torque ripple is slightly above 3% of the rated torque of WF section.

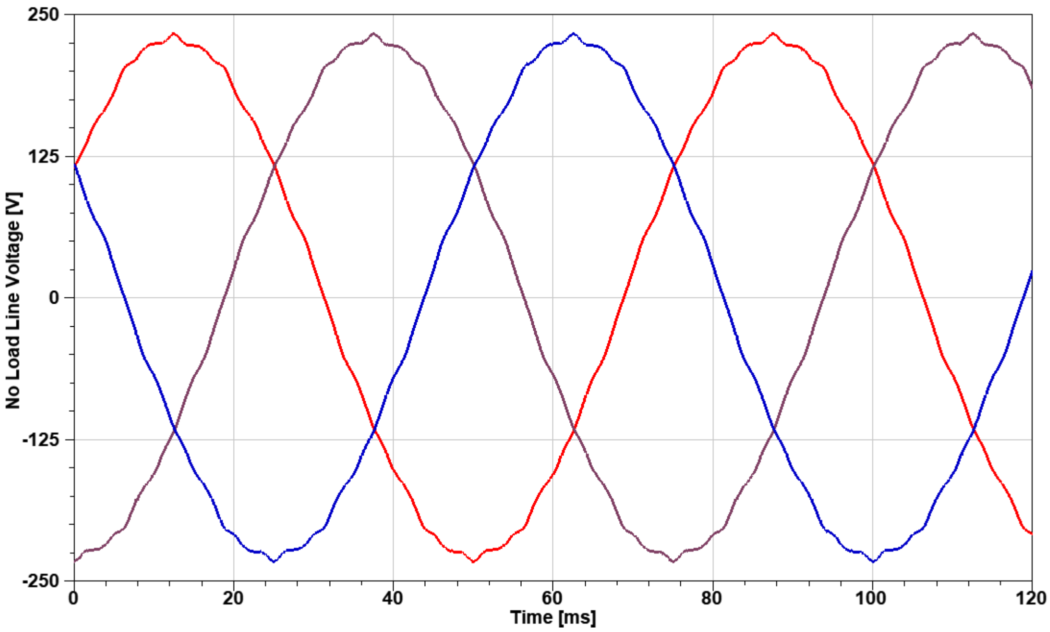

Figure 4.6: No load line to line voltage at 16 rpm of the WF section.

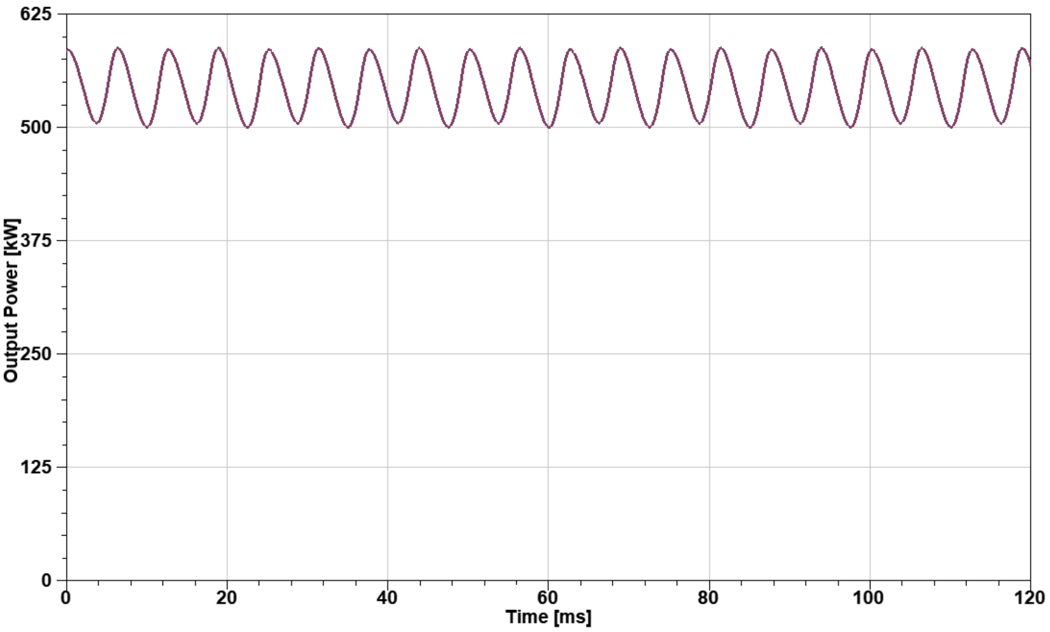

Figure 4.7: Output power of WF part under full load.

Flux density distribution under full load condition is given in Figure 4.9. The maximum density is observed in the teeth neighboring to the excited phase windings and may reach up to 2 Tesla.

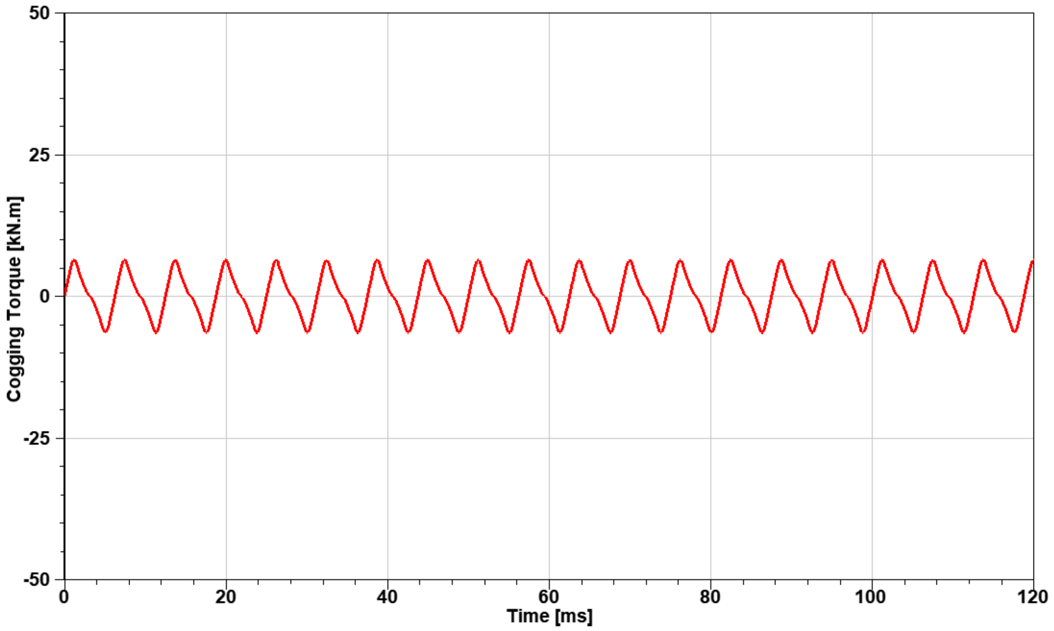

Figure 4.8: No load torque ripple of WF part.

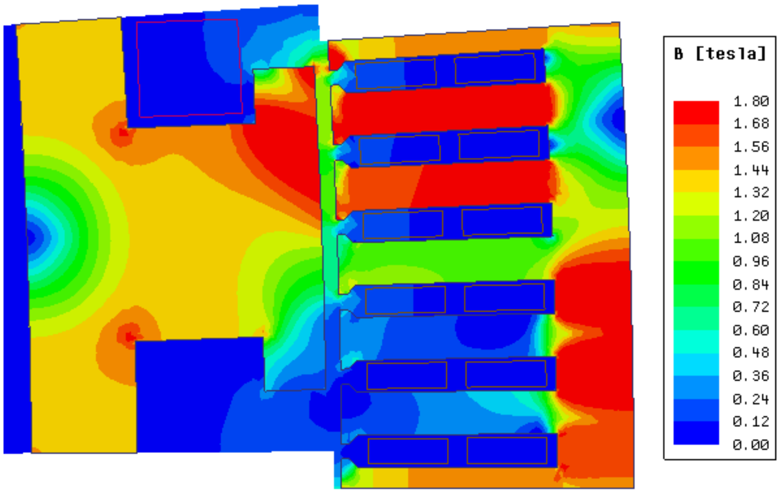

Figure 4.9: Flux density distribution of WF part at full load condition.

4.2.3 Variation of the Field Current

The simulations presented in the previous section are conducted for the rated field current which is determined to be 55A. Since capability of controlling terminal voltage and output power is stated as one of the most important advantages of this topology, the range of this controllability needs to be investigated by varying the field current.

This controllability is highly dependent on the response time of the field current to the control signal. Since the equivalent inductance of the field windings of 100 poles connected in series is estimated to be in the order of Henries, the time constant is relatively high. In Figure 4.10, the decay of field current is given. The time constant is calculated to be nearly 0.5 seconds where the equivalent inductance and resistance of the field windings are 3.8 H and 7 Ω, respectively.

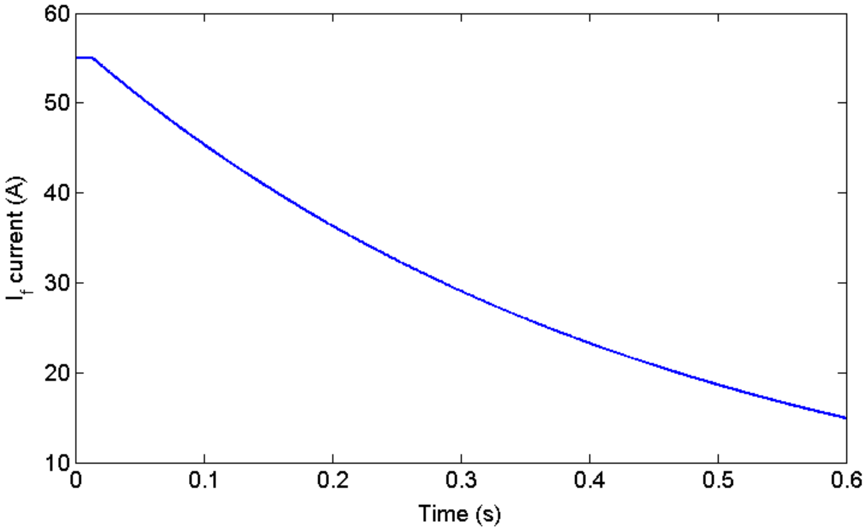

Figure 4.10: The decay of the field current.

The summation of induced voltages from both sections for different field currents are given in Figure 4.11. When the rated field current is applied, total induced line voltage is recorded to have an rms value of 660 V. The variation of no load terminal voltage with respect to the field current is given in Figure 4.12. Increasing the field current from 10A to 55A increases the terminal voltage by 24.5%.

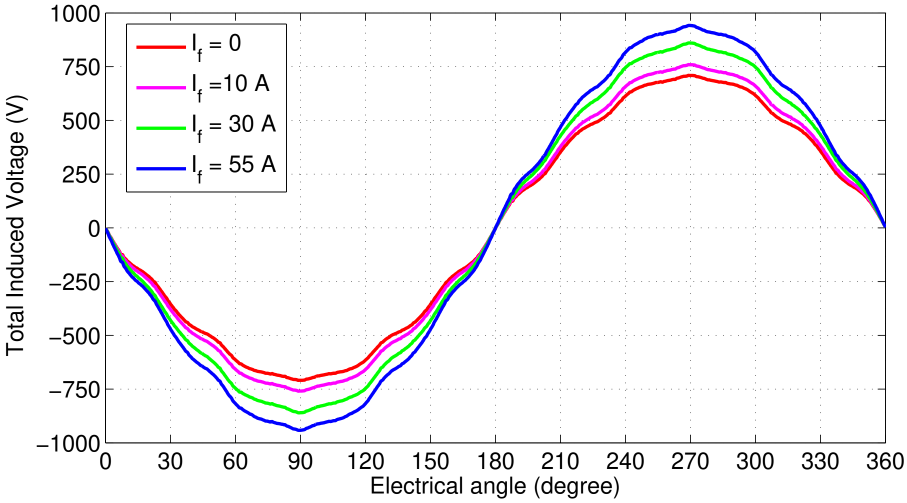

Figure 4.11: Total induced voltage for different field currents.

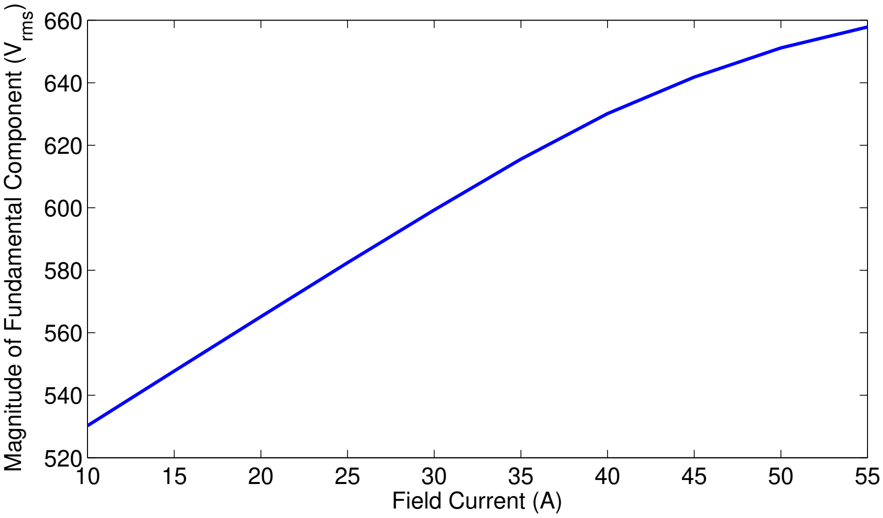

Figure 4.12: Variation of total induced voltage with respect to field current.

The summation of output power of the sections at full load according to Maxwell 2D simulations for different field currents are given in Figure 4.13. At rated field current, output power is found to be nearly 2.4 MW.

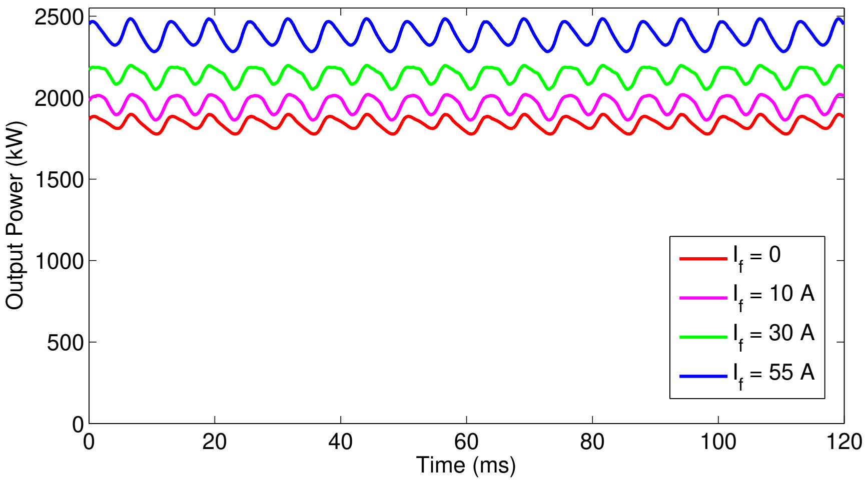

Figure 4.13: Variation of total output power with respect to field current.

Changing the applied field current also affects the power factor as can be seen from the typical V curve characteristics of synchronous machines given in Figure 4.14. Increasing the field current increases the power factor for the leading case and decreases it for the lagging case.

In this thesis, it is assumed that the designed generators are driven under vector control and the angle between phase current and induced voltage is equal to zero to maximize the available torque at the output. The vector diagram of the corresponding case is given in Figure 4.15. The phase current and induced voltage being in phase enforces the power factor to be leading. Therefore, the power factor is expected to increase as field current is increased.

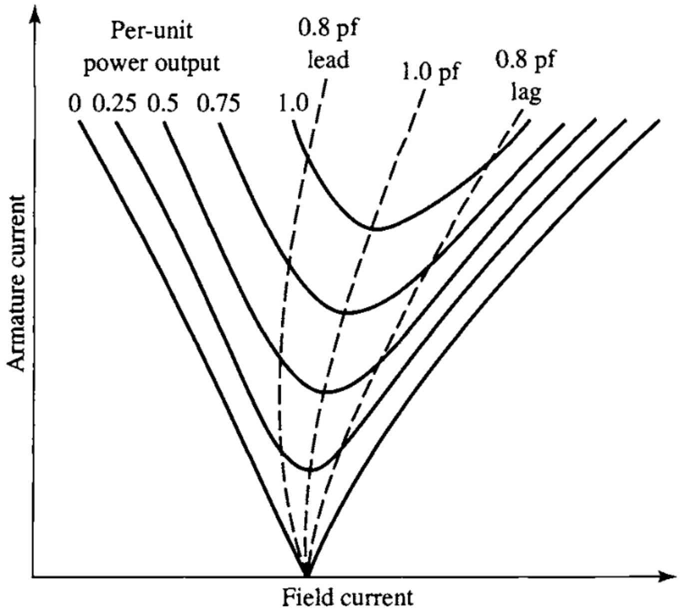

Figure 4.14: Typical V-curves of synchronous generators [48].

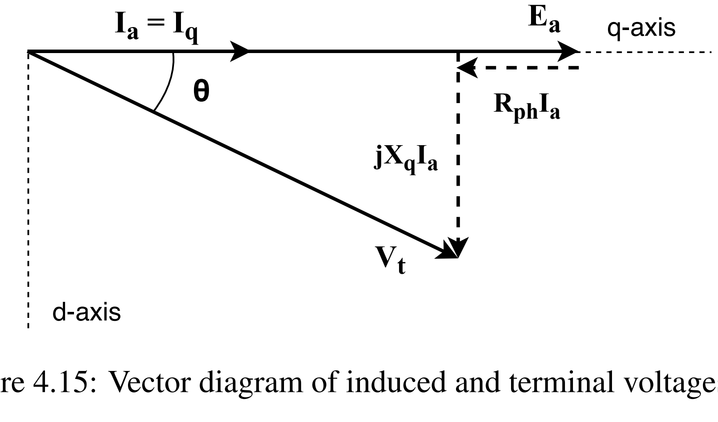

Figure 4.15: Vector diagram of induced and terminal voltages.

For the designed HESG, the variation of power factor, which is a result of changing terminal voltage, can be seen from Figure 4.16. The power factor increases from 0.8 to 0.86 as the field current goes up from 10 A to 55 A.

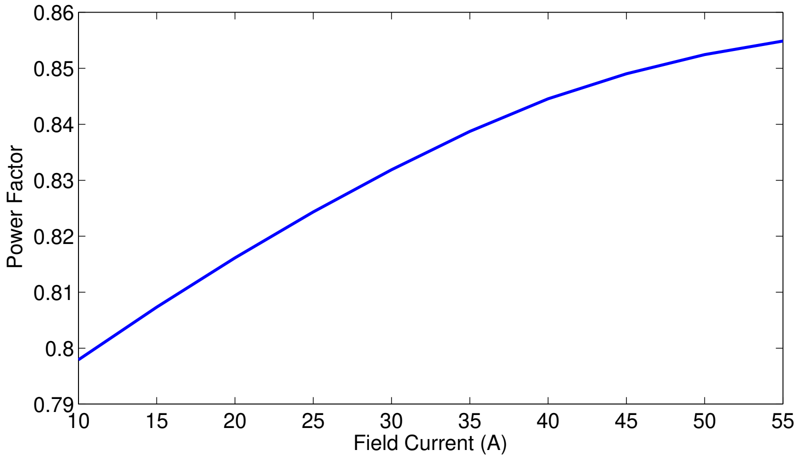

Figure 4.16: Variation of power factor with respect to field current.

According to the results of 2D simulations, varying the field current yields the expected variation in the induced voltage and output power.

Another important feature of the hybrid topology is the flexibility to operate at different modes according to the load demand. At full load, 75% of the output power is inevitably generated by the PM section; however, it is possible to determine how much power is generated by the WF section at partial loads. At light loads, the WF section may not be energized at all to maximize the generator efficiency. That is due to the fact that copper losses in the field windings is more dominant in lower power ratings. In Figure 4.17, the change in efficiency with respect to the percentage of load for different modes of operation is presented. As seen from the graph, below 30% rated power, operating only the PM section is the most efficient mode whereas under higher power outputs, varying the field current in hybrid excitation mode yields the highest efficiency. Since in PM mode, 75% power output is obtained with the rated armature current, the efficiency reduces due to loss in the armature windings. Operating with rated field current all the time in the hybrid mode, dramatically reduces the efficiency under light loads due to the dominance of the loss in field windings at low power ratings.

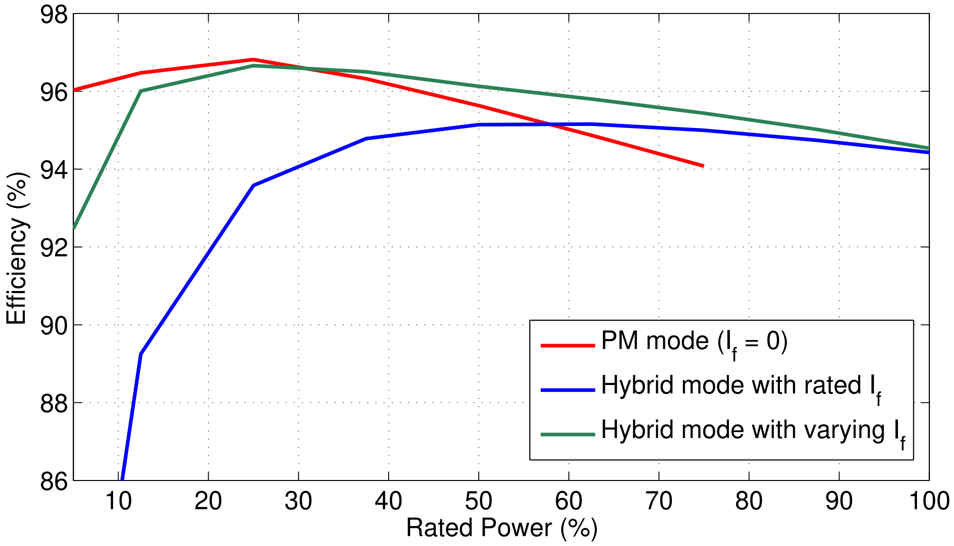

Figure 4.17: Efficiency vs. load for different operating modes.

In hybrid mode with varying field current, the current is gradually increased from 0 to 55 A where 50% load case corresponded to a field current of 30 A which is slightly higher than the 50% of the rated value. In Table 4.1, calculated efficiency values for different loads are listed.

According to the results, controlling the load of operation under different loads improves efficiency and annual energy production of the wind turbine.

Table 4.1: Efficiency with respect to load.

	Efficiency		
Load	**Only PM Mode**	**Hybrid Mode (Constant If**	**Hybrid Mode (Varying If)**
12.5%	96.4%	89.2%	96%
25%	96.8%	93.3%	96.6%
37.5%	96.3%	94.8%	96.5%
50%	95.6%	95.1%	96.1%
62.5%	94.8%	95.2%	95.8%
75%	94%	94.9%	95.4%
100%	-	94.4%	94.4%

4.3 3D Finite Element Analysis

So far, the hybrid excited synchronous generator under investigation is analyzed like two separate PM and WF excited machines connected in series. The working principle is indeed so, however the assumption still needs to be verified by analyzing the generator as a whole. Hence, 3D simulations are conducted to discuss the performance of the whole model.

4.3.1 Magneto-static Solution Type

3D FEM simulation of the designed machine geometry requires excessive number of mesh elements. Mesh operation of a single pole of the generator plotted for magneto-static solution type can be seen in Figure 4.18.

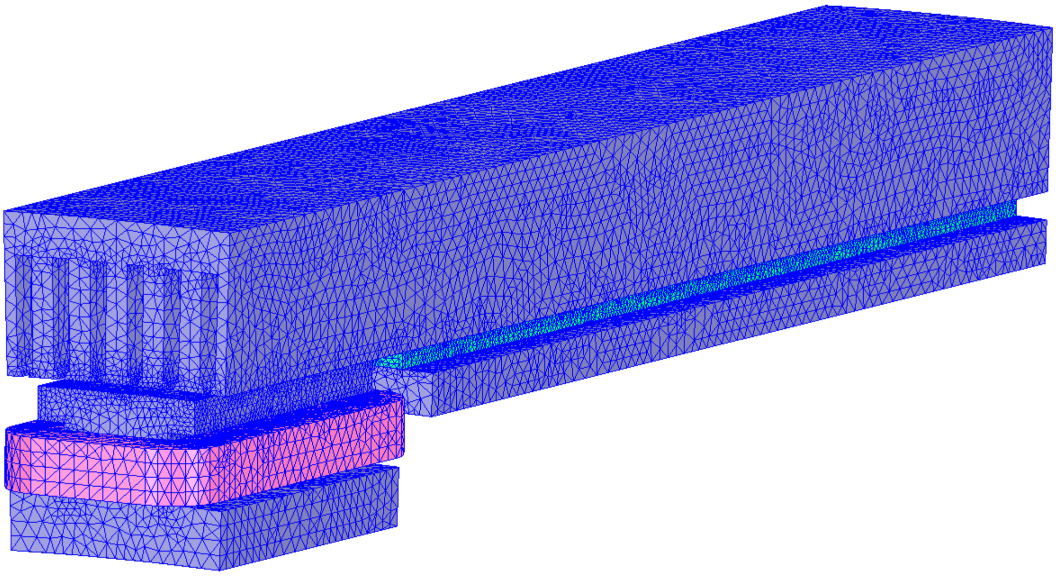

Figure 4.18: The mesh distribution of one pole of the whole generator in 3D FEA model.

In magneto-static solution type, the mesh elements are generated by iterations aiming at minimum error in calculated energy. Therefore, this solution type is very useful to analyze the flux density and magnetic field distribution.

The most critical region is where the PM and end windings of the WF interact. The flux density vectors between excitation sections and along the field windings are shown in Figure 4.19 where magnetic field vectors ar the same region is given in Figure 4.20. As seen from the figures, a little amount of the leakage flux flows through the magnets. Moreover, the magnetic field intensity in the corresponding part of the stator is very low. The investigated plane in the axial cross-section lays in the midpoint of a pole. The flux density vectors plotted at an axial plane of full length is given in Figure 4.21.

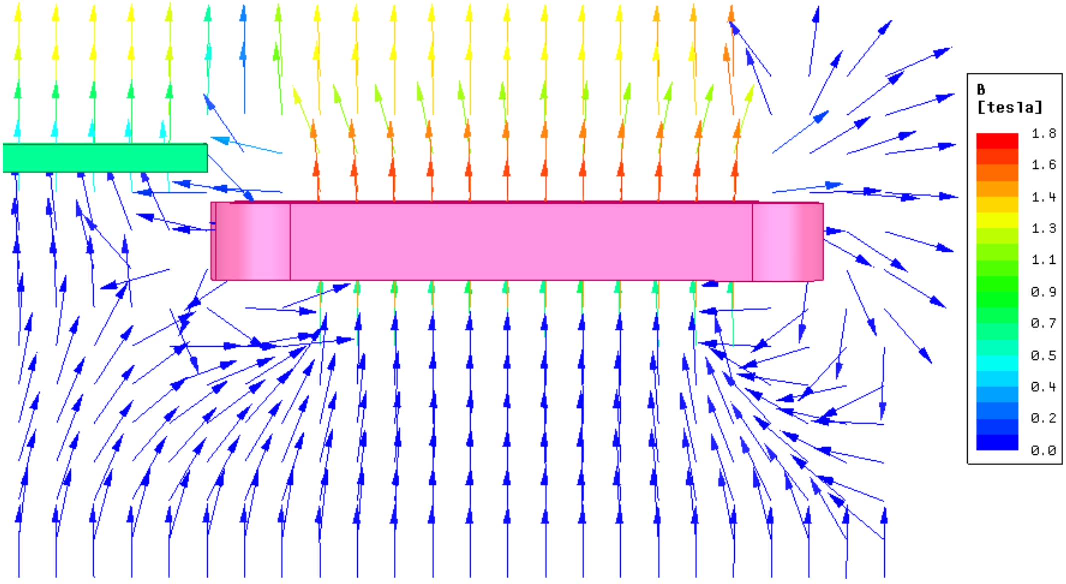

Figure 4.19: Flux density vectors resulting due to field windings.

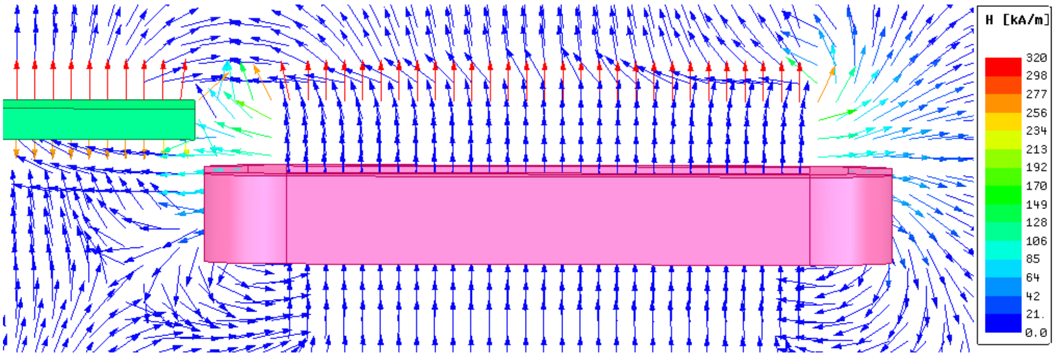

Figure 4.20: Magnetic field vectors resulting due to field windings.

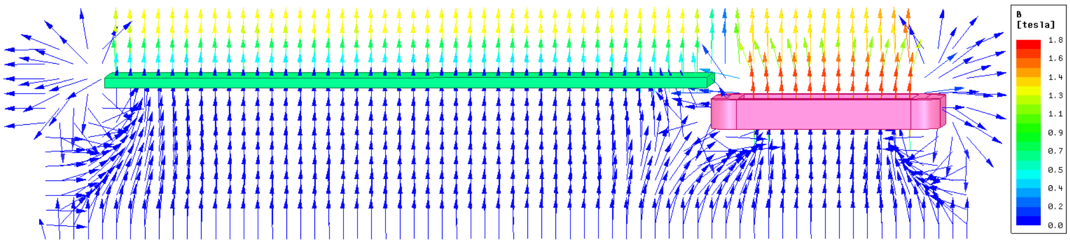

Figure 4.21: Flux density vectors at the axial plane of full length.

The flux density distribution at the same axial plane where the flux vectors are plotted is given in Figure 4.22. A closer look at flux density at WF section and interaction region is presented in Figure 4.23. The simulation is conducted at no load, therefore the density in the stator is in 1.3-1.4 Tesla range.

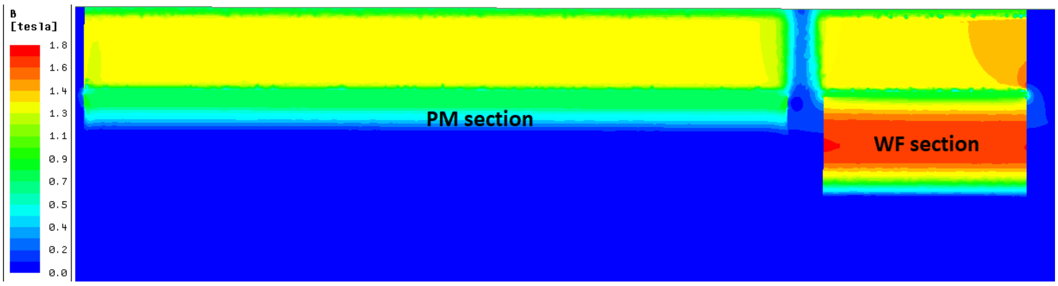

Figure 4.22: Flux density distribution in axial plane in the midpoint of a pole.

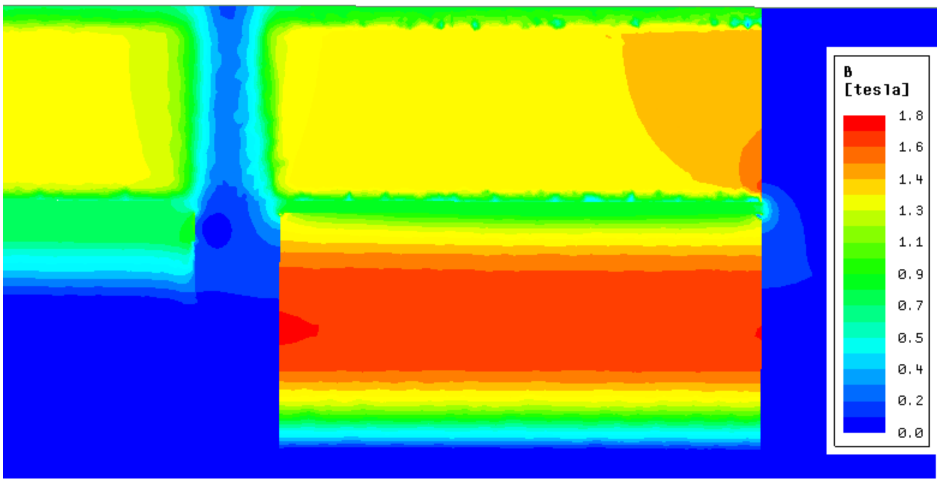

Figure 4.23: Closer look at flux density distribution in axial plane of WF section.

The flux density magnitude between the PM and end windings is nearly 0.3 Tesla. This value is nearly same with the region of the end windings located at the other edge. However, the region where the flux density is observed is slightly larger due to PM interaction. There exist a region with a higher density in the pole shoe of the WF section. This is also a result of PM interaction since the magnet pulls a higher amount of flux than the air that surrounds the end windings at the other edge.

Another important point is that the flux density in the stator's closest region to the WF end windings witnesses a higher flux density. This phenomena would have been seen at the other edge of WF if this was a fully electrically excited machine. However, the most of the flux resulting due to end windings flows towards the magnet instead of completing its path through the stator. The result is an asymmetrical flux density distribution at the axial plane of the WF section.

The flux density variation at different cross-sections can also be seen through an arc which stator slots and teeth as seen in Figure 4.24. The densities may differ from edge to the midpoint of the stator as mentioned above due to interaction of sections and leakage flux. However, it is seen that the average of the areas under the flux density graphs are nearly the same with the graphs obtained with 2D simulations.

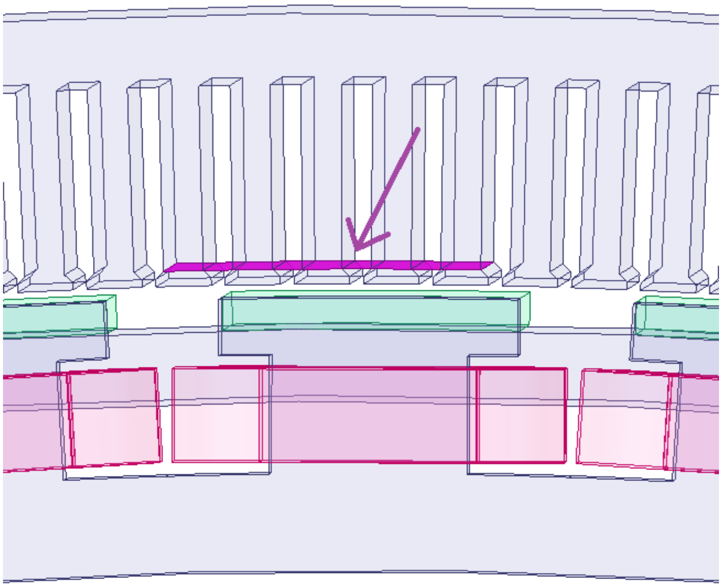

Figure 4.24: The plane crossing the teeth and slots to measure flux density.

Figures 4.26 and 4.27 show flux densities along an arc drawn on a pole of the stator according to 2D and 3D simulations. In 3D case, different cross-sections are evaluated assuming the PM edge is the zero point as seen in Figure 4.25. The 2D and 3D results being compatible indicates that the flux per pole and hence the induced voltage values would also be similar.

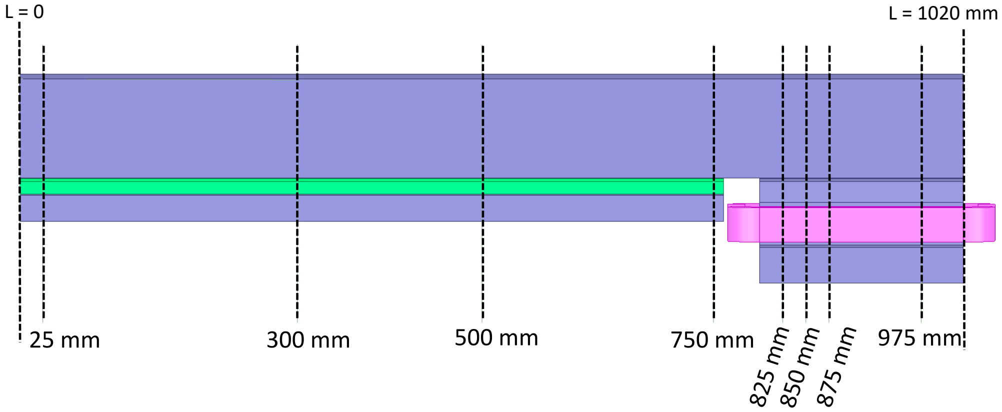

Figure 4.25: The location of cross-sectional planes where flux densities are measured.

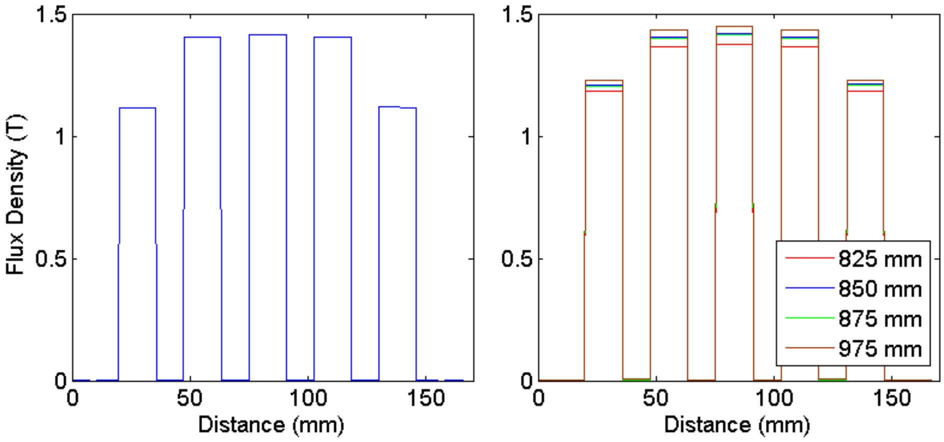

Figure 4.26: Flux density along an arc located in the stator teeth at 2D (left) and 3D (right) simulations for WF section.

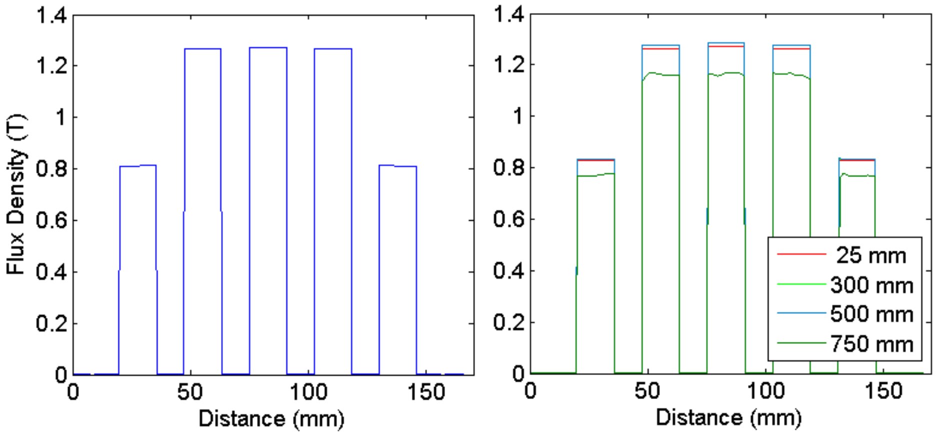

Figure 4.27: Flux density along an arc located in the stator teeth at 2D (left) and 3D (right) simulations for PM section.

Although magneto-static solver is capable of calculating the flux density with a narrow margin of error, it cannot directly display the variation of time dependent variables like induced EMF. One way to obtain the induced EMF is to record the flux passing through a certain area while the rotor position is changed slightly in each step, multiplying it with turns ratio and then differentiating the resulting flux linkage as Eq. 4.1 stated where λ is flux linkage, N_{ph} is the number of turns per phase, B is the flux density and E_a is the induced voltage.

$$\lambda = N_{ph} \oint BdA \qquad \& \qquad E_a = -\frac{d\lambda}{dt} \tag{4.1}$$

In order to apply the given mathematical relation, a model with 4 pole of the designed hybrid excited machine is constructed as seen in Figure 4.28 where the area that the flux is to be integrated over is the swept version of the arc given in Figure 4.24 along the axial direction.

Using the given model, the rotor is rotated by 0.1 degree each time and the normal component of the flux density is integrated over the surface covering the area between the windings belonging to a certain phase. A half cycle of flux density variation is obtained by applying parametric sweep, however the solver failed to calculate the flux at a couple position. Therefore these values are calculated via interpolation and the whole waveform is constructed bu using symmetry. Figure 4.29 shows, the resulting

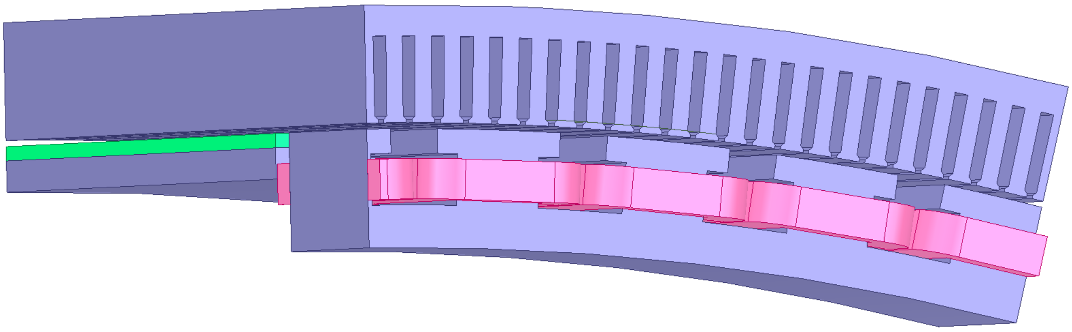

Figure 4.28: The model containing 4 pole to obtain flux linkage as the rotation angle is gradually changed.

flux density and a pure sinusoidal waveform with the same frequency and magnitude. The peak value of the flux density is recorded to be 6.4 Wb.

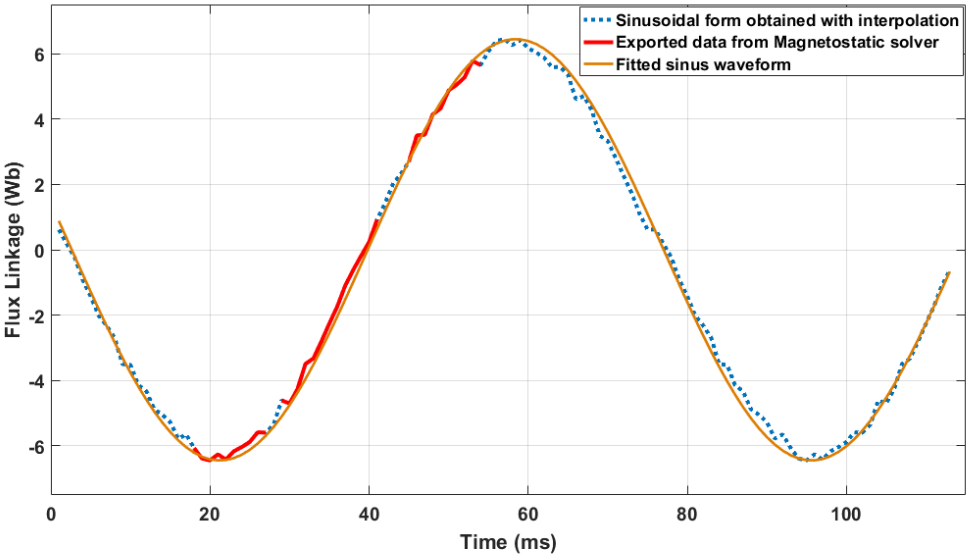

Figure 4.29: Flux linkage obtained by sweeping rotation angle.

The derivative of the flux linkage with respect to time yields the induced phase voltage. However, due to inadequate mesh elements and parametric sweep steps for rotor angle being too large, the differentiation results in an unrealistic waveform containing high order harmonics as seen in Figure 4.30. Nonetheless, the fundamental component of the waveforms has an rms value of 640 V which is just 3% lower than the value obtained via 2D simulations.

Even though magneto-static solution type yielded approximate data about induced EMF, the findings are said to be compatible with analytical calculations and 2D simulations.

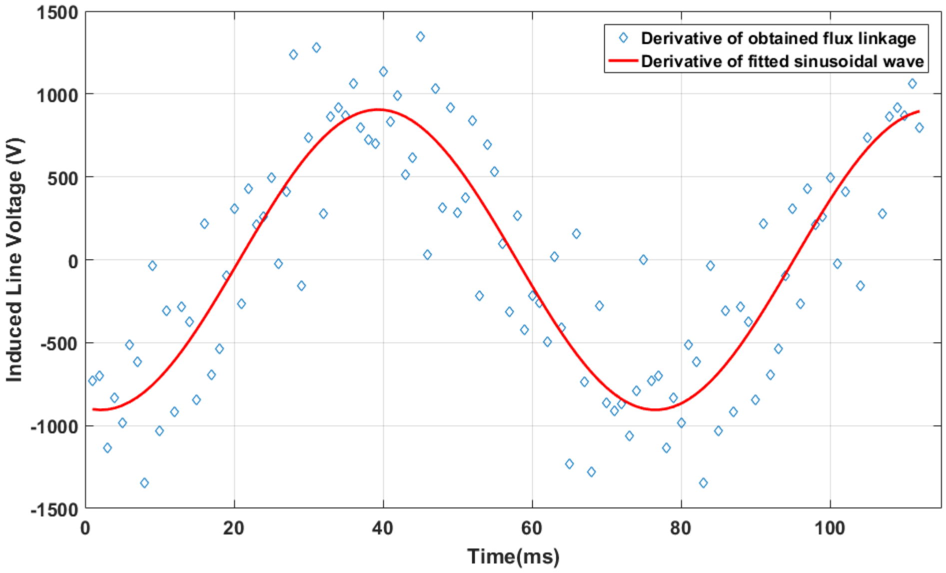

Figure 4.30: Induced EMF waveforms obtained by differentiating exported and approximated flux linkages.

4.3.2 Transient Solution Type

Transient solution type enables us to observe time variation of the parameters of the simulated model. However, transient solver does not have adaptive meshing capability and hence, the mesh elements can be either exported from RMxprt module or fully defined by the user. Moreover, the transient solution generally takes longer than the magneto-static solution does.

The flux linkage waveforms that transient solver provided are given in Figure 4.31. The peak value of the wave is 6.6 Wb which is slightly higher than that of seen in Figure 4.29.

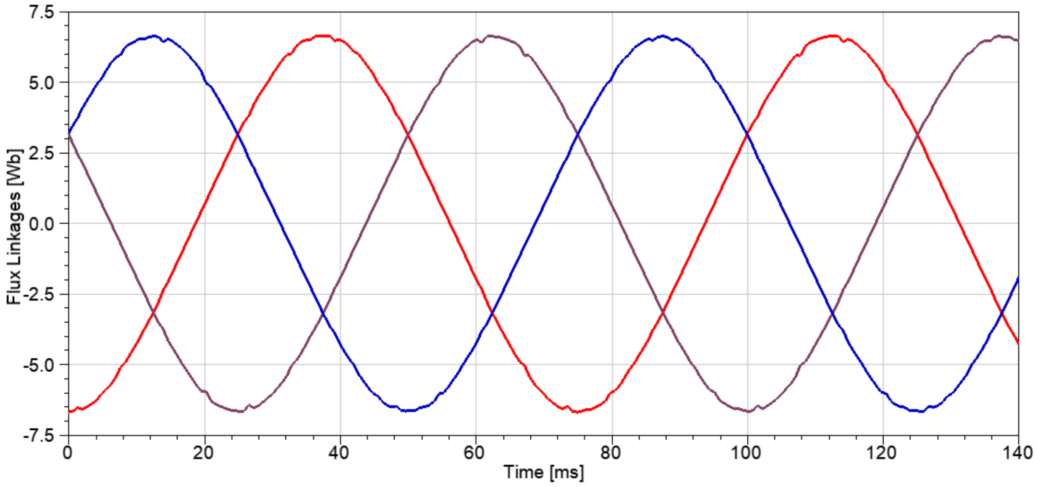

Figure 4.31: Flux linkage waveforms obtained with transient solver.

The flux linkage waveform is smoother than the waveform obtained by using magnetostatic solver. As a result, the distortion due to differentiation is lower as seen in Figure 4.32. The fundamental component of the wave is 668 V, 1.2% higher than the value obtained via 2D simulations.

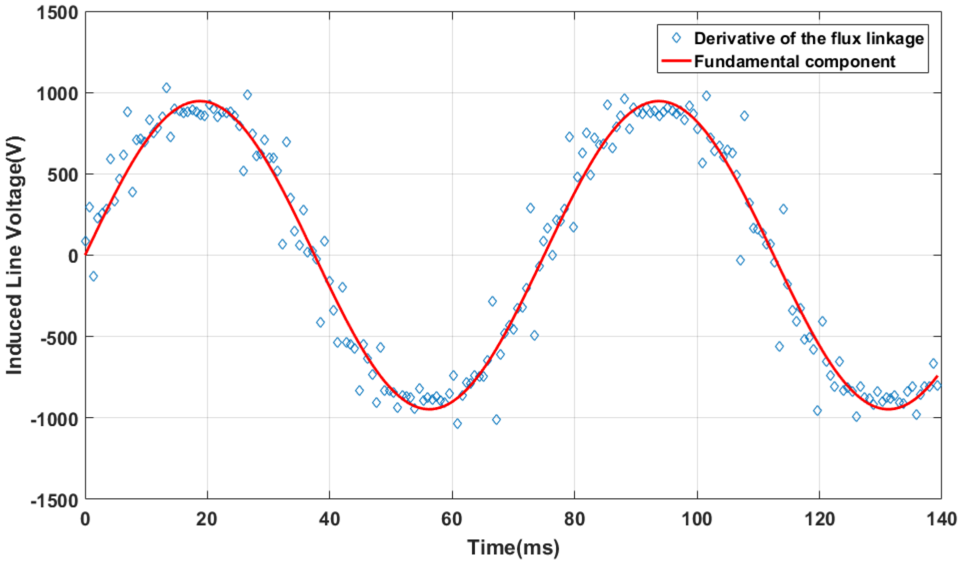

Figure 4.32: The resulting induced EMF and the fundamental component of the waveform.

The transient solver reveals a more accurate induced EMF waveform; however, the waveform still contained spikes and high order harmonics due to insufficient mesh elements. Finer mesh operation and shorter step time would definitely yield a more accurate waveforms. Nonetheless, in order to solve this finite element problem, more computational power is needed although the findings are compatible with the expectations.

4.4 Discussion and Comments

Under this chapter, 2D and 3D FEA results of the designed HESG are presented. It is shown that, the simulations conducted in ANSYS Maxwell software are compatible with analytical calculations as summarized in Table 4.2. Following remarks can be made according to the simulation results;

Table 4.2: Comparison of analytical results with 2D and 3D simulations.

	Analytical calculations	**2D FEM simulations**	**3D FEM simulations**
Fundamental component of induced voltage, E_a	650 V	660 V	668 V
Peak air-gap flux density in the PM section, B_g	0.75 T	0.77 T	0.77 T
Peak air-gap flux density in the WF section, B_g	0.88 T	0.86 T	0.86 T
Peak of the flux linkage, λ	6.3 Wb	6.5 Wb	6.66 Wb
Phase inductance of PM section, L_{ph}	0.5 mH	0.68 mH	-
Q-axis equivalent inductance of WF section, L_q	0.3 mH	0.31 mH	-
Inductance due to extended region in the stator	9 μ H	22 μ H	-
Phase resistance, R_{ph}	7.8 mΩ	9.6 mΩ	-

- There exists a gap of nearly 4 cm between PM and WF rotors including end windings. This gap causes the stator to be longer and the corresponding region in the stator witnesses a very low flux density. According to the inductance matrix calculation done in Maxwell 2D, this extension in the armature windings results in an inductance of 22 μ H. The corresponding inductances of WF and PM parts can be treated as series inductances. Since the equivalent inductances of the WF and PM sections are 0.3 and 0.5 mH, respectively; neglecting this gap in the analytical design process is a valid assumption. However, the power factor is slightly lower when the inductance of this section is included.

- Due to the extension in the stator due to end windings of the field and the gap between two rotors, in 3D simulations, total induced voltage may slightly increase when compared to the estimated value with 2D simulations where that extension is discarded. The rms value of the fundamental component of the induced line voltage is found to be 668 V with 3D transient solver, whereas the summation of the separately simulated sections is 660 V. Although it may seem feasible, the error margin of the 3D transient analysis must be considered.

- 2D analysis cannot reveal the difference in flux density distribution in the core regions located near to and far from the edges as pointed in Figure 4.33. Figures 4.34 and 4.35 display flux density distributions at the different cross-sections along the axial length. The rotor back-cores near to the edges witness a higher flux density than the regions located in the middle. This is due to the increased non-radial flux near to the edges.

- The PM and WF interaction causes an asymmetrical flux density distribution at the axial plane. Density in a narrow region in the WF rotor pole shoe gets higher due to the magnet pulling flux to itself. Moreover, as clearly seen in Figure 4.35, the density in the stator region closer to the edge is higher because of the leakage flux completing path through stator.

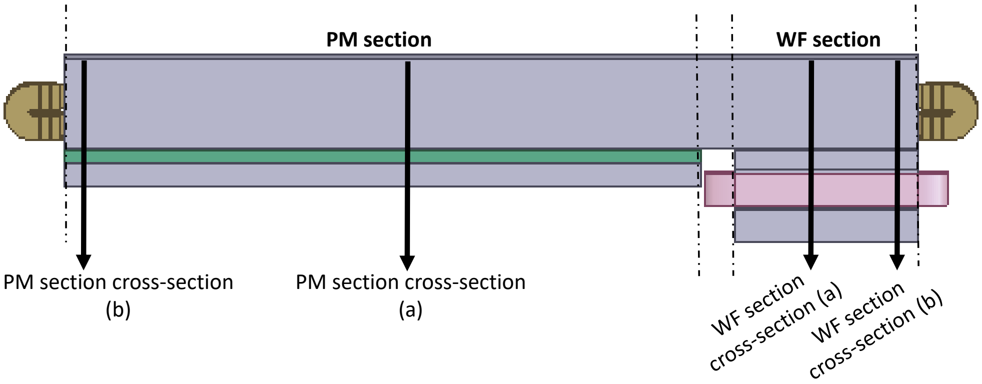

Figure 4.33: The cross-sections to plot flux density distribution in different regions of the sections.

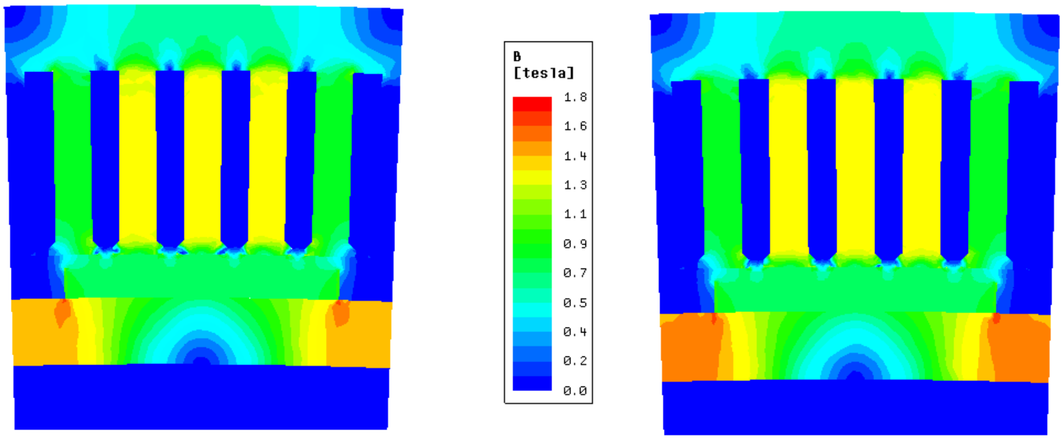

(a) Flux density distribution in the middle of PM section.

(b) Flux density distribution near the armature end windings.

Figure 4.34: Flux density distribution at different cross-sectional planes of PM section.

- Even though both magneto-static and transient solver yielded distorted EMF waveforms, gave more accurate results are achieved with the transient solver. Further improvement of the waveform leans on more computational power as the processors of the regular computers are not capable of solving finite element problem defined on such a huge geometry that requires too many mesh elements.

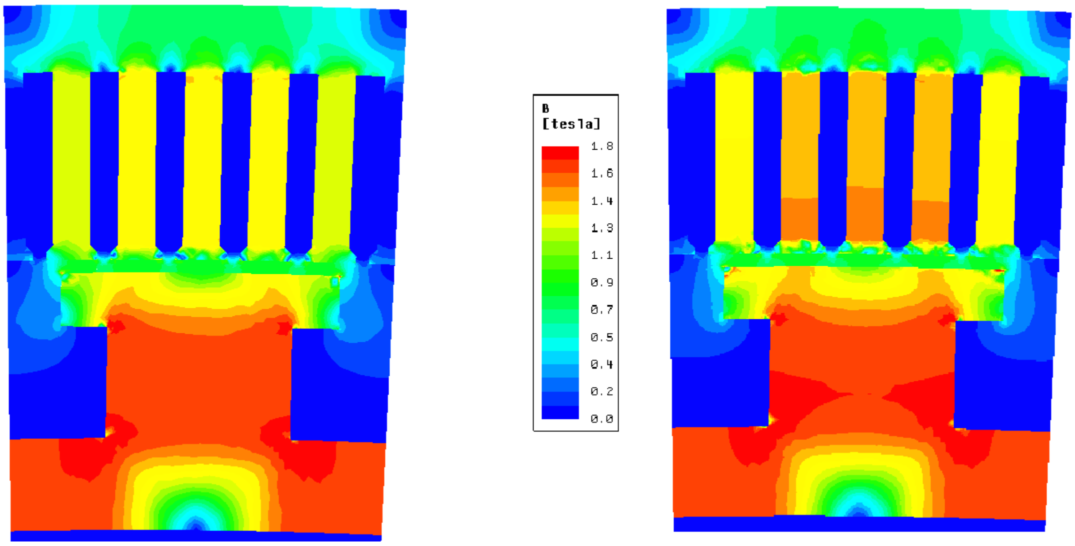

(a) Flux density distribution in the middle of WF section.

(b) Flux density distribution near the armature end windings.

Figure 4.35: Flux density distribution at different cross-sectional planes of WF section.

- The design of the selected HESG topology is verified by FEM simulations and it is shown that HESGs can be designed bu using similar approach used for EESG and PMSGs where it is aimed to combine the advantages of those two topologies. However, benefits and downsides of the utilizing direct drive HESG in wind turbines need to be questioned. This investigation mostly relies on the performance of the topology compared to the ones available in the industry. In the final chapter of the thesis, the designed 2.5 MW direct drive generators are compared.

CHAPTER 5

COMPARISON OF THE DESIGNS

5.1 Introduction

In this chapter, 2.5 MW 16 rpm direct drive PMSG, EESG and Hybrid Excited Synchronous Generator whose design procedures are conveyed in the previous chapters are compared. The harmonic content of the induced voltage waveforms in the armature windings are evaluated for each topology by applying FFT analysis in MATLAB. Total harmonic distortion (THD) of the line voltages are calculated accordingly.

In addition to the operation of the generator under nominal conditions, the response of the system to a short circuit event is extremely important to avoid damaging magnets and mechanical components. Hence, a short circuit scenario is simulated and the short circuit torque and currents are recorded. According to the results, short circuit characteristics of the given topologies are discussed.

So far, only the active mass of the generator, that is the mass of the components in the generator which participates the electricity generation, is taken into account. However, inactive or structural mass which contains the mechanical support structures for these direct drive topologies can be even larger than the active mass. Therefore, based on a support structure model given in literature, inactive mass of the given topologies is estimated.

In addition, the dimension and performance parameters calculated through analytical design or extracted from ANSYS Maxwell are summarized for the three generator designs under investigation.

According to the stated findings, the designed 2.5 MW hybrid excited synchronous generator is evaluated and the feasibility of the topology is discussed.

5.2 Harmonic Content of the Induced Voltage

The total harmonic distortion (THD) of the line voltage effects the quality of the power delivered to the grid converter and should be minimized. THD is directly calculated from the magnitudes of fundamental and higher order harmonic components of the waveform.

In Y-connected machines, third order harmonic components do not exist in the line voltage. Moreover, the 5^{th} & 7^{th} harmonic components can be effectively reduced by choosing winding the pitch ratio for short-pitched winding as $5/6$. The next effective harmonic orders are 11^{th} and 13^{th} which may be dominant in the harmonic spectrum. Figure 5.1 reveals the FFT analysis of the induced line voltages of 2.5 MW PMSG and EESG. THD of induced EMF of PMSG is found to be 2.6% whereas that of EESG is nearly 2%.

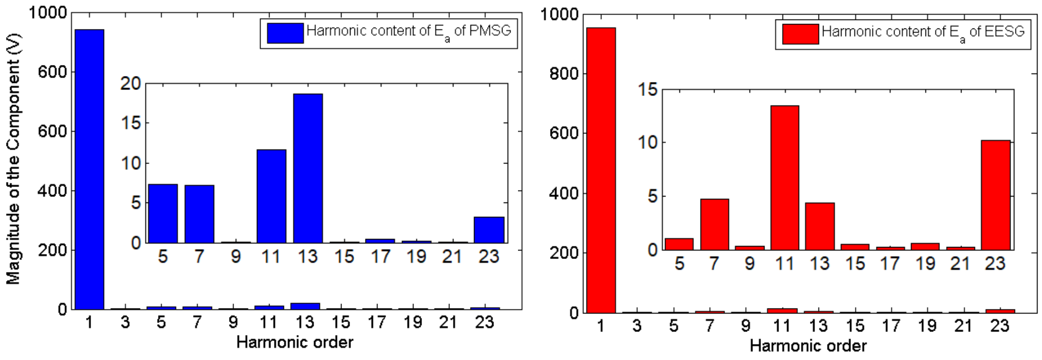

Figure 5.1: FFT analysis of the induced line voltage of PMSG (left) and EESG(right).

The harmonic content of the 2.5 MW hybrid excited synchronous generator is given in Figure 5.2. The THD of the corresponding induced EMF waveform is 2.4%.

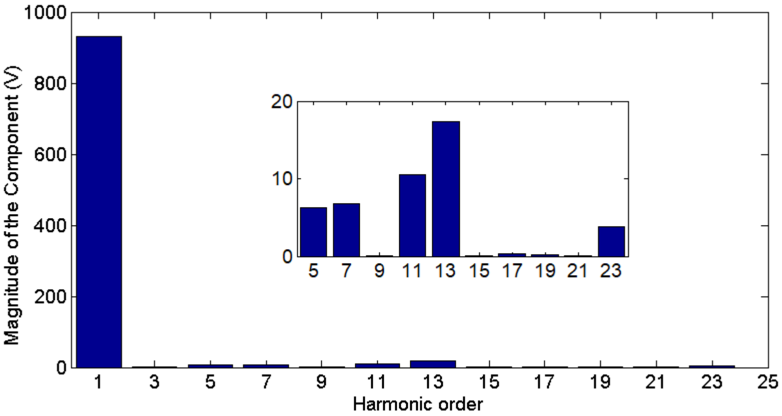

Figure 5.2: FFT analysis of the induced line voltage of HESG.

As seen from the given spectra, the trend in harmonic content is similar among the given topologies. This is expected since the pitch ratio of the armature windings for each topology is the same and therefore 5^{th} & 7^{th} order harmonics are successfully suppressed. Moreover, the magnet embrace for PM rotor and pole shoe embrace for WF rotor are selected to be same. These embrace ratios affect the harmonic content of the flux density and therefore that of induced voltage. The rms values of harmonic components of the induced voltages of the investigated generators are listed in Table 5.1.

Table 5.1: RMS values of harmonic components of induced voltages of PMSG, EESG and HESG.

Harmonic component	**PMSG**	**EESG**	**HESG**
Fundamental	663 V	672 V	659 V
5^{rd} order	5.17 V	0.73 V	4.42 V
7^{th} order	5.04 V	3.34 V	4.79 V
11^{th} order	8.20 V	9.54 V	7.42 V
13^{th} order	13.15 V	3.08 V	12.30 V
23^{th} order	2.28 V	7.21 V	2.66 V

5.3 Short Circuit Analysis and Structural Mass

5.3.1 Short Circuit Characteristics

In addition to the performance parameters under nominal operation conditions, the short circuit characteristics of the generators have a significant importance. Excessive amount of current may flow through windings due to short circuit event, which causes a very high copper loss and even demagnetization of the magnets in case of PM motors. Moreover, the resulting short circuit torque may damage the generator structure and even causes the support mechanism to break.

The support structure needs to be designed to withstand the short circuit torque and a protection mechanism which has an immediate response capability needs to be included in the system.In this section, three-phase short circuit case is simulated as a worst case to evaluate the performance.

In Figure 5.3 and 5.5, the short circuit current of a phase and resulting output torque under three phase fault are given for the PMSG, respectively. The maximum current is recorded to be 9.12 kA which is nearly three times the rated current (2.25 kA). The short circuit torque is 2.65 MN.m and it is reached in a time period less than 10 ms. This value is 76% higher than the rated torque (1.5 MN.m).

In Figure 5.4 the short circuit current of a phase is given and its maximum value is estimated to be 8.44 kA for the designed EESG. The short circuit torque is given in Figure 5.6 and its slightly higher than that of PMSG.

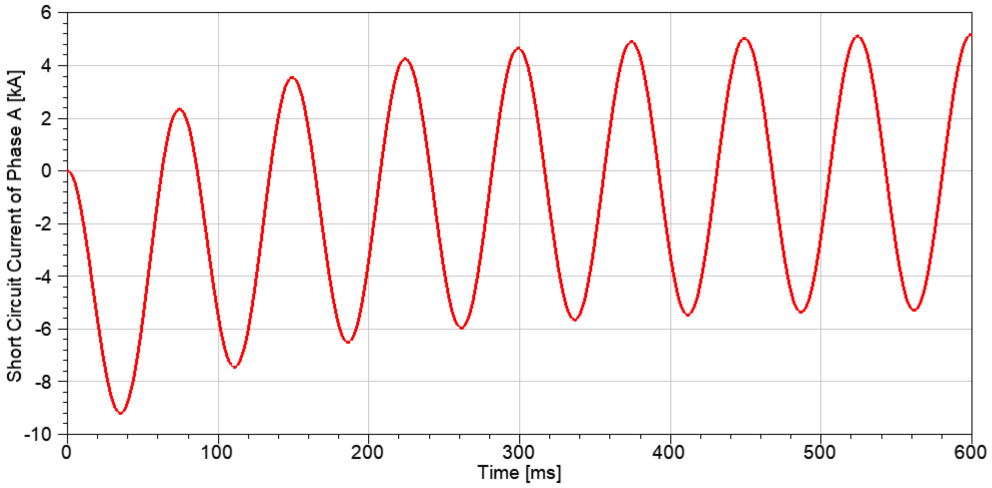

Figure 5.3: Short circuit current of phase A of full scale PMSG.

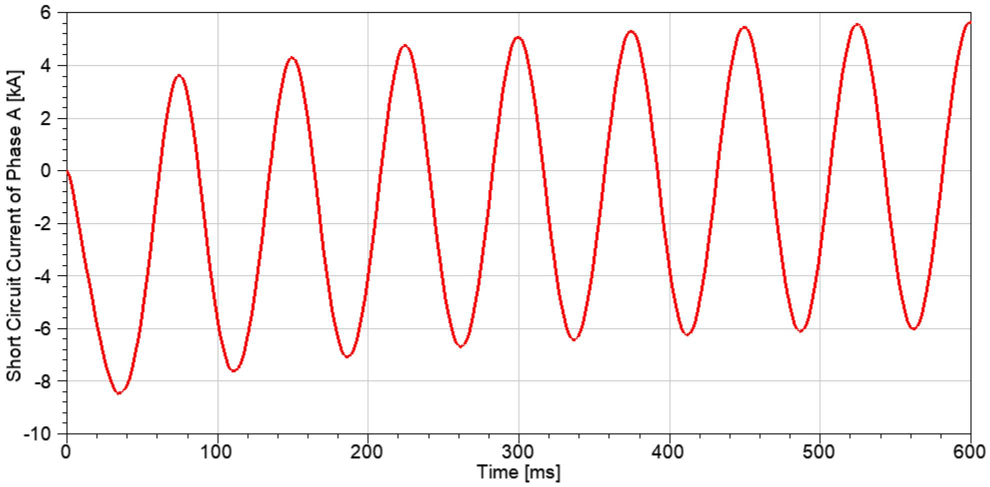

Figure 5.4: Short circuit current of phase A of full scale EESG.

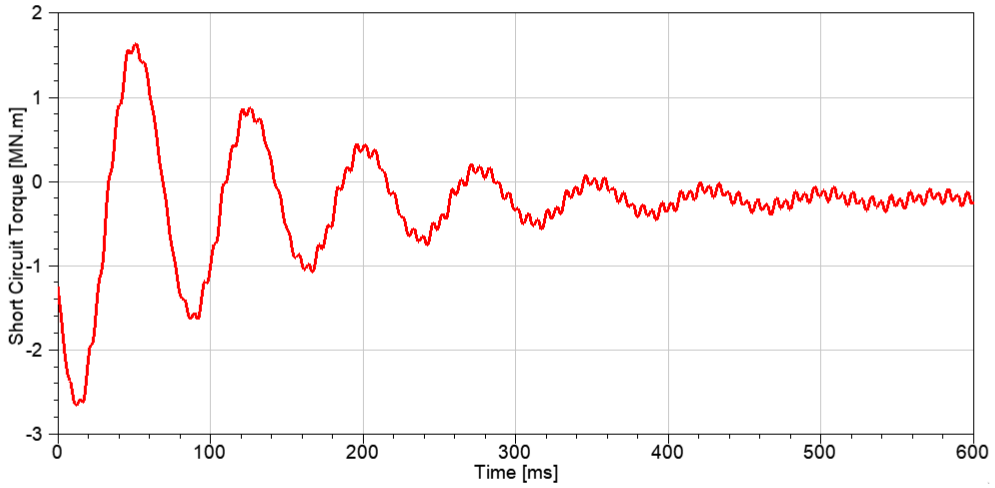

Figure 5.5: Short circuit torque of full scale PMSG.

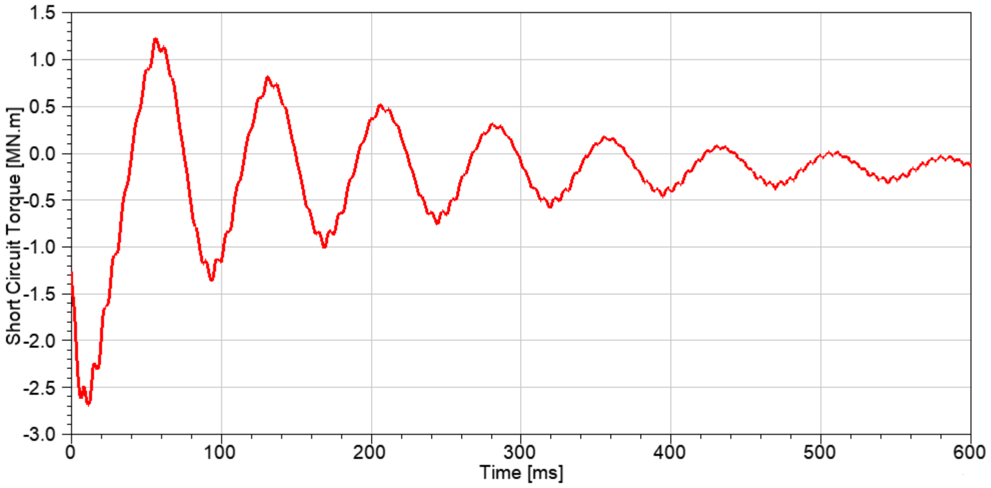

Figure 5.6: Short circuit torque of full scale EESG.

The short circuit characteristics of the HESG is also analyzed in Maxwell 2D environment by separately applying the fault scenario to each excitation sections. The output torque of both sections and total torque are given in Figure 5.7. The maximum value reaches 1.95 MN.m whereas the rated torque is nearly 1.5 MN.m. The peak of short circuit current is calculated to be 6.33 kA by using the phase inductance and resistance.

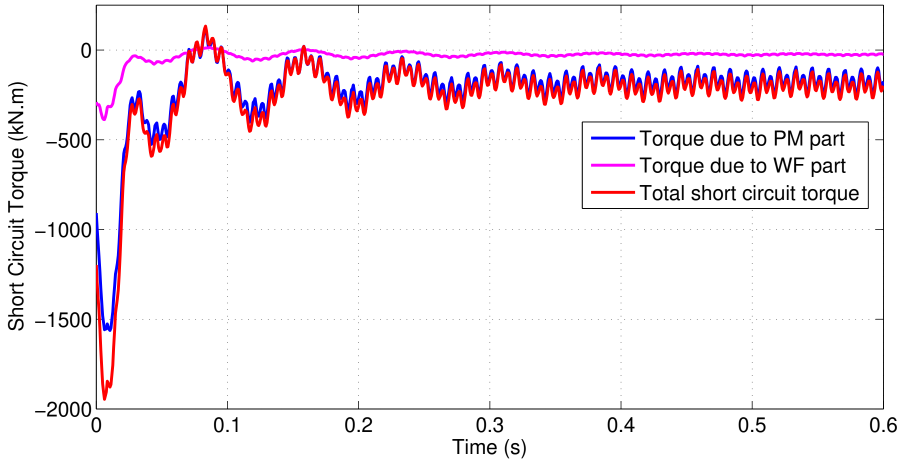

Figure 5.7: Short circuit torque of the HESG.

The findings of the short circuit analysis are given in Table 5.2. HESG has lower short circuit current due to the increased equivalent inductances and hence short circuit torque is also lower. The peak values of the short circuit torque of EESG and PMSG are similar. Nevertheless, EESG would require heavier structural mass due to larger dimensions and weight. The largest short circuit current is estimated for PMSG and the consequence of current at such level may result in demagnetization of PM.

Table 5.2: Short circuit characteristics of PMSG, EESG and HESG.

Parameter	**PMSG**	**EESG**	**HESG**
Short circuit torque	−2.65 MN.m	−2.68 MN.m	−1.95 MN.m
Short circuit current	−9.12 kA	−8.44 kA	−6.33 kA

One of the most important properties of the hybrid excitation is the ability to control the field excitation and the terminal voltage. Therefore, the possibility of altering field current to suppress the fault current emerges. The short circuit current of the WF section while field current is decaying to zero is given in Figure 5.8.

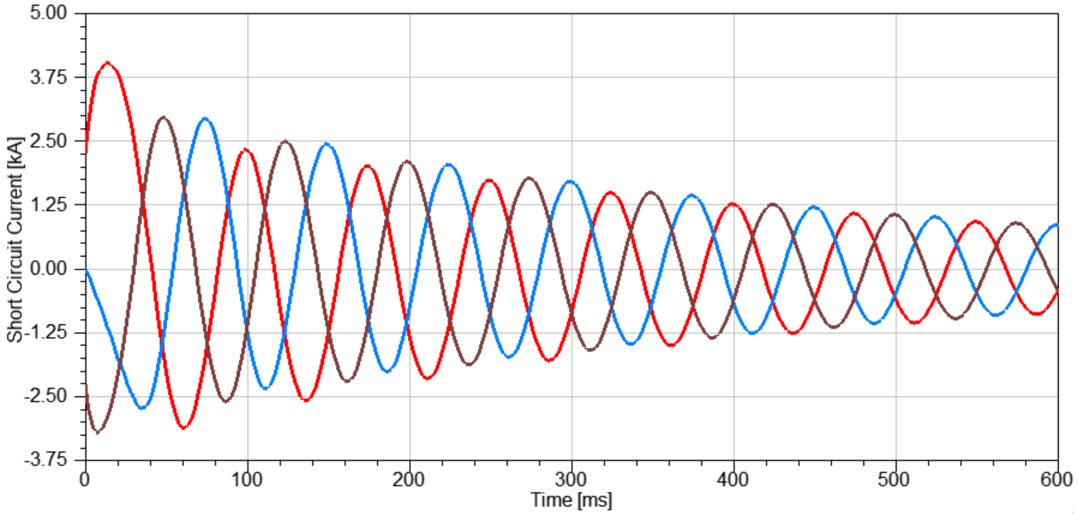

Figure 5.8: Short circuit current while field current decays.

Nonetheless, as stated in the Section 4.2.3, the time constant of field winding is nearly 0.5 seconds whereas the maximum short circuit torque is reached within milliseconds. Hence, although reducing field current imposes decay upon fault current and reduces the copper loss, it can not prevent the consequences of the maximum short circuit torque and current. The decay of the field current can be accelerated by applying negative voltage to the excitation terminals as shown in Figure 5.9. Still, the desired quick response is not reached.

Therefore, if the short circuit events are desired to be taken under control by immediate response of the field current, the winding configuration of the field needs to be rearranged to yield a reduced time constant. To be more specific, parallel connection of the field windings may be considered instead of series connection in order to decrease the equivalent winding inductance and hence the time constant. However, parallel connection of the windings requires an excitation system that can supply field current to each winding of a hundred poles. To avoid such an excessive current requirement; the area of field winding conductors, the number of turns in the winding and the height of the rotor pole can be altered. In this case, the mass of the poles, the copper loss and efficiency must be recalculated.

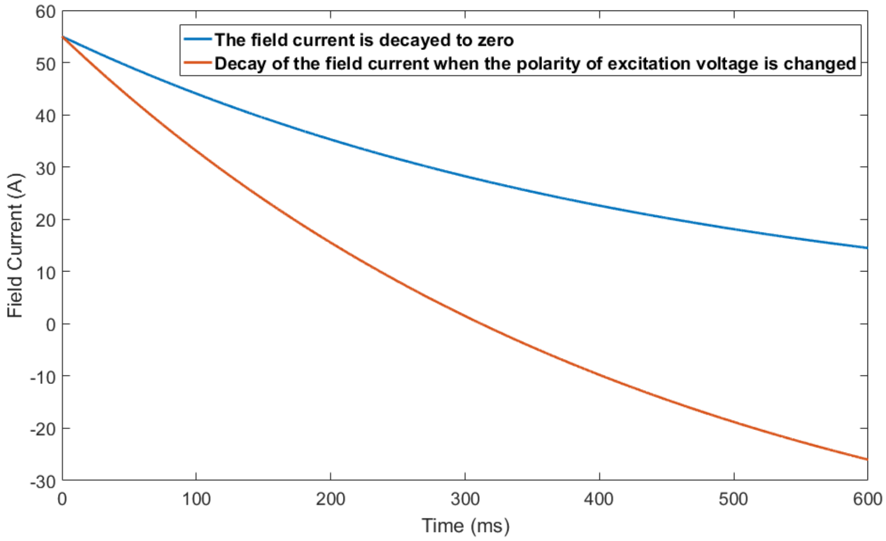

Figure 5.9: The decay of the field current for different cases.

5.3.2 Estimation of the Structural Mass

In direct drive applications, where speed is low and torque rating is high, electrical machines require a solid support structures which come out to be heavy and bulky, especially direct drive generator designs.

There are various types of support structures as stated in [49] where several applicable models for PM wind turbine generators are compared. However, in [50], an analytical method is proposed to calculate the structural mass by using stator bore diameter, rotor diameter, maximum air-gap flux density and mechanical torque of the generator. In the study, the mechanical distortion and mass of the structures are estimated by considering Maxwell stress, gravitational pull and centripetal force. Moreover, both analytical and FEA tools are presented that can optimize the required structural mass.

In this thesis, the analytical optimization presented in [50] is adapted to predict the approximate mass of the support structure bu using generator parameters. The adapted five armed structural model is shown in Figure 5.10.

The results of the applied analytical model are given in Table 5.3. Both the mass of support structure and its share on total material cost are highest for EESG topology.

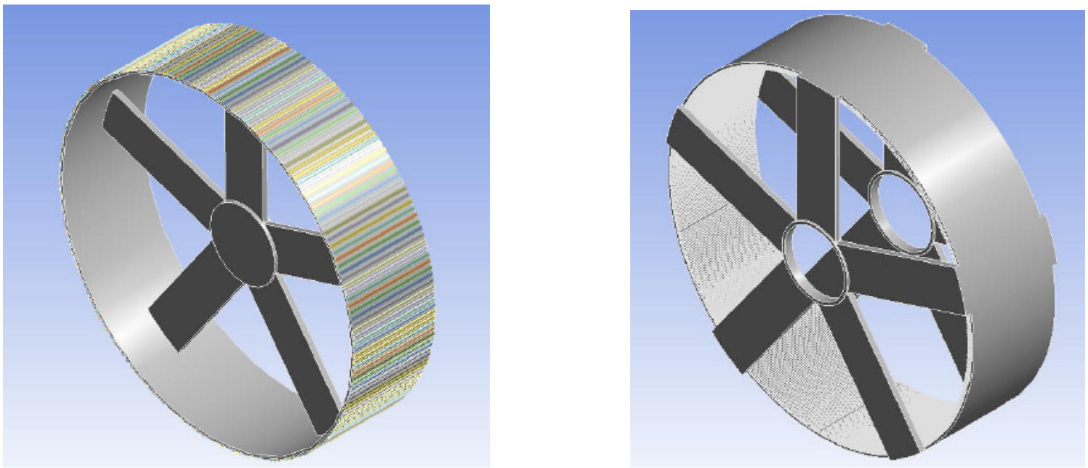

(a) Rotor structure.

(b) Stator structure.

Figure 5.10: Support structures with 5 arms for the rotor and the stator [50].

Table 5.3: Comparison of active and inactive mass of PMSG, EESG and HESG.

	PMSG	**EESG**	**HESG**
Active mass	16.9 t	33.1 t	19.2 t
Structural mass	36 t	48 t	37 t
Cost of the inactive mass	\$ 108k	\$ 144k	\$ 111k
Cost of the active mass	\$ 157.3k	\$ 140.9k	\$ 150k
Total material cost	\$ 265.3k	\$ 284.9k	\$ 261k
Share of inactive material cost	40.7%	50.5%	42.5%

These presented numbers are useful to predict the overall mass and material cost; however, it must be considered that the resulting structure needs to be verified by mechanical FEA and/or different mechanical modeling and simulation methods.

5.4 Overall Results

The dimensions, parameters and obtained performance values are shared altogether to compare the three topologies, namely PMSG, EESG and HESG which have the same output power, rotational speed and terminal voltage ratings. Moreover, the air-gap length, number of poles and ratio of magnet/pole shoe over pole pitch (embrace) are equal as listed in Table 5.4 with other common design parameters.

Table 5.4: Common design parameters for the PMSG, EESG and HESG.

Parameter	**Value**
Rated power, P_{out}	2.5 MW
Rated terminal voltage, V_t	690 V
Air gap length, g	5.5 mm
Number of poles, p	100
Number of slots s	600
Number of parallel branches in armature	100
Magnet/pole shoe embrace	0.72

The main dimensions of the designs are given in Table 5.5. The HESG and PMSG have the same outer diameter as the stator of the PMSG is adapted in the HESG design. The outer diameter and axial length of the EESG is larger than the others as expected because power density in lower than PM based synchronous machines.

Table 5.5: Main dimensions of the designed PMSG, EESG and HESG.

Parameter	**PMSG**	**EESG**	**HESG**
Outer diameter, D_o	5436 mm	5465 mm	5436 mm
Stacking length, L_{stk}	1015 mm	1053 mm	1020 mm
Number of turns per slot, N_a	76	52	76
Number of turns in field, N_f	-	105	83
PM thickness, L_m	13 mm	-	13 mm

The performance parameters are listed in Table 5.6. The PMSG has the highest efficiency thanks to the absence of the field windings and reduced core loss. The THD values of the induced EMF waveforms turn out to be similar mostly due to the fact that the pitch ratio of armature windings and the magnet/pole shoe embrace are equal for all three generators.

Table 5.6: Performance parameters of the PMSG, EESG and HESG.

Parameter	**PMSG**	**EESG**	**HESG**
Induced line voltage, E_a	658 V	667.2 V	650 V
Core loss, P_{core}	12.3 kW	20.1 kW	12.3 kW
Armature copper loss, Pcu_a	119.3 kW	77.1 kW	117.9 kW
Field copper loss, Pcu_f	-	90.8 kW	25.1 kW
Efficiency, η	95%	93%	94.1%
Power factor	0.9	0.9	0.86
THD of induced EMF	2.6%	2%	2.4%

The result of the mass and cost calculations are shared in Table 5.7. According to the estimation including structural mass, the overall cost is the highest for EESG although the cost of the active mass of the PMSG is higher.

Table 5.7: Mass and cost values of the PMSG, EESG and HESG.

Parameter	**PMSG**	**EESG**	**HESG**
Iron mass, M_{iron}	13.4 t	27.2 t	14.7 t
Magnet mass, M_{magnet}	1.2 t	-	879 kg
Copper mass, M_{cu}	2.3 t	5.9 t	3.5 t
Active material mass, M	16.9 t	33.1 t	19.2 t
Structural Mass	36 t	48 t	37 t
Active material cost, C_a	\$ 157.3k	\$ 140.9k	\$ 150k
Total material cost, C	\$ 265.3k	\$ 284.9k	\$ 261k

According to the presented findings, some of the parameters of the HESG turn out to be in between those of PMSG and EESG. As expected, these are efficiency, axial length, material mass and cost values.

Two of the notable differences of HESG from the others are power factor and short circuit peak current which are correlated since both are dependent on the winding inductance. As discussed earlier, the pancake-type geometry of the WF section of the hybrid excited generator results in a high winding inductance, which yields poorer power factor. In return, increasing the winding inductance suppress the rapid climb of the armature current in a short circuit event.

CHAPTER 6

CONCLUSIONS

In this study, a 2.5 MW direct drive hybrid excited SG is designed and compared with Permanent Magnet and Electrically Excited synchronous generators at the same ratings to discuss the feasibility of hybrid excitation. The discussion is carried according to the findings of analytical model based on cost optimization and FEM simulations conducted in ANSYS Maxwell environment.

The hybrid excitation concept basically focuses on combining advantages of PM machines and WF excitation. Among many of the topologies presented in the literature, the one that includes two separate rotors for two different excitations is selected. According to the findings, the following remarks can be made:

- PMSG utilization in wind industry tends to increase as the power ratings of the wind turbines increase since PMSGs are efficient, power dense and reliable. However, they induce uncontrollable voltage as a result of PM excitation. Moreover, there may be fluctuations in PM costs due to economical policies although PMs are already expensive materials. Direct drive EESGs are easier to manufacture but they have bulky and massive structure. In addition, the excitation loss in the field winding is inevitable. Both PMSGs and EESGs are utilized with full scale power converter although EESG topology inherently provides the opportunity to change the induced voltage.

- The selected hybrid excited topology contains both PMs and DC excited field windings located at different rotors coupled to the same shaft. Therefore, the fixed voltage induced due to PM adds up to the variable voltage induced thanks to controllable field winding current of the WF rotor. This property is verified by electromagnetic FEM simulations as the presence of the WF rotor provides controllability over the terminal voltage and output power in a range defined by the ratio of the maximum power contribution of WF excitation section over the rated power of the whole machine. In this study, this range is 25% as the PM section is responsible from generating 75% of the rated power.

- In the proposed hybrid excited system, required PM amount is reduced by 26.7% compared to a full PMSG at the same ratings as the PM mass dropped from 1.2 tonnes to 0.88 tonnes. However,under full load, the efficiency is lower as a result of the copper loss on the field windings. The material mass and the cost of the hybrid excited SG are in between those of EESG and PMSG.
- The WF section of the hybrid excited machine has low efficiency and poor power factor when treated as a separate machine rated at 25% of 2.5 MW. This is because the aspect ratio of the design is far from the optimum point for such power level. In addition, the rated current of the armature is above 2 kA since the excitation sections share the stator, and hence the copper loss became more dominant.

  The poor power factor is a result of the increased winding inductance due to WF section of the hybrid machine. Increased winding inductance suppress the short circuit current and torque. However, this correlation can not be treated as an advantage of combining excitation types, it is more likely to be a result of selected generator geometry to do so.
- The hybrid generator topology given in [25], which is selected for investigation of hybrid excitation concept in this thesis, claims that the controllability feature of the topology thanks to WF section enables the utilization of passive diode rectifier instead of active rectifiers. As a result, the power converter would be cheaper. However, in this study, the calculations and estimations are performed assuming that the induced voltage and the load current are kept in phase via vector control. In case of a passive rectifier, the control over load angle completely depends on field current control where the range is limited. It is shown that the field windings of such a direct drive generator have a high time constant and the resulting response time would fail the system to be as robust as desired.

Moreover, with a passive rectifier, the active power control would depend on the control over turbine blades where the response time is bounded by the mechanical time constants. Therefore, adapting passive rectifier would definitely be cheaper, but the controllability enabled by the WF section would not meet the system requirements.

- The 3D FEM simulation of the proposed hybrid excitation model revealed the characteristics of leakage flux in the interaction region between PM and WF rotors. The PM rotor attracts the leakage flux that supposed to flow though air from the end windings of the field. The interaction causes asymmetrical flux density distribution in the stator core.
- The hybrid configuration also allows the system to operate at different modes considering the required power level. In other words, one of the excitation sections can be enabled or disabled according to the changing wind speed and power generation requirement. It is shown that efficiency can be maximized by operating at only PM mode at 30% and lighter load demands. At 50% rated power, the efficiency is recorded to be 96% in hybrid mode with 50% of the rated field current. Therefore, the field can be arranged according to the load demand to keep on operating at maximum allowable efficiency.
- At higher wind speeds, field weakening control may extend the operating range of the generator and also improves efficiency at higher speeds [51]. In this sense, the flexibility provided by the WF section is not limited to strengthening the effect of PM. When the polarity of the field excitation is reversed, the overall effect would be a ‘field weakening’ case where the induced voltage is reduced. The field weakening of PM machines, otherwise, would require injection of negative I_d current and hence there is always a risk of demagnetization of the magnets. By applying negative field current, field weakening may be accomplished while demagnetization risk is eliminated.

- In the design procedure, constraints regarding manufacturability are considered. However, feedbacks from manufacturers and mechanical designers are essential to yield a realistic electrical machine design. The production capability and mechanical constraints may require the electromagnetic design to be revised. Another future work is to produce and test a prototype hybrid excited machine at a lower power rating.
- As a result, hybrid excited SG is a suitable topology for MW scale direct drive wind turbines, yielding a performance not significantly better but comparable to those of EESG and PMSG.

REFERENCES

[1] REN21 - Renewable Energy Policy Network for the 21st Century, “Renewables 2016 Glabal Status Report,” tech. rep., REN21, Paris, 2016.

[2] IRENA - International Renewable Energy Agency, “Renewable Energy Technologies: Cost Analysis Series,” Tech. Rep. 5, 2012.

[3] R. Zeinali, *Design and Optimization of High Torque Density Generator for Direct Drive Wind Turbine Applications*. Ms thesis, Middle East Technical University, 2016.

[4] A. D. Hansen, F. Iov, F. Blaabjerg, and L. H. Hansen, “Review of Contemporary Wind Turbine Concepts and their Market Penetration,” *Wind Engineering*, vol. 28, no. 3, pp. 247–263, 2004.

[5] H. Li and Z. Chen, “Overview of different wind generator systems and their comparisons,” *Renewable Power Generation, IET*, vol. 2, no. 2, pp. 123–138, 2008.

[6] ENERCON, “https://www.enercon.de/en/technology/ [Last visited: May 21, 2018].”

[7] C. V. Hernandez, T. Telsnig, and A. V. Pradas, “JRC Wind Energy Status Report 2016 Edition,” tech. rep., Joint Research Centre, Directorate for Energy Transport and Climate, 2017.

[8] J. Cotrell, “A preliminary evaluation of a multiple-generator drivetrain configuration for wind turbines,” in *2002 ASME Wind Energy Symposium*, (Reston, Virigina), American Institute of Aeronautics and Astronautics, jan 2002.

[9] A. McDonald, “Hybrid excitation of synchronous generators for wind turbines,” in *2nd IET Renewable Power Generation Conference (RPG 2013)*, (Beijing, China), pp. 3.55–3.55, Institution of Engineering and Technology, 2013.

[10] F. B. McCarty, “Hybrid excited generator with flux control of consequent-pole US Patent 4,656,379,” 1987.

[11] X. Luo and T. A. Lipo, “A synchronous/permanent magnet hybrid AC machine,” *IEEE Transactions on Energy Conversion*, vol. 15, no. 2, pp. 203–208, 2000.

[12] Y. Liao, L. Feng, and T. A. Lipo, “A Novel Permanent-Magnet Motor With Doubly Salient Structure,” *IEEE Transactions on Industry Applications*, vol. 31, no. 5, pp. 1069–1078, 1995.

[13] K. T. Chau, J. Z. Jiang, and Y. Wang, “A Novel Stator Doubly Fed Doubly Salient Permanent Magnet Brushless Machine,” *IEEE Transactions on Magnetics*, vol. 39, no. 5 II, pp. 3001–3003, 2003.

[14] X. Zhu, M. Cheng, W. Hua, J. Zhang, and W. Zhao, “Design and analysis of a new hybrid excited doubly salient machine capable of field control,” in *Conference Record - IAS Annual Meeting (IEEE Industry Applications Society)*, vol. 5, (Tampa, FL, USA), pp. 2382–2389, IEEE, 2006.

[15] X. Zhu and M. Cheng, “Design, analysis and control of hybrid excited doubly salient stator-permanent-magnet motor,” *Science China Technological Sciences*, vol. 53, no. 1, pp. 188–199, 2010.

[16] Z. Zhang, Y. Tao, and Y. Yan, “Investigation of a New Topology of Hybrid Excitation Doubly Salient Brushless DC Generator,” *IEEE Transactions on Industrial Electronics*, vol. 59, no. 6, pp. 2550–2556, 2012.

[17] M. Cheraghi and M. Karimi, “Optimal Design of a Hybrid Excited Doubly Salient Permanent Magnet Generator for Wind Turbine Application,” in *8th Power Electronics, Drive Systems & Technologies Conference (PEDSTC 2017)*, (Mashhad, Iran), pp. 19–24, 2017.

[18] K. T. Chau, Y. B. Li, J. Z. Jiang, and S. Niu, “Design and control of a PM brushless hybrid generator for wind power application,” *IEEE Transactions on Magnetics*, vol. 42, no. 10, pp. 3497–3499, 2006.

[19] R. L. Owen, Z. Q. Zhu, and G. W. Jewell, “Hybrid-excited flux-switching permanent-magnet machines with iron flux bridges,” *IEEE Transactions on Magnetics*, vol. 46, no. 6, pp. 1726–1729, 2010.

[20] C. Liu, K. T. Chau, J. Z. Jiang, and L. Jian, “Design of a new outer-rotor permanent magnet hybrid machine for wind power generation,” *IEEE Transactions on Magnetics*, vol. 44, no. 6, pp. 1494–1497, 2008.

[21] X. Liu, H. Lin, Z. Q. Zhu, C. Yang, S. Fang, and J. Guo, “A Novel Dual-Stator Hybrid Excited SynchronousWind Generator,” *IEEE Transactions on Industry Applications*, vol. 45, no. 3, pp. 947–953, 2009.

[22] H. Hua and Z. Q. Zhu, “Novel Parallel Hybrid Excited Machines With Separate Stators,” *IEEE Transactions on Energy Conversion*, vol. 31, no. 3, pp. 1212–1220, 2016.

[23] J. A. Tapia, F. Leonardi, and T. A. Lipo, “Consequent-pole permanent-magnet machine with extended field-weakening capability,” *IEEE Transactions on Industry Applications*, vol. 39, no. 6, pp. 1704–1709, 2003.

[24] O. Beik and N. Schofield, “Hybrid generator for wind generation systems,” in *2014 IEEE Energy Conversion Congress and Exposition (ECCE)*, pp. 3886–3893, 2014.

[25] O. Beik and N. Schofield, “High-voltage hybrid generator and conversion system for wind turbine applications,” *IEEE Transactions on Industrial Electronics*, vol. 65, no. 4, pp. 3220–3229, 2018.

[26] Q. Wang, S. Niu, and L. Yang, “Design optimization of a novel scale-down hybrid-excited dual permanent magnet generator for direct-drive wind power application,” *IEEE Transactions on Magnetics*, vol. 54, no. 3, pp. 3–6, 2018.

[27] Turkish Wind Energy Association, “Türkiye Rüzgar Enerjisi İstatistik Raporu,” tech. rep., 2017.

[28] ENERCON, “http://www.enercon.de/p/downloads/ENERCON_Produkt_en_web_072013.pdf [Last visited: Feb 12, 2018],” 2013.

[29] C. Versteegh and G. Hassan, “Design of the Zephyros Z72 wind turbine with emphasis on the direct drive PM generator,” in *in Proceedings of the Nordic workshop on power and industrial electronics (NORPIE)*, vol. 31, (Trondheim), pp. 1–7, 2004.

[30] D. J. Bang, H. Polinder, G. Shrestha, and J. A. Ferreira, “Promising direct-drive generator system for large wind turbines,” *EPE Journal (European Power Electronics and Drives Journal)*, vol. 18, no. 3, pp. 7–13, 2008.

[31] The Switch, “Permanent magnet generators - The Switch, https://theswitch.com/wind-power/permanent-magnet-generators/ [Last visited: Jan 5, 2019].”

[32] H. Polinder, F. F. Van Der Pijl, G. J. De Vilder, and P. J. Tavner, “Comparison of direct-drive and geared generator concepts for wind turbines,” *IEEE Transactions on Energy Conversion*, vol. 21, no. 3, pp. 725–733, 2006.

[33] D. Liu, H. Polinder, A. B. Abrahamsen, X. Wang, and J. A. Ferreira, “Comparison of Superconducting Generators and Permanent Magnet Generators for 10-MW Direct-Drive Wind Turbines,” in *19th International Conference on Electrical Machines and Systems (ICEMS)*, (Chiba, Japan), IEEE.

[34] A. Akgemci, R. Zeinali, and O. Keysan, “Minimization of EMF Harmonics and Cogging Torque for a Medium Speed RFPM Wind Turbine Generator,” in *2018 7th International Conference on Renewable Energy Research and Applications (ICRERA)*, vol. 5, (Paris), pp. 342–347, IEEE, 2018.

[35] A. Rokke, *Permanent Magnet Generators for Marine Current Tidal Turbines*. PhD thesis, Norwegian University of Science and Technology, 2017.

[36] M. Cistelecan and M. Popescu, “Study of the Number of Slots/Pole Combinations for Low Speed Permanent Magnet Synchronous Generators,” in *2007 IEEE International Electric Machines & Drives Conference*, vol. 2, 2007.

[37] T. Li and G. Slemon, “Reduction of cogging torque in permanent magnet motors,” *IEEE Transactions on Magnetics*, vol. 24, no. 6, pp. 2901–2903, 1988.

[38] L. Zhu, S. Z. Jiang, Z. Q. Zhu, and C. C. Chan, “Analytical methods for minimizing cogging torque in permanent-magnet machines,” *IEEE Transactions on Magnetics*, vol. 45, no. 4, pp. 2023–2031, 2009.

[39] M. S. Islam, S. Mir, and T. Sebastian, “Issues in reducing the cogging torque of mass-produced permanent-magnet brushless DC motor,” *IEEE Transactions on Industry Applications*, vol. 40, no. 3, pp. 813–820, 2004.

[40] W. Q. Chu and Z. Q. Zhu, "Investigation of torque ripples in permanent magnet synchronous machines with skewing," *IEEE Transactions on Magnetics*, vol. 49, no. 3, pp. 1211–1220, 2013.

[41] J. Sopanen, V. Ruuskanen, J. Nerg, and J. Pyrhonen, "Dynamic torque analysis of a wind turbine drive train including a direct-driven permanent-magnet generator," *IEEE Transactions on Industrial Electronics*, vol. 58, no. 9, pp. 3859–3867, 2011.

[42] W. Fei and Z. Q. Zhu, "Comparison of cogging torque reduction in permanent magnet brushless machines by conventional and herringbone skewing techniques," *IEEE Transactions on Energy Conversion*, vol. 28, no. 3, pp. 664–674, 2013.

[43] Y.-s. Xue, L. Han, H. Li, and L.-d. Xie, "Optimal Design and Comparison of Different PM Synchronous Generator Systems for Wind Turbines," *Electrical Machines and Systems*, no. ICEMS 2008, pp. 2448–2453, 2008.

[44] T. Surinkaew and I. Ngamroo, "Coordinated robust control of DFIG wind turbine and pss for stabilization of power oscillations considering system uncertainties," *IEEE Transactions on Sustainable Energy*, vol. 5, no. 3, pp. 823–833, 2014.

[45] J. L. Rodriguez-Amenedo, S. Arnaltes, and J. C. Burgos, "Automatic generation control of a wind farm with variable speed wind turbines," *Transactions on Energy Conversion*, vol. 17, no. 2, pp. 279–284, 2002.

[46] N. Strachan and D. Jovcic, "Offshore wind farm with centralised power conversion and DC interconnection," *IET Generation, Transmission & Distribution*, vol. 3, no. 6, pp. 586–595, 2009.

[47] P. Ngatchou, A. Zarei, and M. El-Sharkawi, "Pareto multi objective optimization," in *Proceedings of the 13th International Conference on, Intelligent Systems Application to Power Systems*, vol. 40, (Arlington, VA, USA), pp. 100–105, IEEE, 2005.

[48] A. E. Fitzgerald, J. Charles Kingsley, and S. D. Umans, *Electric Machinery*, vol. 319. McGraw-Hill,Inc., 6th ed., 2003.

[49] J. N. Stander, G. Venter, and M. J. Kamper, “Review of direct-drive radial flux wind turbine generator mechanical design,” *Wind Energy*, vol. 15, pp. 459–472, 2012.

[50] A. Zavvos, *Structural Optimisation of Permanent Magnet Direct Drive Generators for 5MW Wind Turbines*. PhD thesis, The University of Edinburgh, 2013.

[51] N. Milivojevic, N. Schofield, I. Stamenkovic, and Y. Gurkaynak, “Field Weakening Control of PM Generator Used for Small Wind Turbine Application,” in *IET Conference on Renewable Power Generation (RPG)*, (Edinburgh, UK), IET.